

REPORT DOCUMENTATION PAGE			Form Approved OMB No. 0704-0188	
Public reporting burden for this collection of information is estimated to average 1 hour per response, including the time for reviewing instructions, searching existing data sources, gathering and maintaining the data needed, and completing and reviewing the collection of information. Send comments regarding this burden estimate or any other aspect of this collection of information, including suggestions for reducing this burden, to Washington Headquarters Services, Directorate for Information Operations and Reports, 1215 Jefferson Davis Highway, Suite 1204, Arlington, VA 22202-4302, and to the Office of Management and Budget, Paperwork Reduction Project (0704-0188), Washington, DC 20503.				
1. AGENCY USE ONLY (Leave blank)	2. REPORT DATE 14.Nov.03	3. REPORT TYPE AND DATES COVERED DISSERTATION		
4. TITLE AND SUBTITLE "DETECTION AND DIAGNOSIS OF ORAL NEOPLASIA WITH CONFOCAL MICROSCOPY AND OPTICAL COHERENCE"		5. FUNDING NUMBERS		
6. AUTHOR(S) MAJ CLARK ANNE L				
7. PERFORMING ORGANIZATION NAME(S) AND ADDRESS(ES) UNIVERSITY OF TEXAS AT AUSTIN		8. PERFORMING ORGANIZATION REPORT NUMBER CI02-1303		
9. SPONSORING/MONITORING AGENCY NAME(S) AND ADDRESS(ES) THE DEPARTMENT OF THE AIR FORCE AFIT/CIA, BLDG 125 2950 P STREET WPAFB OH 45433		10. SPONSORING/MONITORING AGENCY REPORT NUMBER		
11. SUPPLEMENTARY NOTES				
12a. DISTRIBUTION AVAILABILITY STATEMENT Unlimited distribution In Accordance With AFI 35-205/AFIT Sup 1			12b. DISTRIBUTION CODE	
13. ABSTRACT (Maximum 200 words)				
20031126 030				
14. SUBJECT TERMS			15. NUMBER OF PAGES 169	
			16. PRICE CODE	
17. SECURITY CLASSIFICATION OF REPORT	18. SECURITY CLASSIFICATION OF THIS PAGE	19. SECURITY CLASSIFICATION OF ABSTRACT	20. LIMITATION OF ABSTRACT	

THE VIEWS EXPRESSED IN THIS ARTICLE ARE THOSE OF
THE AUTHOR AND DO NOT REFLECT THE OFFICIAL
POLICY OR POSITION OF THE UNITED STATES AIR
FORCE, DEPARTMENT OF DEFENSE, OR THE U.S.
GOVERNMENT

© Copyright

by

Anne Lauren Clark

2003

**The Dissertation Committee for Anne Lauren Clark certifies that this is the
approved version of the following dissertation:**

**Detection and Diagnosis of Oral Neoplasia
with
Confocal Microscopy and Optical Coherence Microscopy**

Committee:

Rebecca Richards-Kortum, Supervisor

Ann Gillenwater

Thomas Milner

H. G. Rylander, III

Joseph Izatt

The views expressed in this article are those of the author and do not reflect the official policy or position of the United States Air Force, Department of Defense, or the U.S. Government

Detection and Diagnosis of Oral Neoplasia
with
Confocal Microscopy and Optical Coherence Microscopy

by

Anne Lauren Clark, B. S., M. S.

Dissertation

Presented to the Faculty of the Graduate School of
the University of Texas at Austin
in Partial Fulfillment
of the Requirements
for the Degree of

Doctor of Philosophy

The University of Texas at Austin

August 2003

Dedication

To my parents, for always being there with support and love.

Acknowledgements

I want to thank some of the people who have been so important to my finishing this dissertation. Earning a Ph.D. is never a one person accomplishment and I know that I never would have made it without support from a lot of wonderful people.

The first person that I have to thank is my advisor, Dr. Rebecca Richards-Kortum. Before coming to Texas, I heard some great things about her and they've all been true and more. I always knew that if I reached a standstill in my research that she'd know a way to fix the problem or something else to consider. And even more importantly, I knew that no matter how busy things got, she'd be there, to hold qualifiers three days before the baby was due, to read a draft that just needed a little more time, whatever was needed.

Next, I'd like to thank the members of my committee. I never would have made it through the clinical studies without Dr. Gillenwater. I particularly remember a day when she jumped on a plane with an hour's notice because the engineers needed her in Austin to explain some histology. I'd like to thank Dr. Izatt for introducing me to optical coherence microscopy, Dr. Milner and his lab for answering the OCT neophyte's questions, and Dr. Rylander for his enthusiasm and support.

Last, but not least, I'd like to acknowledge the friends that saw me through. The LaChance clan adopted me into the family and made sure I didn't get too engrossed in my research. Anne Williams was always being ready to pick up the phone and let me vent, no matter how late. Alicia Lacy, Mark Carlson, Betsy Hsu, Nate Kemp, Gracie Vargas, and the rest of the biomedical engineering graduate students never gave up on

me, even when I disappeared for weeks on end to write proposals and dissertations. And of course, I need to thank everyone in the Optical Spectroscopy and Imaging Lab for the advice, help, support, patience, and whatever else was needed to get this done. I really couldn't have done it without your help!

Detection and Diagnosis of Oral Neoplasia
with Confocal Microscopy and Optical Coherence Microscopy

Publication No. _____

Anne Lauren Clark, Ph.D.

The University of Texas at Austin, 2003

Supervisor: Rebecca Richards-Kortum

Oral cancer remains an important health issue in the world. In the United States, over 27,000 new cases and approximately 7,000 deaths attributable to oral cancer are expected in 2003. In some areas of the world, this malignancy is much more common; oral cancer is the most common cancer among men and the third most common cancer in women, in India [1]. Prognosis for patients with oral cancer remains low with five-year survival rates hovering in the fiftieth percentile [2]. High resolution, *in vivo* optical imaging may offer a clinically useful adjunct to standard histopathologic techniques.

The work in this dissertation centered on optical imaging in the oral cavity to determine whether confocal microscopy and optical coherence microscopy could detect

and diagnose oral neoplasia. A survey of features of normal epithelium and SCCs using a reflectance confocal microscope resolved nuclear density and morphology differences between neoplastic and non-neoplastic oral cavity specimens and features of non-cancerous and cancerous oral tissue such as inflammation, fibrosis, muscle fibers and salivary glands. A detailed study of the differences between normal, preneoplastic, and neoplastic oral cavity tissue using images from a reflectance confocal microscope found that descriptive statistics characterizing nuclear morphology allowed slight differentiation between normal and dysplastic epithelium. Reviews of confocal images by trained pathologists and untrained engineers emphasized the need for situational awareness of the region of the epithelium occupied by the image plane. An optical coherence microscope with subcellular resolution and an estimated penetration depth (based on SNR) of 690 – 1,227 microns was built to support imaging deeply within oral mucosa. This increased penetration depth supported a study of epithelial scattering coefficients from reflected nuclear intensities which was successful in non-hyperkeratotic layers and showed differentiation between scattering properties of normal and dysplastic epithelium and SCCs.

Overall, the research in this dissertation gives a thorough basis for optical imaging in the oral cavity. Images were acquired from five sites in the oral cavity and represented a wide variety of pathological conditions. Two approaches, morphologic statistical analysis and calculation of scattering coefficients, showed diagnostic contrast with the differentiation from the scattering coefficients being superior.

Table of Contents

List of Tables	xiv
List of Figures.....	xv
Chapter 1 Introduction.....	1
1.1 Introduction.....	1
1.2 Specific Aims.....	1
1.3 Dissertation Overview	2
Chapter 2 Background	4
2.1 Introduction.....	4
2.2 Motivation.....	4
2.3 Anatomy of the Oral Cavity.....	6
2.4 Pathology of the Oral Cavity	8
2.5 Literature Review.....	10
2.5.1 <i>Confocal microscopy</i>	12
2.5.2 <i>Optical coherence tomography</i>	18
2.5.3 <i>Optical coherence microscopy</i>	22

Chapter 3 Confocal Microscopy for Real Time Detection of Oral Cavity

Neoplasia24

3.1 Introduction.....24

3.2 Methods and Materials.....26

3.2.1 Specimens.....26

3.2.2 Confocal System.....27

3.2.3 Imaging and Image Processing28

3.3 Results.....30

3.4 Discussion.....43

3.5 Conclusion46

Chapter 4 Confocal Microscopy for Diagnosis of Oral Cavity Preneoplasia and

Neoplasia47

4.1 Introduction.....47

4.2 Methods and Materials.....49

4.2.1 Specimens.....49

4.2.2 Confocal System.....50

4.2.3 Images and Image Processing51

4.2.4 Pathologic Review of Confocal Images52

4.3	Results.....	54
4.3.1	<i>Imaging Results</i>	54
4.3.2	<i>Nuclear Morphologic Analysis</i>	61
4.3.3	<i>Image Review</i>	65
4.4	Discussion.....	71
4.5	Conclusion	73

Chapter 5 Design, Construction, and Characterization of an Optical Coherence Microscope.....75

5.1	Introduction.....	75
5.2	System Design Requirements	76
5.3	System Design and Final Configuration.....	78
5.3.1	<i>Choosing a source and objective</i>	79
5.3.2	<i>Reference arm design</i>	81
5.3.3	<i>Sample arm design</i>	84
5.3.4	<i>Computer and electrical design</i>	88
5.4	OCM Characterization	90
5.4.1	<i>Resolution</i>	90
5.4.2	<i>Penetration Depth Estimate</i>	92

Chapter 6 Detection and Diagnosis of Oral Neoplasia with an Optical Coherence

Microscope.....94

6.1 Introduction.....94

6.2 Methods and Materials.....97

6.2.1 Specimens.....97

6.2.2 Optical Coherence System98

6.2.3 Imaging and Image Processing100

6.2.4 Scattering Coefficient Analysis101

6.3 Results.....102

6.3.1 Imaging Results.....102

6.3.2 Penetration Depth and Scattering Coefficient Analysis109

6.4 Discussion.....115

6.5 Conclusion117

Chapter 7 Summary and Conclusions.....119

7.1 Summary of Results.....119

7.2 Future Directions121

References.....	123
------------------------	------------

Vita	146
-------------------	------------

List of Tables

Table 2.1. Five-year relative survival rates by stage at diagnosis, 1989-1996 [3].	5
Table 3.1. Number of clinically normal and abnormal biopsies from each site.	30
Table 3.2. Histopathologic diagnosis by patient.....	31
Table 4.1. Number of clinically normal and abnormal biopsies from each site.	55
Table 4.2. Histopathologic diagnosis by patient.....	56
Table 5.1. Top-level system requirements.....	77
Table 6.1. Number of clinically normal and abnormal biopsies from each site.	103
Table 6.2. Histopathologic diagnosis by patient.....	104

List of Figures

Figure 2.1. Masticatory and lining mucosa. (A) Masticatory mucosa; (i) basal layer; (ii) spinous layer; (iii) granular layer (arrows); (iv) keratinized layer. (B) Lining mucosa; (i) basal layer; (ii) spinous layer; (iii) intermediate layer; (iv) superficial layer [8].....	8
Figure 2.2. Oral cancer features. (A) Nuclear size differences, cell shape changes and tissue disruption. (B) Invasion of epithelium and connective tissue [12].....	9
Figure 2.3. Optical sectioning in a confocal microscope [64].	14
Figure 2.4. Schematic of an OCT System [48].....	19
Figure 2.5. Plots of confocal and OCM response [59].	23
Figure 3.1. Block diagram of the near real-time reflectance confocal microscope used to image oral cavity specimens.	28
Figure 3.2. Comparison of confocal images to histologic sections. The histology section (A) and mosaic of confocal images (B) from a 200 micron thick transverse organ culture of a normal gingiva biopsy show epithelium and stroma; the basal epithelial nuclei are readily apparent at the epithelial stromal junction (double arrows). Epithelial cell nuclei and fibroblast nuclei (single arrow) are resolved. The histology section (C) and transverse confocal image (D) of a hyperkeratotic tongue biopsy show epithelial cell nuclei from superficial epithelium on the right (double arrows) to the basal layer (single arrow) on the left. Scale bars = 50 microns.	33

Figure 3.3. Transverse histologic image (A) and en face confocal images (B-D) obtained at different depths beneath the epithelial surface from hyperkeratotic tissue from the ventral tongue surface. Nuclear density, cell size, and cytoplasmic scattering change as the depth of the focal plane increases from (B) 20 microns to (C) 50 microns to (D) 150 microns beneath the epithelial surface. Scale bars = 50 microns..... 34

Figure 3.4. Histologic and confocal images of a moderately differentiated SCC from the lateral surface of the tongue. (A) Low magnification image of a keratin antibody (MMAC) stained section showing tumor cells interspersed with stroma containing inflammation (2.5X objective). (B) High magnification image of tumor cells (single arrows) containing pleomorphic nuclei and stroma with inflammation (double arrows). (C) Confocal image taken 100 microns below the epithelial surface illustrating pleomorphic nuclei (single arrows) and dark areas corresponding to stroma containing inflammation (double arrows). Scale bars = 50 microns. 36

Figure 3.5. Confocal and histologic mages of invasive SCC of the soft palate. (A) Low magnification image of a keratin antibody (MMAC) stained section showing extensive tumor cells surrounding areas of stroma with inflammation (2.5X objective). (B) High magnification image of keratinized, tightly packed tumor cells (single arrow) with stroma containing inflammation (double arrows) (20X objective). (C) Confocal image taken 100 microns below the surface of tightly packed, highly scattering tumor cells (single arrow) with dark areas of stroma with inflammation (double arrows). (D) High magnification histologic image of less keratinized, larger tumor cells (single arrow) with stroma containing inflammation

(double arrows) (20X objective). (E) Confocal image taken 100 microns below the surface with larger cells (single arrow) and less background scattering combined with dark areas of stroma with inflammation (double arrows). Scale bars = 50 microns..... 37

Figure 3.6. Images of a moderately differentiated SCC from the buccal mucosa. (A) Low magnification image of a keratin antibody (MMAC) stained section showing keratin pearls, highly keratinized tumor cells, and stroma with inflammation (2.5X objective). (B) High magnification histologic image of tumor cells (single arrow) and stroma containing inflammation (double arrows) (20X objective). (C) Confocal image taken 200 microns below the epithelial surface showing dark regions of stroma with inflammation (double arrows) alternating with tightly packed tumor cells (single arrow) containing irregular nuclei. (D) High magnification histologic image of a keratin pearl (single arrow) (20X objective). (E) Confocal image of a keratin pearl (single arrow) taken 50 microns below the surface showing the highly reflective, speckled appearance characteristic of keratin. Scale bars = 50 microns. 39

Figure 3.7. Images of a well differentiated SCC from the gingiva. (A) Low magnification image of a keratin antibody (MMAC) stained section showing tumor cells and keratin pearls interspersed with stroma containing inflammation (2.5X objective). (B) High magnification histologic image of a keratin pearl (double arrows) (20X objective). (C) Confocal image taken 50 microns below the surface containing highly reflective keratin (double arrows). (D) High magnification histologic image of keratin pearls with highly keratinized tumor cells (single arrow)

(20X objective). (E) Confocal image taken 50 microns below the surface containing areas of highly reflective keratin with nuclei (single arrow). Scale bars = 50 microns.

..... 40

Figure 3.8. Images of a muscle and fibrosis from a moderately differentiated SCC from the lateral surface of the tongue. (A) Low magnification image of an H&E section shows skeletal muscle and extensive fibrosis (2.5X objective). (B) High magnification histologic image of muscle (single arrow) (20X objective). (C) Confocal image of muscle (single arrow) taken 100 microns below the surface. (D) High magnification histologic image of fibrosis (double arrows) with elongated fibroblast nuclei (single arrow) (20X objective). (E) Confocal image of fibrosis (double arrows) taken 50 microns below the surface illustrating reflectance from structural protein fibers and containing elongated fibroblast nuclei (single arrow). Scale bars = 50 microns. 41

Figure 3.9. Images of salivary glands from the floor of the mouth. (A) Low magnification image of a keratin antibody (MMAC) stained section showing extensive salivary glands (2.5X objective). (B) High magnification histologic image of salivary glands (single arrow) (20X objective). (C) Confocal image of salivary glands (single arrow) taken 50 microns below the surface. Scale bars = 50 microns.

..... 42

Figure 4.1. Diagram of the OCM system containing the confocal arm used to image oral cavity specimens with its reference arm blocked. 51

Figure 4.2. Transverse histologic section (A) with en face confocal images (B – F) obtained at different depths below the epithelial surface of a hyperkeratotic and hyperplastic biopsy from the ventral surface of the tongue. Nuclear density, cell size, and cytoplasmic scattering change as the depth of the focal plane increases from (B) 40 microns to (C) 80 microns beneath the epithelial surface, moving from the superficial layer to the intermediate. At 120 microns below the tissue surface, brightly returning basal cells appear in one portion of the image (arrow) and at (E) 160 microns, the image plane has reached the top of a rete process surrounded by these basal cells. At (F) 200 microns, another rete process appears in the bottom center of the image while a dark region of stroma occupies most of the top of the image (double arrows). Scale bars = 20 microns..... 58

Figure 4.3. Clinical example with a macroscopic digital image of a patient's soft palate and corresponding histologic and confocal images from biopsies acquired from this patient. (A) Digital image identifying the region of the soft palate from which the abnormal (B) and normal (E) biopsies were acquired. (B) Low magnification image of an H&E section from an invasive, well differentiated SCC with tumor cells and stroma with inflammation (4X objective). (C) High magnification image of an H&E section from an invasive, well differentiated SCC with tumor cells (arrow) and stroma with inflammation (double arrows) (20X objective). (D) Confocal image taken 40 microns below the surface of an invasive, well differentiated SCC showing tightly packed tumor cells with irregular nuclei (arrow) and a dark region of stroma with inflammation (double arrows). (E) Low magnification image of an H&E

section from a hyperkeratotic and hyperplastic biopsy with regularly shaped nuclei and a much lower nuclear-cytoplasmic ratio than in (B) (10X objective). (E) Low magnification image of an H&E section from a hyperkeratotic and hyperplastic biopsy with regularly shaped nuclei (arrow) and a much lower nuclear-cytoplasmic ratio than in (C) (20X objective). (F) Confocal image taken 100 microns below the surface with regularly shaped nuclei (arrow) and a much lower nuclear-cytoplasmic ratio than in (D). Scale bars = 20 microns. 60

Figure 4.4. Scatter plot of nuclear to cytoplasmic ratio versus average nuclear area for images at 50 microns below the tissue surface. Images are classified as normal, dysplastic, or from SCCs based on histology. 62

Figure 4.5. Scatter plot of nuclear to cytoplasmic ratio versus average nuclear area for images that are likely from the basal layer (at the maximum depth below the tissue surface at which nuclei are clearly and fully resolvable for a particular depth of focus stack). Images are classified as normal, dysplastic, or from SCCs. At these depths, a slight differentiation between normal and dysplastic images as a function of both nuclear to cytoplasmic ration and average nuclear area can be seen. 63

Figure 4.6. Scatter plot of nuclear to cytoplasmic ratio versus average nuclear area for images from the tongue that are likely from the basal layer (at the maximum depth below the tissue surface at which nuclei are clearly and fully resolvable for a particular depth of focus stack). Images are classified as normal, dysplastic, or from SCCs (with no samples in this set). The differentiation between normal and

dysplastic samples is still very limited when morphologic variations due to site are removed..... 64

Figure 4.7. (A) Scatter plot of the sensitivity and specificity of the diagnoses made by the trained reviewers. (B) Mean sensitivity and specificity of trained reviewers was $73\% \pm 11\%$ and $36\% \pm 15\%$, respectively..... 66

Figure 4.8. (A) A breakdown of the percentage of trained reviewers making the correct diagnosis for abnormal samples identifies that the trained reviewers had difficulty diagnosing moderate dysplasia, but were much better at diagnosing mild dysplasia and SCC. (B) A breakdown of the percentage of trained reviewers making the correct diagnosis for normal samples shows that the trained reviewers made incorrect diagnoses more than 50% of the time but does identify that 1) the trained reviewers had extra difficulty diagnosing severe hyperkeratotic cases and one biopsy with a striated tissue architecture and 2) three histopathologic diagnoses for tangentially cut biopsies may be incorrect..... 67

Figure 4.9. Examples of confocal images from diagnostically normal biopsies that trained reviewers consistently classified as abnormal. (A) Confocal image from 90 microns below the surface of a severely hyperkeratotic biopsy from the lateral surface of a tongue with pleomorphic nuclei (arrow). (B) Confocal image from 100 microns below the surface of a tangentially cut buccal mucosa biopsy with pleomorphic nuclei (arrow). (C) Confocal image from 25 microns below the surface of a hyperkeratotic and hyperplastic biopsy from the lateral surface of a tongue with a striated tissue architecture that was repeated at multiple depths..... 68

Figure 4.10. (A) Scatter plot of the sensitivity and specificity of the diagnoses made by the untrained reviewers. (B) Mean sensitivity and specificity of untrained reviewers was $63\% \pm 18\%$ and $61\% \pm 15\%$, respectively.	70
Figure 4.11. (A) A breakdown of the percentage of untrained reviewers making the correct diagnosis for abnormal samples identifies that the untrained reviewers also had difficulty diagnosing moderate dysplasia and that they did not do as well as the trained reviewers in identifying mild dysplasia and SCC. (B) A breakdown of the percentage of untrained reviewers making the correct diagnosis for normal samples shows that they diagnosed severe hyperkeratosis correctly as often as mild to moderate hyperkeratosis, but did misdiagnose the biopsy with striated tissue architecture. More of the diagnoses from the untrained reviewers for the three tangentially cut biopsies matched the histopathologic diagnosis.	71
Figure 5.1. OCM block diagram.	78
Figure 5.2. Sample arm optics.	87
Figure 5.3. Electrical interfacing requirements.....	89
Figure 5.4. Intensity as a function of u and a normalized parameter, $A = 2.81$	91
Figure 5.5. Measured resolution for the OCM. (A) A line profile from an image of a Ronchi grating showing the system's edge response. A lateral resolution of 2.3 microns was determined by measuring the distance between the 10% and 90% intensity lines. (B) Normalized intensity response to moving a mirror through the focus while keeping the reference arm's pathlength matched with the top of the mirror. Axial resolutions of 5.4 microns and 7.8 microns for the confocal mode and	

the OCM, respectively, were measured through the full-width half-maximum of the average intensity. The slight widening of axial resolution for the OCM system is attributed to dispersion effects. 92

Figure 6.1. Diagram of the OCM system used to image oral cavity specimens..... 99

Figure 6.2. Transverse histologic image (F) with en face confocal (A – E) and OCM (G – K) images obtained at different depths beneath the epithelial surface of a hyperkeratotic and hyperplastic floor of the mouth biopsy. Both imaging modalities captured an increase in nuclear density as the depth of the focal plane increased from (A, G) 50 microns to (B, H) 150 microns to (C, I) 250 microns below the tissue surface. At (D) 300 microns below the tissue surface, confocal image quality started to degrade and by (E) 350 microns below the tissue surface, features were barely resolvable. In the corresponding OCM images, cell membranes (arrow) are still resolvable at (J) 300 microns below the tissue surface. At (K) 350 microns below the tissue surface, cells are captured (arrow) and part of the focal plane has traversed through the basement membrane into stroma (double arrows). Scale bars = 20 microns..... 106

Figure 6.3. Histologic and en face OCM images of normal and cancerous tissue. The consistent nuclear area and spacing in images from a hyperplastic and hyperkeratotic biopsy from gingiva (A, C) contrast sharply with the tightly packed tumor cells (arrow) containing irregular nuclei visualized in a well differentiated SCC from the soft palate (B, D). A portion of stroma with inflammation (double arrows) is also captured in both images of the SCC (B, D). Scale bars = 20 microns..... 108

Figure 6.4. Penetration depth of confocal microscope versus OCM system. 110

Figure 6.5. Comparison of histology to normalized reflected nuclear intensity as a function of depth. (A) Histologic image from a keratin antibody (MMAC) stained section from a hyperkeratotic and hyperplastic gingiva biopsy. (B) Plot of normalized reflected nuclear intensity taken from the same biopsy in (A) showing characteristic decay within the hyperkeratotic region and exponential attenuation starting at 70 microns with a fit constant of 54 (with a mean correlation coefficient of 0.91), implying a scattering coefficient of 27 cm^{-1} . (C) Histologic image from a keratin antibody (MMAC) stained section from a hyperkeratotic gingiva biopsy with mild dysplasia and focal moderate to severe dysplasia. (D) Plot of normalized reflected nuclear intensity taken from the same biopsy in (C) showing characteristic decay of the hyperkeratotic region and exponential attenuation starting at 120 microns with a fit constant of 69 (with a mean correlation coefficient of 0.88), implying a scattering coefficient of 34 cm^{-1} 112

Figure 6.6. Examples of normalized nuclear intensity plots from different sites and pathologic states. (A) Plot from a hyperkeratotic and hyperplastic biopsy from the floor of the mouth with an estimated scattering coefficient of 16 cm^{-1} (mean correlation coefficient of 0.92). (B) Plot from a hyperkeratotic, mildly dysplastic biopsy from the lateral surface of a tongue with an estimated scattering coefficient of 34 cm^{-1} (mean correlation coefficient of 0.96). (C) Plot from a severely hyperkeratotic, moderately dysplastic biopsy from the floor of the mouth with an estimated scattering coefficient of 48 cm^{-1} (mean correlation coefficient of 0.96).

(D) Plot from an invasive, well differentiated SCC from the soft palate with an estimated scattering coefficient of 70 cm^{-1} (mean correlation coefficient of 0.98). 114

Figure 6.7. (a) Scatter plot of scattering coefficients for non-hyperkeratotic tissue. (b) Bar chart comparing mean scattering coefficients for non-hyperkeratotic tissue by pathologic diagnosis..... 115

CHAPTER 1

Introduction

1.1 INTRODUCTION

This dissertation describes an exploration of optical imaging in the oral cavity to investigate the feasibility of using confocal microscopy and optical coherence microscopy for detection and diagnosis of oral neoplasia. Both of these imaging systems were able visualize, at the subcellular level, features of both normal and neoplastic oral mucosa throughout the oral cavity. This capability enables non-invasive evaluation of oral lesions with 3D sub-cellular resolution making the imaging modalities strong candidates for use in a clinical setting.

1.2 SPECIFIC AIMS

The primary objective of my research was to assess the feasibility of using optical imaging modalities such as confocal microscopy and optical coherence microscopy for detection of oral neoplasias for the purpose of improving early detection rates of oral dysplasia.

My specific goals were:

1. Explore visualization by optical imaging of features of normal epithelium, dysplasia, and squamous cell carcinoma to support further research into methods of differentiating these pathologic states.
2. Investigate the ability of optical imaging modalities to capture morphologic variations in oral epithelium associated with dysplastic changes and present this information in a format allowing accurate diagnosis of the pathologic state of the sample.
3. Use the extended penetration depth of optical coherence microscopy to study the scattering properties of normal and neoplastic oral mucosa to determine if diagnostic contrast is available to support differentiation between normal and dysplastic tissue.

1.3 DISSERTATION OVERVIEW

After this chapter's overview of research objectives, the second chapter provides motivation and background for this dissertation, including a description of the target tissue's anatomy and pathology, a literature survey, and an overview of the imaging modalities used in our investigation. The third chapter includes a paper accepted for publication by Clinical Cancer Research reporting results from a clinical study of 17 patients that used a near real-time, epi-illumination, reflectance confocal microscope to characterize features of normal and neoplastic oral mucosa in multiple sites of the oral cavity. The fourth chapter includes a paper that we plan to submit to Head and Neck

detailing a study of an additional 22 patients with an epi-illumination, reflectance confocal microscope. This paper explores the diagnostic information contained in confocal images of cell morphology and tissue architecture details by extracting morphological statistics such as nuclear to cytoplasmic ratio and average nuclear area from the images to determine if they provide diagnostic contrast and performing both trained and untrained image reviews to assess the ability of reviewers to diagnose from confocal images. The fifth chapter describes the design and construction of an optical coherence microscope (OCM) that incorporates interferometric techniques from optical coherence tomography with high numerical confocal microscopy to extend penetration depth into oral mucosa. The sixth chapter includes a paper that we plan to submit to the Journal of Biomedical Optics covering a 12 patient clinical study using the OCM to investigate optical imaging's ability to image deeply in oral mucosa and to calculate average reflected nuclear intensity from the intermediate and basal layers of oral mucosa to extract scattering coefficients for a range of sites and pathologic states.

CHAPTER 2

Background

2.1 INTRODUCTION

This chapter contains the background needed to understand this dissertation. The first section contains the motivation for detecting premalignant lesions in the oral cavity. The next two sections detail the anatomy and pathology of the oral cavity with emphasis on the changes that occur during dysplastic progression and are present in squamous cell carcinoma. The chapter then finishes with a literature survey of the imaging modalities currently used to detect oral cancer before giving details on the three subcellular techniques that provide the foundation for this work.

2.2 MOTIVATION

Cancer is the second leading cause of death in the U. S. (exceeded only by heart disease) with approximately 1,334,100 new cases expected in 2003 [2], with approximately 85% of these cancers originating in an epithelial layer. Five-year survival rates for these organ sites are significantly higher when the cancer is diagnosed while still classified as local, or confined to the original organ site, as shown in Table 2.1. For example, in the oral cavity, the 5-year survival rate drops from 81% when diagnosed early to 21% if the cancer has spread to parts of the body at a distance from the primary tumor. These statistics combined with the ease of accessing epithelial-lined cavities has

engendered strong interest in developing screening techniques for health professionals to detect precancerous lesions before they progress.

Table 2.1. Five-year relative survival rates by stage at diagnosis, 1989-1996 [3].

Site	All Stages %	Local %	Regional %	Distant %
Oral	54	81	44	21
Colon & Rectum	61	90	65	8
Melanoma (Skin)	88	96	59	13
Urinary Bladder	81	93	49	6
Uterine Corpus	84	96	64	26

Despite the presence of these premalignant lesions, screening and detection programs in sites other than the cervix have not been successful. Screening in the mouth is especially difficult due to the many types of benign lesions. In [4], Scully lists 32 lesions other than neoplasms that present as lumps or swellings in the mouth. Current guidance is to perform a biopsy (either incisional or with an oral brush) when a lesion has been present for over three weeks or if the patient is in a high-risk group [5]. Another factor that makes early diagnosis difficult is the extensive nature of many mouth lesions, complicating the choice of biopsy site [6]. As a result, from 1989 – 1996, only 36% of oral cancer was detected while in the localized stage versus 53% of cervical cancer [3].

This dissertation describes optical imaging of epithelial tissue in the oral cavity using both confocal microscopes and an optical coherence microscope (OCM). Both of these instruments have the ability to optically section tissue, non-invasively providing 3D

sub-cellular resolution images without the need for histologic processing. If successful, optical imaging could reduce the number of unnecessary biopsies with their associated pathology requirements while increasing the accuracy of diagnoses by allowing the clinician to quickly image the entire lesion instead of just a small sample.

2.3 ANATOMY OF THE ORAL CAVITY

The ability to detect dysplastic changes requires a sound knowledge of the tissue, both normal and abnormal, to be examined. The most common malignant lesions of the oral cavity are squamous carcinomas that primarily affect the stratified squamous epithelium in the mouth [6]. Before examining the neoplasms that lead to squamous cell carcinoma, it is therefore important to understand the different types of oral epithelia and their structure.

The oral cavity is lined by oral mucosa consisting of stratified squamous epithelium responsible for protecting the mouth from abrasion during eating [7]. A complicating factor in oral cancer screening and diagnosis is that there are three distinct type of oral mucosa: masticatory, or tough, mucosa found on the gums and the hard palate on the roof of the mouth; lining, or flexible, mucosa found on the lips, cheeks, floor of the mouth, inferior surface of the tongue, and the soft palate; and specialized mucosa (a mix of masticatory and lining) on the dorsal surface of the tongue [8]. Each mucosa type has layers of tightly packed epithelial cells whose differentiation varies depending on function.

The masticatory mucosa shown in Figure 2.1A includes four distinct layers. The stratum basale, or basal layer, is closest to the basement membrane, contains the least-differentiated cells arranged in two or three layers, and is responsible for cell division and production. These cells are the smallest, being cuboidal or columnar in shape [8]. Cells in this layer are pushed up into the stratum spinosum, or spinous layer, as the cells continue to divide. While in the spinous layer, the cells become larger and their shape becomes polyhedral with numerous cytoplasmic processes, or spines, attached by desmosomes to adjacent cells [9]. The next layer, the stratum granulosum, or granular layer, is specific to the masticatory mucosa in the mouth. This layer contains flattened cells with decreased nuclear size and densely packed keratin [8]. These cells combined with thickening of the cell membrane and a large number of keratin filaments result in a final layer of densely packed keratinized cells responsible for reducing the permeability of masticatory mucosa.

The lining mucosa, shown in Figure 2.1B, is also known as nonkeratinized epithelium, making it less resistant to injury, but much more flexible than the masticatory mucosa. It includes similar bottom basal and spinous layers, but instead of a granular layer, there is an intermediate layer in which the cells become flattened as they move into the final superficial layer [8]. The top two layers show a gradual decrease in the volume of organelles and decreased desmosomes between the cells, resulting in a much more permeable tissue than the masticatory mucosa [8].

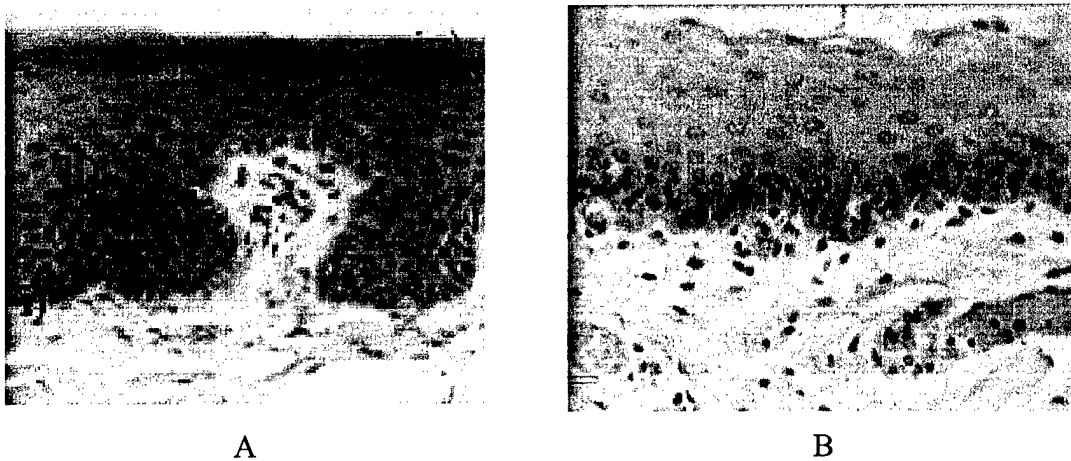


Figure 2.1. Masticatory and lining mucosa. (A) Masticatory mucosa; (i) basal layer; (ii) spinous layer; (iii) granular layer (arrows); (iv) keratinized layer. (B) Lining mucosa; (i) basal layer; (ii) spinous layer; (iii) intermediate layer; (iv) superficial layer [8].

2.4 PATHOLOGY OF THE ORAL CAVITY

Optical imaging must also be able to detect features used to determine whether a lesion is premalignant or benign throughout the epithelial layer. This section will first define the terms commonly used to describe oral cancer and the morphologic changes associated with dysplasia before describing common premalignant and malignant tumors in the oral cavity. The mouth is prone to many conditions other than cancer that can cause a tumor, or a swelling of the tissue [10]. Only those tumors that demonstrate an independent, uncoordinated new growth of tissue potentially capable of unlimited proliferation and do not regress after removal of the stimulus responsible for the lesion are labeled as premalignant or neoplasms [10]. Changes in the normal shape, size, and organization of the tissue and its cells associated with this uncontrollable growth are called dysplasia [7]. When the neoplasm breaks through the basement membrane below

the epithelium and starts to spread into surrounding and distant tissues, or metastasize, the growth is called a cancer, a malignancy, or a carcinoma (cancers of the epithelia) [7].

Current detection practice for oral neoplasia involves tissue biopsy and examination by a trained pathologist. The pathologist looks for dysplasia indicating the presence of abnormal tissue. Common indicators of premalignant or malignant lesions are morphological changes in cells and their nuclei and inconsistent tissue structure. Unlike normal cells that tend to have the same shape and size (due to their shared role), cancer cells have varied shapes and sizes, as well as distorted shapes [11]. Since the primary indicator of malignancy is uncontrolled growth, the nuclei in abnormal cells are typically larger with variable shapes. In addition, they appear darker after being stained by certain dyes due to an increased amount of DNA [11]. Finally, neoplasms compromise the overall consistency of the tissue and are capable of invading other tissues. All of these changes are visible in the histology images in Figure 2.2.

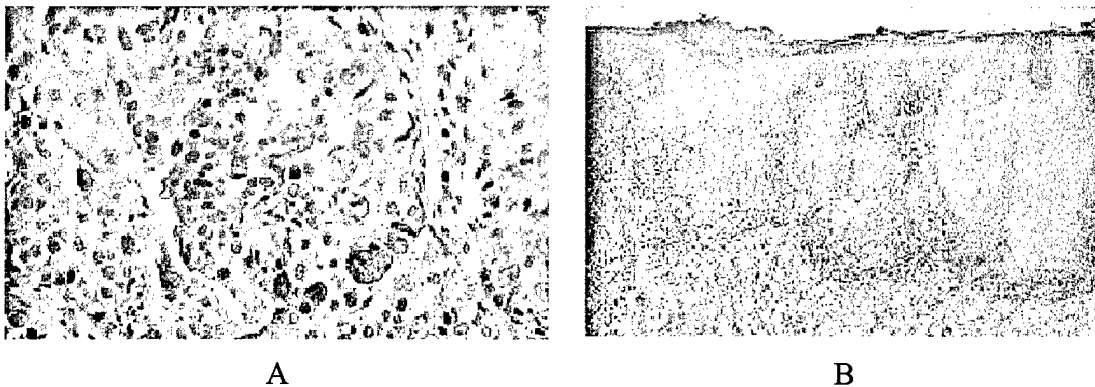


Figure 2.2. Oral cancer features. (A) Nuclear size differences, cell shape changes and tissue disruption. (B) Invasion of epithelium and connective tissue [12].

While there are many different kinds of mouth lesions, two are definitely linked with oral cancer: leukoplakia and erythroplakia. Leukoplakia is a general term applied to white patches on oral mucosa membranes that cannot be rubbed off or removed by scraping and cannot be classified clinically or microscopically as another disease entity [12]. This definition is purely clinical because there are many benign reasons for leukoplakia, including cheek biting, friction, or tobacco use [4]. In fact, only 6 – 17.5% of cases actually transform into malignant tumors [12]. Patches of leukoplakia vary from nonpalpable, faintly translucent white areas to thick, fissured, indurated lesions and often have finely wrinkled or shriveled surfaces [10]. Since these lesions represent nearly 85% of all oral premalignancies [12], biopsies looking for dysplasia are recommended in all long-term cases to decide whether they are benign or malignant.

Erythroplakia is a less common lesion of the oral cavity and appears as an isolated, red, velvety lesion affecting patients mainly in their sixties and seventies [4]. They also appear in concert with leukoplakia. These lesions tend to appear on the floor of the mouth, soft palate, and masticatory mucosa [12] and are more worrisome than leukoplakia because 75 – 90% of lesions develop into carcinoma and are severely dysplastic [4]. Due to this increased malignancy rate, immediate excision and histology of these lesions is recommended.

2.5 LITERATURE REVIEW

A literature survey of detection and screening methods for oral cancer was performed. These techniques can be split into four categories: biopsy or cytology

specimen evaluation, spectroscopy, macroscopic imaging, and microscopic imaging. The technique most often used today to diagnose premalignant lesions in the oral cavity is to perform an incisional biopsy to remove a small part of the tumor, stain and process the biopsy, and then have a trained pathologist examine it for dysplasia [11]. A problem with this technique is that oral lesions such as leukoplakia can be large and the biopsy may not be taken in the correct place, resulting in false negatives. Even when successful, the process is painful due to the removal of tissue. It is also lengthy, requiring patients to wait for results. A similar technique uses an oral brush to gently scrape cells from the lesion [13-16] for cytologic review. While effective in non-keratinized lesions such as erythroplakias, exfoliative cytology has limited usefulness in diagnosing malignant transformation of leukoplakias which have a significant keratinized superficial layer preventing deeper dysplastic cells from being sampled [17]. In one study, false negative diagnoses were given for 62% of hyperkeratotic lesions [18].

Another technique proposed for screening oral cancers is optical spectroscopy, which quantitatively measures light tissue interaction to detect abnormal tissue [19-24]. This technique evaluates tissue properties by illuminating the tissue with light, oftentimes using a specific wavelength laser source, and analyzing the intensity and character of light emitted in the form of fluorescence. Studies testing the technique's potential have shown very encouraging results with one study [23] achieving 100% sensitivity (probability that a test is positive, given the patient has the disease) and 98% specificity (probability that a test is negative, given that the person does not have the disease) after using a control population to find optimal excitation wavelengths for normal versus

abnormal samples. Also, the ability to record data and analyze it using a computer reduces the need for clinical expertise and therefore can potentially lower treatment costs. A significant disadvantage of optical spectroscopy is that it is an integrative technique, taking information from all of the tissue. This means that if the neoplasm is not readily visible, the clinician must use a different technique to determine its precise location and extent for treatment.

A variety of macroscopic techniques are available for isolating the location and extent of neoplasms [25-36]. Currently, the most popular are computed tomography (CT) scans and magnetic resonance imaging (MRI) with MRI becoming the dominant technique [29]. MRI's primary advantages over other imaging modalities are the lack of ionizing radiation found in X-ray examinations, high sensitivity to fluid flow, the ability to control the scanning plane, and high contrast resolution in soft tissue [29]. While useful in determining where to perform a biopsy or the full extent of a tumor, MRIs do not have the resolution to characterize tissue [34]. This severely limits the technique's ability to diagnose whether a tumor is benign or premalignant.

There are currently three techniques proposed for imaging at the cellular level: confocal imaging [37-44], OCT [45-51], and OCM [52-61]. The abilities and limitations of these techniques are covered in the next three sections.

2.5.1 Confocal microscopy

Marvin Minsky first conceived the confocal microscope in 1957 [62]. The technique did not become viable though until almost 30 years later, when the laser provided a virtually unlimited power source and the computer allowed fast processing of

the large amount of data needed for images [63]. Since then, the confocal microscope's popularity has grown with many different modes such as reflectance, phase, differential interference contrast (DIC), polarization, and fluorescence becoming readily available. This popularity is primarily due to the instrument's increased resolution over standard light microscopes and its optical sectioning capability. In this dissertation, we only used the reflectance configuration of confocal microscopy.

Optical sectioning is the confocal microscope's ability to image very thin sections of a thick sample by rejecting light from out of focus planes. This ability comes from the use of pinholes in both the illumination and detection paths, providing a point source and a finite detector. Figure 2.3 illustrates this concept, using a simple epi-configuration (or reflection mode) confocal microscope. Light from the point source is focused onto a very small point in the sample. Light returning from this focus spot (shown by the solid line) is refocused onto the detector. More importantly, light reflected from outside the focal plane (shown by the dashed line) is filtered by the pinhole so only a small amount actually reaches the detector. With the addition of a scanning mechanism to record multiple points in the focal plan, optical sectioning allows confocal microscopes to build ultra-thin, *en-face* images through thick samples and, with a little processing, to form three-dimensional pictures.

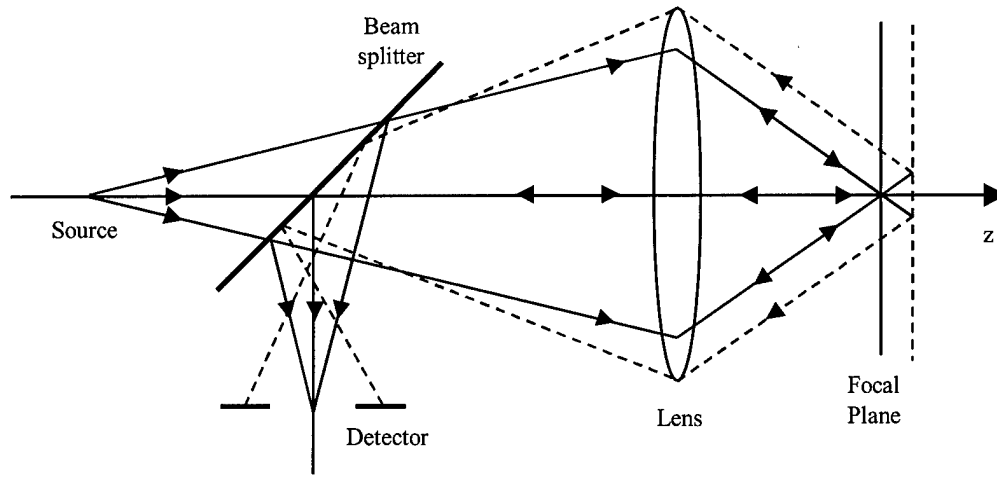


Figure 2.3. Optical sectioning in a confocal microscope [64].

Another advantage of confocal microscopes is their increased resolution over standard light microscopes. A common way to measure resolution in microscopy is to use the full width at half maximum (FWHM) value of the point-spread function (PSF), or intensity pattern illuminated or observed by a lens at its focal plane [65]. Wilson derived a solution for both lateral and axial PSFs in [64] by assuming an infinitely small detector, coherent light at the detector, and making the following normalized optical coordinate transformations:

$$v = \frac{2\pi}{\lambda} r n \sin \alpha \quad (2.1)$$

$$u = \frac{8\pi}{\lambda} z \left\{ n \sin \left(\frac{\alpha}{2} \right) \right\}^2 \quad (2.2)$$

where λ is the wavelength and $n \sin \alpha$ is the numerical aperture (NA) of the lens. In this idealized case, the PSFs are:

$$I(v) = \left(\frac{2J_1(v)}{v} \right)^4 \quad (2.3)$$

$$I(u) = \left(\frac{\sin(u/4)}{u/4} \right)^4 \quad (2.4)$$

where $J_1(v)$ is a first order Bessel function. Solving for the FWHM points of these functions and then substituting them for u and v in (2.1) and (2.2) gives the following rough FWHM estimates of a confocal microscope's ability to resolve two points [66]:

$$\Delta r = \frac{0.431\lambda}{NA} \quad (2.5)$$

$$\Delta z = n \cdot \frac{\lambda}{NA^2} \quad (2.6)$$

where n is the index of refraction for the material in which imaging is performed. These estimates should be used with care since they do not account for the magnification of a multiple lens systems, errors within the system, and the use of a non-infinitely small pinhole.

Since it is impossible to use an infinitely small detector, the PSFs above are only approximations of real system performance. Wilson did a study where he examined the performance of confocal systems as the normalized pinhole radius (found by substituting the real pinhole radius into (2.1)) increased [67]. He found that lateral resolution was very sensitive to increasing pinhole radius and must be kept less than 0.5 optical units (defined as the product of the sample attenuation coefficient and depth within the sample) in order to obtain the full confocal resolution improvement [68]. On the other hand, axial

resolution remained practically constant until the pinhole radius exceeded 2.5 optical units. Since all of these calculations were done assuming a single lens system, he recommends that the designer concentrate on optimizing optical sectioning and guarantee that the following inequality is met:

$$\frac{M}{NA_p} \geq \frac{\pi d_o}{2.5\lambda} \quad (2.7)$$

where M is the total magnification of the lenses between the sample and the pinhole, NA_p is the pinhole's NA, and d_o is the actual diameter of the pinhole [68].

The addition of fiber optics to a confocal microscope changes how the size of the detector affects the system. The use of optical fiber(s) in the illumination path, the detection path, or both is popular due to the compact components that it allows the designer to use (e.g., a fiber coupler as a beamsplitter) and its flexible, low loss transport of light that supports isolation of noisy sources and endoscopic systems. When optical fibers are used in place of a detector pinhole, they have a fundamental effect on the system. First of all, imaging is always coherent because the detected field is given by the overlap integral between the field at the fiber face and the mode pattern, given that a single-mode fiber is used [69]. Also, using a single-mode fiber puts a strict limit on fiber radius that is a function of λ and commercial availability. For example, if an 855 nm source is used, the most readily available fiber has a core radius of 5 microns. In [70], Gu examined how the use of optical fibers in both the illumination and the detection path would affect confocal resolution in a single lens system. He defined a dimensionless fiber spot size parameter, A :

$$A = \left(\frac{2\pi r_o NA_c}{\lambda} \right)^2, \quad r_o = \frac{\rho}{(2 \ln V)^{1/2}} \quad (2.8)$$

where NA_c is the NA of the lens used to collimate light from the fiber and r_o is the fiber spot size and is a function of the fiber's core radius, ρ , and normalized frequency, V . He derived an expression for a confocal microscope's PSF with an optical fiber [52, 70]:

$$h_{eff} = \left| \frac{A \{1 - \exp[-(A - iu)]\}}{[1 - \exp(-A)](A - iu)} \right|^2. \quad (2.9)$$

When he plotted this function, he found that axial resolutions for $A \leq 1$ are very close to ideal confocal resolution.

Careful system design using the equations above will result in a system with subcellular resolution, a requirement for detecting premalignant lesions. Another requirement is that the system be able to produce images throughout the extent of the epithelial layer. Penetration depth in confocal microscopy has been extensively examined [71-76]. Izatt used single backscatter theory to estimate that penetration depth is limited by the signal-to-background (S/B) ratio to 5 – 8 optical depths (OD), where optical depth is equal to the total attenuation coefficient, μ_t , times the depth in the tissue [71]. When multiple scattering due to deep penetration into tissue was taken into account, Schmitt found that this limit is limited by the signal-to-noise ratio (SNR) and falls to 3 – 4 ODs [72]. While Schmitt's studies were performed using large normalized pinholes of 8 to 17 optical units, his results were confirmed by Smithpeter who used experimental results to show that when a confocal system approaches ideal confocal

resolution ($v_p \leq 3$), penetration depth is limited to 3 – 4 ODs for a 0.05 index mismatch [76].

To understand what these results mean, a value for optical depth in oral mucosa is needed, which in turn requires that μ_t be known. If the source's wavelength is limited to the near infrared (NIR) region, absorption becomes negligible and it can be assumed that μ_t is equal to the scattering coefficient, μ_s . We recently completed a study of tissue scattering coefficients for cervical epithelium including both normal and high grade cervical intraepithelial neoplasia (CIN 3) [77]. The mean scattering coefficient for CIN 3 of 69 cm^{-1} was significantly higher than the mean value for normal of 22 cm^{-1} . Using a scattering coefficient of 69 cm^{-1} gives an estimated maximum penetration depth of 450 – 600 microns for confocal microscopy. Actual reported penetration depths are well below this estimate, varying from 200 microns in amelanotic tissue [38] and human skin [78] to 490 microns in the lip (achieved through use of a low NA objective) [44].

2.5.2 *Optical coherence tomography*

OCT is an optical imaging technique capable of building two-dimensional reflectance maps from small signals within a scattering medium. The technique is an offshoot of optical coherence-domain reflectometry (OCDR), a one-dimensional ranging technique used extensively in measuring the eye [48]. OCT was also very successful in imaging the transparent tissue in the eye [79-83], but has also been used to image highly scattering media such as tissue and skin [46, 47, 49-51, 84-90].

OCT is very similar to ultrasound, measuring the intensity of reflected light rather than sound waves [88]. Since time of flight data for light cannot be measured directly,

interferometric techniques are used. A basic OCT system is shown in Figure 2.4. While many improvements have been made to this system to increase its image acquisition speed, penetration depth, and resolution, the basic components remain the same. Light from a NIR laser is split into a reference and sample arm by a Michelson interferometer (the 50/50 coupler in Figure 2.4) which then recombines reflected light from the two arms into one signal. An interferometric signal is only detected when the reflections are nearly matched in group delay [91]. The use of a broadband source with its correspondingly low coherence means that the interferometric signal falls off rapidly as the difference between the two arm delays increases. OCT performs multiple longitudinal scans (typically by scanning the reference arm position) with the sample arm's optical beam moved laterally between scans [48] to build two-dimensional images perpendicular to the tissue's surface.

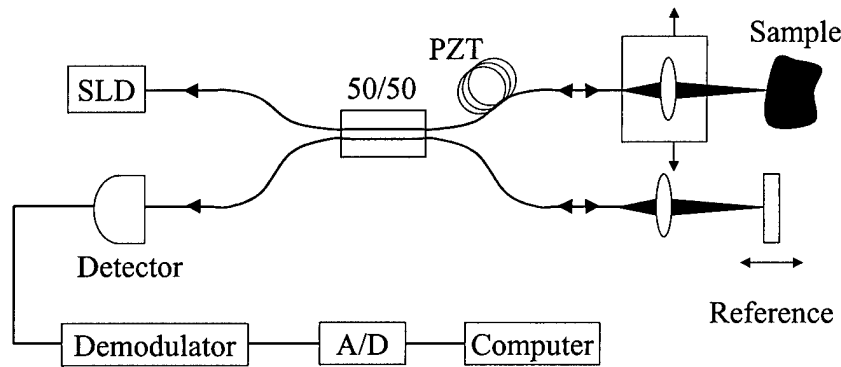


Figure 2.4. Schematic of an OCT System [48].

The system's axial resolution is directly related to the coherence length of the source. For an ideal mirror in the sample, the interferometric detector signal (after the DC component is filtered out) is proportional to the source's autocorrelation function [59]. Most papers assume that the source has a Gaussian spectrum with a FWHM

bandwidth, $\Delta\lambda$, and a center wavelength, λ_o , resulting in an autocorrelation function of [59]:

$$R_{ii}(\Delta l) = \exp \left\{ - \left[\frac{\Delta l}{(l_c/2\sqrt{\ln 2})} \right]^2 \right\} \cdot \cos(2k_o \Delta l), \quad (2.10)$$

where l_c is the source's coherence length and an OCT's axial resolution is:

$$l_c = \frac{2 \ln(2)}{\pi} \frac{\lambda^2}{\Delta \lambda}. \quad (2.11)$$

For example, a superluminescent diode (SLD) with a center wavelength at 855 nm and a bandwidth of 25 nm results in an axial resolution of 12.9 microns. Lateral resolution is determined by the optics in the sample arm. Most OCT systems sacrifice lateral resolution by using a low NA objective in order to eliminate the need to adjust the sample arm's focus during scanning [91]. This greatly simplifies instrumentation in the sample arm since it only needs to scan in one direction, making OCT a technique well suited for endoscopic applications, but severely limits its ability to perform subcellular imaging.

Another strength of OCT systems is their broad dynamic range. This comes from using optical heterodyne detection where very weak signals from the sample are mixed with strong, modulated signals from the reference arm to produce a final signal that eliminates low frequency $1/f$ mechanical noise (through demodulation) and dominates thermal noise and dark current in the detector [82, 88]. The remaining noise comes from the quantum statistics of light in the reference arm, resulting in a shot noise limited system with a SNR of:

$$SNR = \frac{1}{2} \frac{\eta}{\hbar \omega} \frac{P_s}{NEB} \quad (2.12)$$

where η is the detector's quantum efficiency, $\hbar \omega$ is the photon energy, NEB is the demodulation filter's noise equivalent bandwidth, and P_s is power at the sample [82]. SNRs of greater than 90 dB are found in the literature [82, 92, 93].

OCT's sensitivity leads to one limit on its penetration depth. SNR decreases as image depth increases until a depth is reached where single backscattered light can no longer be detected given shot noise and tissue tolerance exposure limits. Izatt estimated this limit by assuming a minimum SNR of one and solving for optical depth in terms of detector current noise characteristics and found a maximum penetration depth of 15 ODs, or 1.7 mm using the tissue property assumptions from the previous section [71]. Schmitt proposed a second limit on penetration depth in [94]. He found that contrast within the image was lost when interferometric signal from backscattered light, which produces noise in OCT and increases as the image goes deeper, becomes greater than interferometric signal from single-backscattered light. He estimated this limit by assuming that all light reaching the focal plane is unscattered or multiply forward scattered and solving for the ratio of the photocurrents generated by the two sets. This resulted in an estimate of 9 ODs, or approximately 1 mm in epithelial tissue. Both estimates well exceed the amount of penetration depth needed to image epithelium in the oral cavity.

2.5.3 Optical coherence microscopy

Optical coherence microscopy attempts to combine the advantages of both confocal microscopy and OCT to perform subcellular imaging at deep penetration depths. There are two ways of thinking about the technique: 1) as an *en-face* scanning OCT with high NA optics in the sample arm, or 2) as a confocal microscope combined with heterodyne detection and a broadband source. While OCM systems are more complicated than OCT systems or confocal microscopes, gains in lateral resolution and penetration depth give them superior performance in detecting premalignant cancers.

Many groups have built instruments with components of an OCM system. Bashkansky [54, 57, 95], Beaurepaire [96], Podoleanu [60, 97-101], and Xu [53] have all demonstrated OCT systems capable of producing *en face* images, but their systems still use low NA optics in the sample arm. Beaurepaire did report an *en face* imaging, high NA system, but he did not use modulation to allow heterodyne detection [55]. On the other hand, Schmitt introduced a system with dynamic depth focusing and high NA optics, but the instrument was only capable of producing longitudinal scans [102]. Izatt's group was the first to describe an OCM encompassing all of the traits listed above [59, 71], with an improved, faster system discussed in [52, 103]. His work was followed by Hoeling who developed another fully capable OCM used to image embryos [58] and plant cells [58, 104].

System performance in an OCM is a combination of the performance discussed in the previous two sections. The confocal microscope in the sample arm once again determines lateral resolution. Penetration depth will be similar to an OCT system due to

the coherence gate and heterodyne detection and should have the same limits as discussed in the previous section. Finding its axial resolution is more complicated though since it is determined by the overlap of a confocal microscope's PSF and the broadband source's autocorrelation function, as defined by (2.9) and (2.11) respectively. Experimental results for an OCM using a 40x, 0.65 NA objective, measured by moving a mirror through the focal plane with the reference arm blocked (confocal) and unblocked (coherence gate), are shown in Figure 2.5. Near the focus, at zero mirror displacement from the focal plane, the confocal spatial filter dominates the response. As the mirror moves farther from the focal plane, the coherence gate rejects light incompletely rejected by the confocal response [59]. The key is that OCM combines the subcellular lateral resolution of a confocal microscope with the increased penetration depth of an OCT system.

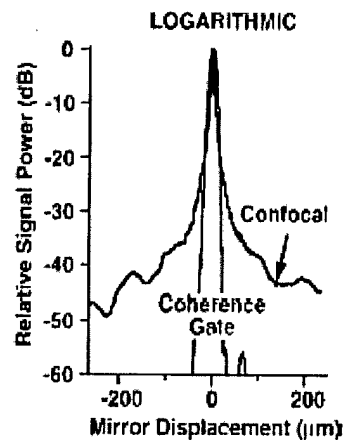


Figure 2.5. Plots of confocal and OCM response [59].

CHAPTER 3

Confocal Microscopy for Real Time Detection of Oral Cavity Neoplasia

3.1 INTRODUCTION

Confocal reflectance microscopy is a new technology that can provide detailed images of tissue architecture and cellular morphology of living tissue in near real time. In concept, *in vivo* confocal imaging resembles histologic tissue evaluation, except that 3D sub-cellular resolution is achieved non-invasively and without stains. In epithelial structure, resolution of 1 micron has been achieved with a 200-400 micron field of view and a penetration depth of up to 500 microns [38, 42, 44, 105-107]. Recently, flexible reflectance confocal microendoscopes have been described which can obtain high resolution confocal images of tissue *in vivo* in near real time [108-116]. Use of this instrument provides the potential to image oral epithelial tissues with subcellular resolution in a clinical setting.

Confocal imaging with reflected light allows for detailed images of cell morphology and tissue architecture using backscattering by various tissue components to provide contrast. In skin [37, 41, 105, 106, 117], cytoplasmic melanin provides a strong source of backscattering, enabling detailed morphologic images of epithelial cell morphology and tissue architecture throughout the entire epithelial thickness. This

technology has been used to image various types of skin pathology, including psoriasis [118], folliculitis [39], and neoplastic skin lesions [119-121]. In neoplastic skin lesions, morphologic changes in cytologic structure and microvasculature were visualized in both basal cell carcinomas and melanomas.

In amelanotic epithelial tissues, cell nuclei provide the primary source of reflected light [38, 122] captured by a reflectance confocal microscope. The backscattering from these nuclei is dramatically enhanced by addition of weak (3-6%) acetic acid [123]. Confocal imaging of oral mucosa in the lip and tongue has resolved subcellular detail at depths of 250 microns and 500 microns, respectively [44]. Recent work showed that reflectance confocal imaging of normal and precancerous cervical tissue can characterize nuclear size, nuclear density and nuclear to cytoplasmic ratio without the need for tissue sectioning or staining. Parameters extracted from confocal images could be used to discriminate high grade cervical precancers with a sensitivity of 100% and a specificity of 91% in a study of 25 samples [107]. These results underscore the potential role of this technology in clinical evaluation of oral lesions and the need for further investigations in oral tissue using multiple anatomic sites and pathologic diagnosis.

The goal of this study was to characterize the features of normal and neoplastic oral mucosa using reflectance confocal microscopy. We report results of a pilot study using near real-time reflectance confocal microscopy to image pairs of clinically normal and abnormal biopsies obtained from 17 patients. We find that confocal microscopy can image oral mucosa with resolution comparable to histology without the need for tissue fixation, sectioning or staining. Confocal images provide a detailed view of cell

morphology and tissue architecture, demonstrating features of normal epithelium, dysplasia, and squamous carcinoma. Based on these results, we recommend that reflectance confocal microscopy should be explored as a tool to improve early detection of oral cavity neoplasia, to provide real time determination of mucosal tumor margins, and to determine response to therapy.

3.2 METHODS AND MATERIALS

3.2.1 *Specimens*

Oral cavity biopsies were acquired from 17 patients at the Head and Neck Clinic of the University of Texas M. D. Anderson Cancer Center who were undergoing surgery for squamous cell carcinoma (SCC) within the oral cavity. Informed consent was given by all patients, and the project was reviewed and approved by the University of Texas M. D. Anderson Cancer Center Office of Protocol Research and the Institutional Review Board at the University of Texas at Austin. Biopsies (approximately 3 mm wide by 4 mm long by 2 mm thick) were acquired from one clinically normal appearing and one clinically suspicious area and immediately placed in growth medium (DMEM, no phenol red). Reflectance confocal images were obtained at multiple image plane depths from biopsies within six hours of excision. Following imaging, biopsies were fixed in 10% formalin and submitted for routine histologic examination by an experienced head and neck pathologist (AEN). Additional sections from each biopsy were stained with Monoclonal Mouse anti-Cytokeratin (Pan) (MMAC) Concentrate Antibody (Zymed Laboratories, Inc.), a broad spectrum monoclonal antibody cocktail of clones A1 and A3

which reacts to cytokeratins 10, 14/15, 16 and 19 in the acidic subfamily and all members of the basic subfamily, to assess correlations between confocal image features and the presence of keratin in the specimen.

3.2.2 *Confocal System*

Reflectance confocal images were obtained from each biopsy using a near real-time, epi-illumination, reflectance confocal microscope [76] (Figure 3.1). Illumination was provided by a continuous wave laser diode operating at 810 nm. A mirror system provided an image frame rate of 7.5 frames per second by scanning illumination light in the sample via a water immersion microscope objective (25X, 0.8 NA). Average illumination power was 10 – 30 mW, focused to a 1 micron-diameter spot on the sample. Light backscattered from the tissue returned to a beam splitter where it was reflected onto a pinhole lens and then spatially filtered by a 10 μm diameter pinhole aperture before being detected by an avalanche photodiode. The confocal system operated at a dimensionless pinhole radius of 2.5 to provide maximum optical sectioning for obtaining cellular detail [76]. The measured lateral and axial resolution of the system were 0.8 microns and 2-3 microns, respectively. The field of view was adjustable from 300 – 400 microns by changing the system magnification.

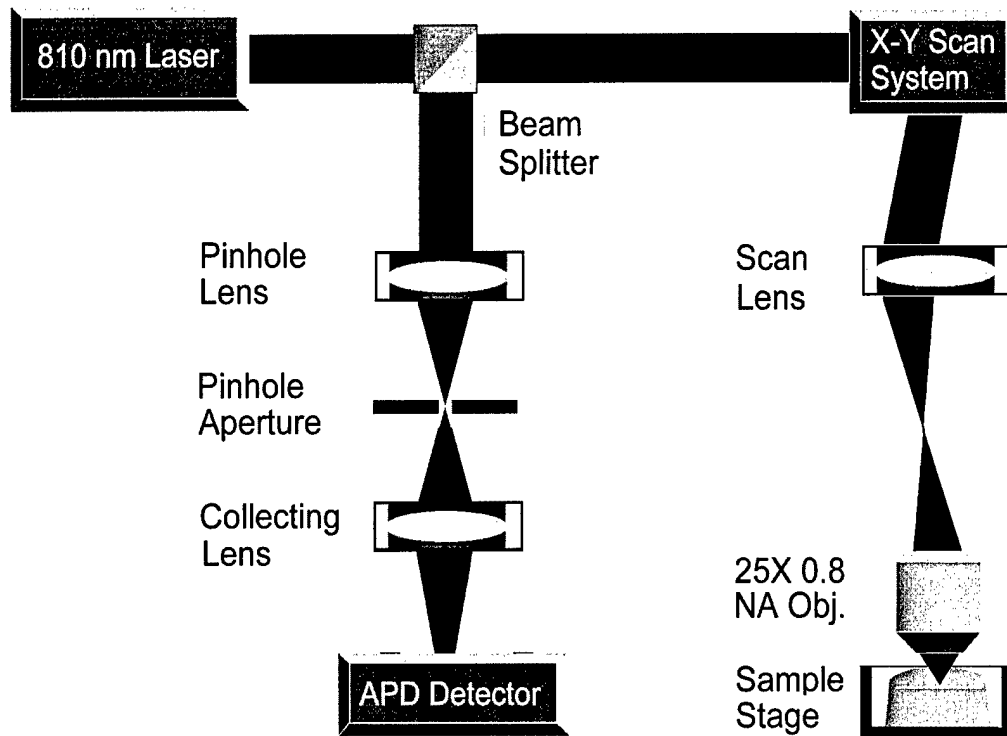


Figure 3.1. Block diagram of the near real-time reflectance confocal microscope used to image oral cavity specimens.

3.2.3 *Imaging and Image Processing*

Prior to imaging, the biopsies were removed from growth media, rinsed with phosphate buffered solution (PBS), and oriented so the image plane of the confocal microscope was parallel to the epithelial surface and would approach the epithelial layer first. A 6% solution of acetic acid was then added to each sample to increase image contrast [123]. Frames were acquired at various epithelial depths until either tissue details were no longer resolvable or up to the working distance of the microscope objective (250 microns). To contrast confocal images obtained in this 'en face'

orientation with the traditional transverse orientation, additional confocal images were acquired from one biopsy oriented so that the image plane of the confocal microscope was perpendicular to the epithelial surface and from two hundred micron thick transverse organ cultures prepared from biopsies from one patient.

Each of the confocal image frames presented here was resampled and processed to enhance image quality. Resampling was performed to reduce distortion in the images caused by nonlinearity in the resonant galvonometric scanning system while image quality was improved by increasing brightness and contrast within the images. Brightness was enhanced by adding a selected percentage of full gray scale to each pixel and contrast increased by removing another percentage of full gray scale from the image and expanding the remaining midrange gray levels. Brightness and contrast for all confocal images in this chapter were increased by 70% and 50%, respectively. Confocal images from the transverse tissues slices were also tiled together to provide large-scale mosaic views of each slice.

Images of stained histologic sections were acquired using a color CCD camera coupled to a brightfield microscope. Reflectance confocal images were compared to histologic images from the same sample to determine which tissue features contribute to image contrast and can be potentially imaged using *in vivo* confocal microscopy. The confocal microscope's small field of view makes it extremely difficult to register exactly where in the biopsy images were acquired so we identified areas in histologic sections that corresponded to features present in our confocal images.

3.3 RESULTS

Images were successfully obtained from specimens from 15 of 17 biopsy pairs with resolution similar to that provided by bright-field microscopy typically used to examine histologic sections; data could not be obtained from two patient specimens due to instrument errors, and these were not included in further analyses. Table 3.1 shows the number of clinically normal and abnormal specimens obtained from each site within the oral cavity. Table 3.2 lists the histopathologic diagnoses for each biopsy from each patient with 15 showing hyperkeratosis or parakeratosis, six exhibiting hyperplasia, one with dysplasia, nine moderately differentiated SCCs, one well differentiated SCC, and three specimens having no diagnosis due to the lack of epithelium in the histologic section.

Table 3.1. Number of clinically normal and abnormal biopsies from each site.

Location	Clinical Appearance	
	Normal	Abnormal
Tongue (Lateral and Ventral Surfaces)	8	8
Floor of Mouth	2	2
Gingiva	2	3
Buccal Mucosa	2	1
Soft Palate	1	1

Table 3.2. Histopathologic diagnosis by patient.

Pat.	Site	Histopathologic Diagnosis	
		Clinically Normal Biopsy	Clinically Abnormal Biopsy
1	Tongue (lateral surface)	Hyperkeratosis	Moderately differentiated SCC
2	Buccal mucosa	Hyperkeratosis	Moderately differentiated SCC
3	Floor of mouth	Mild hyperkeratosis	Hyperkeratosis, hyperplasia
4	Tongue (lateral surface)	Mild hyperplasia	Moderately differentiated SCC
5	Tongue (ventral surface)	Hyperkeratosis	Extreme hyperkeratosis
6	Tongue (lateral surface)	Mild hyperplasia	Moderately differentiated SCC
7	Gingiva	None ¹	Well differentiated SCC
8	Gingiva	Mild hyperkeratosis	Moderately differentiated SCC
9	Tongue (lateral surface)	Hyperkeratosis	Moderately differentiated SCC
10	Tongue (ventral surface)	Hyperkeratosis	None ¹
11	Tongue (lateral surface)	Hyperkeratosis, hyperplasia	None ¹
12	Floor of mouth	Hyperkeratosis, hyperplasia	Moderately differentiated SCC
13	Tongue (lateral surface)	Parakeratosis, hyperplasia	Moderately differentiated SCC
14	Soft Palate	Hyperkeratosis	Moderately differentiated SCC
15	Gingiva	Hyperkeratosis	Mild dysplasia hyperkeratotic

¹No epithelium in specimen.

Figure 3.2 shows a comparison of histologic (Figure 3.2A) and confocal (Figure 3.2B) images from the 200 micron thick transverse organ cultures obtained from the normal gingiva biopsy. In the confocal image mosaic, epithelial cell nuclei are apparent throughout the mucosa with the epithelial stromal junction clearly visible (double arrows). In the stroma, connective tissue and fibroblast nuclei (arrow) can be visualized. Figure 3.2 also shows histologic (Figure 3.2C) and confocal (Figure 3.2D) images of a tongue biopsy with the confocal image plane oriented perpendicular to the epithelial surface. Again, the confocal image shows epithelial nuclei throughout the epithelium; tissue architecture and cell morphology assessed by reflectance confocal microscopy compare well to that assessed by histology.

In clinical applications, reflectance confocal images would be obtained with the image plane parallel to the epithelial surface. Figure 3.3 shows reflectance confocal images obtained in this orientation at different depths beneath the surface of the epithelium. The confocal image from the superficial epithelium (Figure 3.3B) shows larger cells with condensed nuclei, while the confocal image obtained 50 microns beneath the epithelial surface (Figure 3.3C) shows uniform, smaller intermediate epithelial cells. The confocal image of the basal epithelium (Figure 3.3D) shows a distinct increase in cell density and nuclear to cytoplasmic ratio. Confocal image features compare well with the corresponding transverse histologic section (Figure 3.3A). This pattern of confocal images was typical of those recorded from normal biopsies in this study.

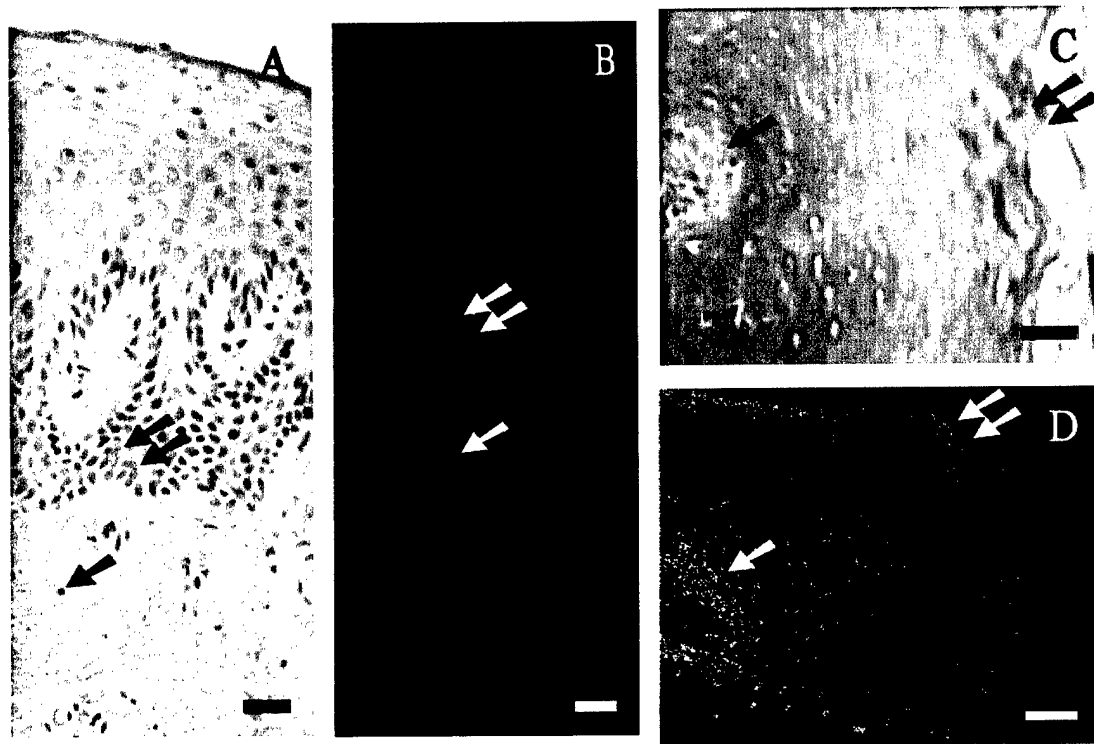


Figure 3.2. Comparison of confocal images to histologic sections. The histology section (A) and mosaic of confocal images (B) from a 200 micron thick transverse organ culture of a normal gingiva biopsy show epithelium and stroma; the basal epithelial nuclei are readily apparent at the epithelial stromal junction (double arrows). Epithelial cell nuclei and fibroblast nuclei (single arrow) are resolved. The histology section (C) and transverse confocal image (D) of a hyperkeratotic tongue biopsy show epithelial cell nuclei from superficial epithelium on the right (double arrows) to the basal layer (single arrow) on the left. Scale bars = 50 microns.

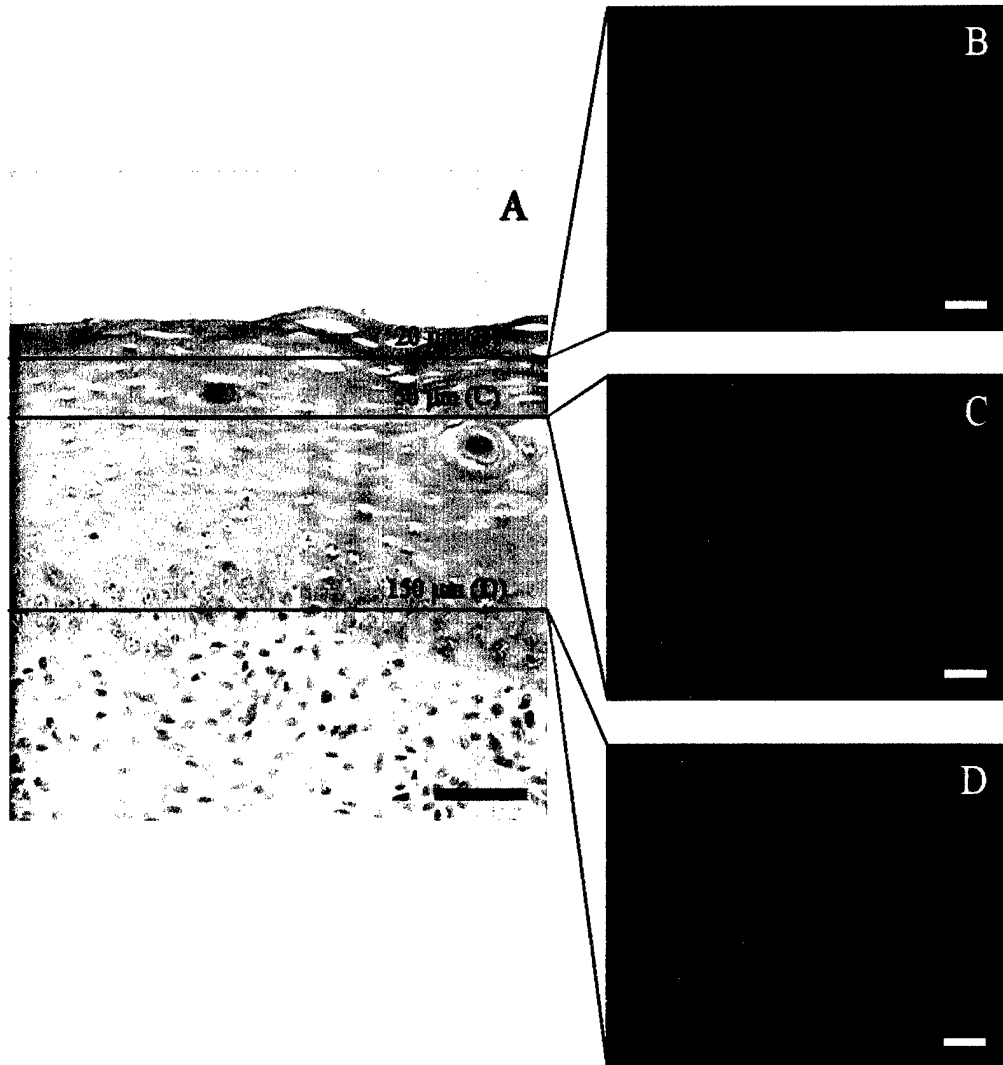


Figure 3.3. Transverse histologic image (A) and en face confocal images (B-D) obtained at different depths beneath the epithelial surface from hyperkeratotic tissue from the ventral tongue surface. Nuclear density, cell size, and cytoplasmic scattering change as the depth of the focal plane increases from (B) 20 microns to (C) 50 microns to (D) 150 microns beneath the epithelial surface. Scale bars = 50 microns.

In contrast, Figures 3.4 – 3.8 show images that illustrate the features of SCCs with confocal microscopy. Figure 3.4 shows histologic (Figure 3.4A, B) and confocal images (Figure 3.4C) of a moderately differentiated SCC from the lateral surface of the tongue. Extensive variations in cell size, nuclear size and nuclear morphology are resolved in both the histologic section (Figure 3.4B) and a confocal image taken 100 microns below the epithelial surface (Figure 3.4C). Epithelial nuclei (single arrows) appear as bright areas on the confocal image, whereas areas of stroma with inflammation (double arrows) appear dark in the confocal image. Similarly, the histologic (Figure 3.5A, B, D) and confocal images (Figure 3.5C, E) of invasive SCC of the soft palate show regions of tumor cells (single arrows) and interspersed regions of stroma containing inflammatory cells (double arrows). Confocal images obtained 100 microns beneath the epithelial surface show strong backscattering from tumor cell nuclei and dark regions corresponding to areas of inflammation. Nuclear density as assessed by confocal microscopy in the SCCs of Figures 3.4 and 3.5 is clearly higher than in the normal tissue displayed in Figure 3.3.

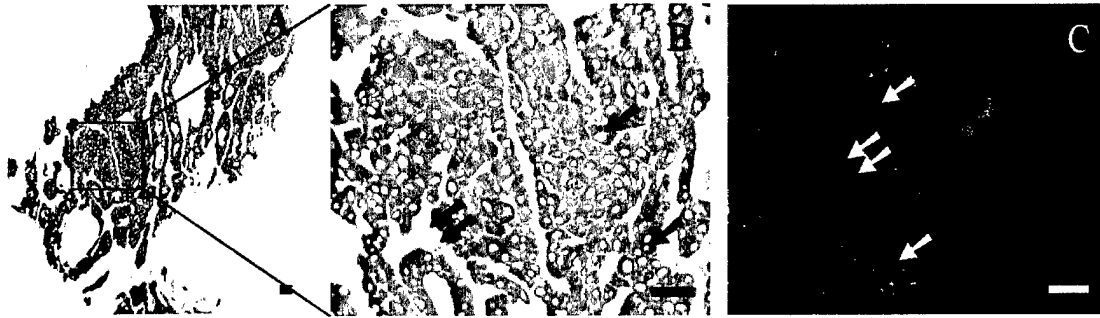


Figure 3.4. Histologic and confocal images of a moderately differentiated SCC from the lateral surface of the tongue. (A) Low magnification image of a keratin antibody (MMAC) stained section showing tumor cells interspersed with stroma containing inflammation (2.5X objective). (B) High magnification image of tumor cells (single arrows) containing pleomorphic nuclei and stroma with inflammation (double arrows). (C) Confocal image taken 100 microns below the epithelial surface illustrating pleomorphic nuclei (single arrows) and dark areas corresponding to stroma containing inflammation (double arrows). Scale bars = 50 microns.

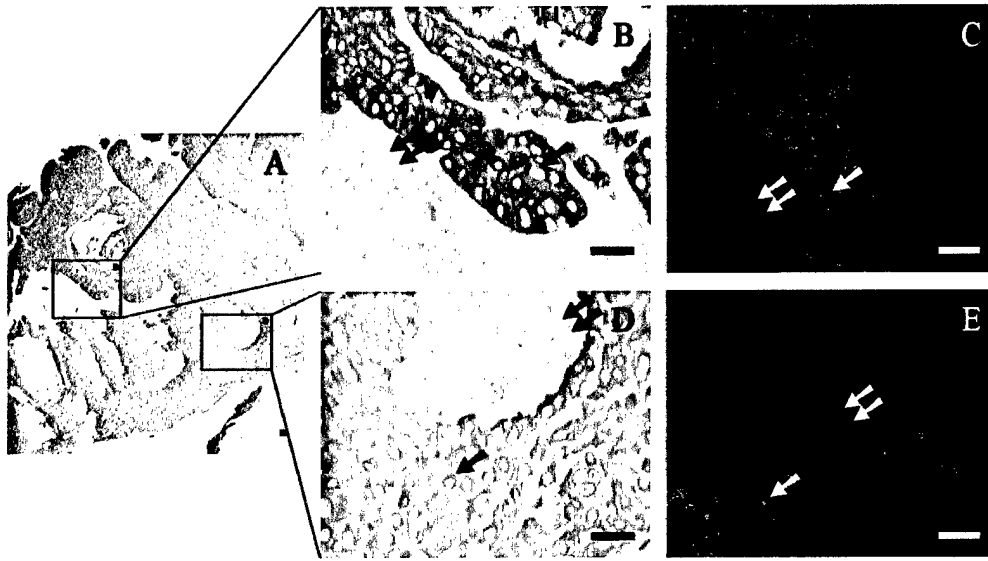


Figure 3.5. Confocal and histologic images of invasive SCC of the soft palate. (A) Low magnification image of a keratin antibody (MMAC) stained section showing extensive tumor cells surrounding areas of stroma with inflammation (2.5X objective). (B) High magnification image of keratinized, tightly packed tumor cells (single arrow) with stroma containing inflammation (double arrows) (20X objective). (C) Confocal image taken 100 microns below the surface of tightly packed, highly scattering tumor cells (single arrow) with dark areas of stroma with inflammation (double arrows). (D) High magnification histologic image of less keratinized, larger tumor cells (single arrow) with stroma containing inflammation (double arrows) (20X objective). (E) Confocal image taken 100 microns below the surface with larger cells (single arrow) and less background scattering combined with dark areas of stroma with inflammation (double arrows). Scale bars = 50 microns.

Figure 3.6 shows histologic and confocal images from a moderately differentiated SCC from the buccal mucosa. Increased keratinization in tumor cells is noted in histologic (Figure 3.6B) and confocal images (Figure 3.6C) as higher signal return from cytoplasmic, nonnuclear areas (single arrows). Large, homogeneous keratin pearls (Figure 3.6D, E) were visible in confocal images as areas of high return with a speckled appearance (single arrows). These features were also observed in images of a well differentiated SCC from the gingiva (Figure 3.7). The confocal images show both keratin pearls (double arrows) (Figure 3.7C) and tumor cells (single arrows) surrounded by smaller keratin pearls (Figure 3.7E). Confocal image features compare well with corresponding histologic images.

In addition to tumor cells and keratin, confocal imaging identified other features in normal and neoplastic oral tissues. Figure 3.8 shows images from a moderately differentiated SCC from the lateral surface of the tongue. Figure 3.8B and C show histologic and confocal images of muscle fibers (single arrows); the muscle fibers do not strongly scatter light and appear dark in the confocal image. Areas of fibrosis in the tumor are clearly discernible in histologic (Figure 3.8D) and confocal images (Figure 3.8E). Confocal images of fibrosis show scattering from individual fibers (double arrows) as well as elongated fibroblast nuclei (single arrows). Figure 3.9 shows images from salivary glands (single arrows) in a biopsy specimen from the floor of the mouth. Confocal images of these glands are characterized by bright return from serous demilunes containing serous secreting cells surrounding darker regions of low return from mucous-secreting units [124].

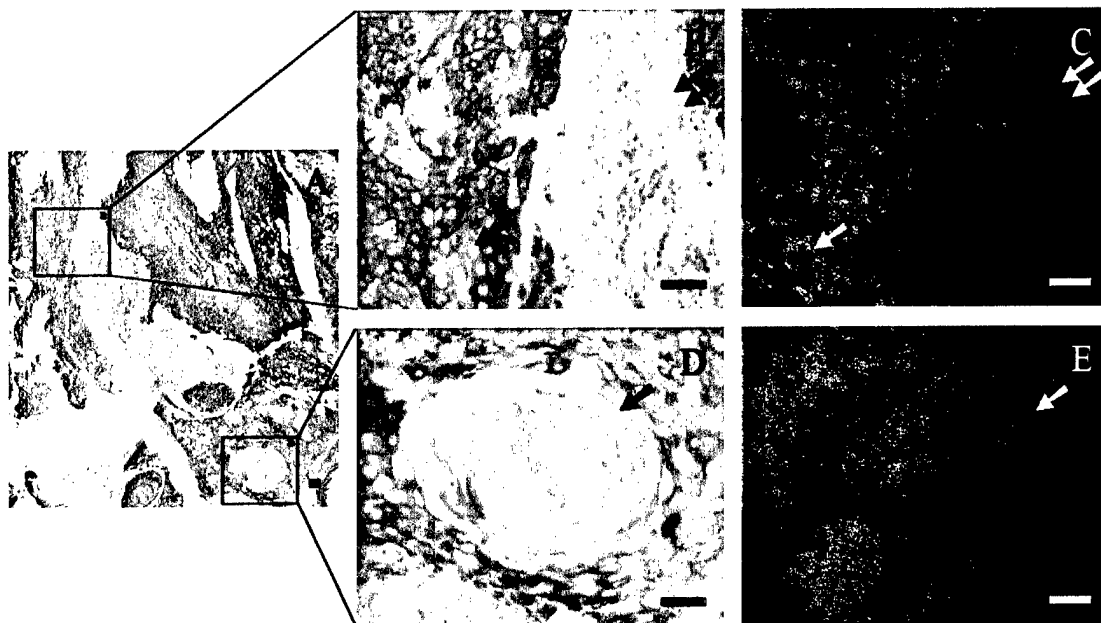


Figure 3.6. Images of a moderately differentiated SCC from the buccal mucosa. (A) Low magnification image of a keratin antibody (MMAC) stained section showing keratin pearls, highly keratinized tumor cells, and stroma with inflammation (2.5X objective). (B) High magnification histologic image of tumor cells (single arrow) and stroma containing inflammation (double arrows) (20X objective). (C) Confocal image taken 200 microns below the epithelial surface showing dark regions of stroma with inflammation (double arrows) alternating with tightly packed tumor cells (single arrow) containing irregular nuclei. (D) High magnification histologic image of a keratin pearl (single arrow) (20X objective). (E) Confocal image of a keratin pearl (single arrow) taken 50 microns below the surface showing the highly reflective, speckled appearance characteristic of keratin. Scale bars = 50 microns.

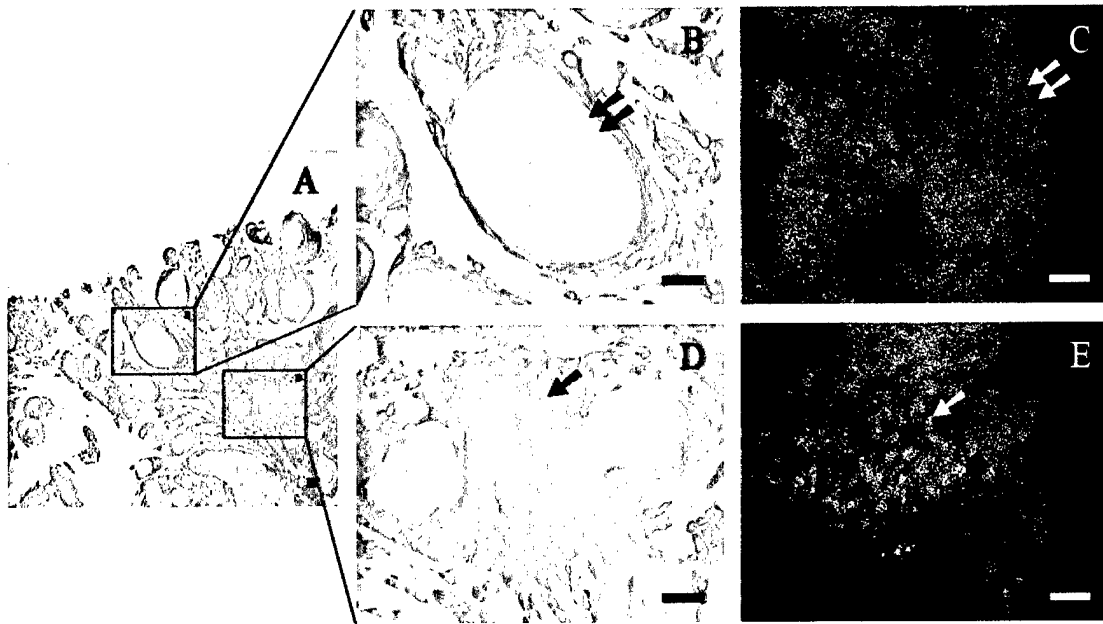


Figure 3.7. Images of a well differentiated SCC from the gingiva. (A) Low magnification image of a keratin antibody (MMAC) stained section showing tumor cells and keratin pearls interspersed with stroma containing inflammation (2.5X objective). (B) High magnification histologic image of a keratin pearl (double arrows) (20X objective). (C) Confocal image taken 50 microns below the surface containing highly reflective keratin (double arrows). (D) High magnification histologic image of keratin pearls with highly keratinized tumor cells (single arrow) (20X objective). (E) Confocal image taken 50 microns below the surface containing areas of highly reflective keratin with nuclei (single arrow). Scale bars = 50 microns.

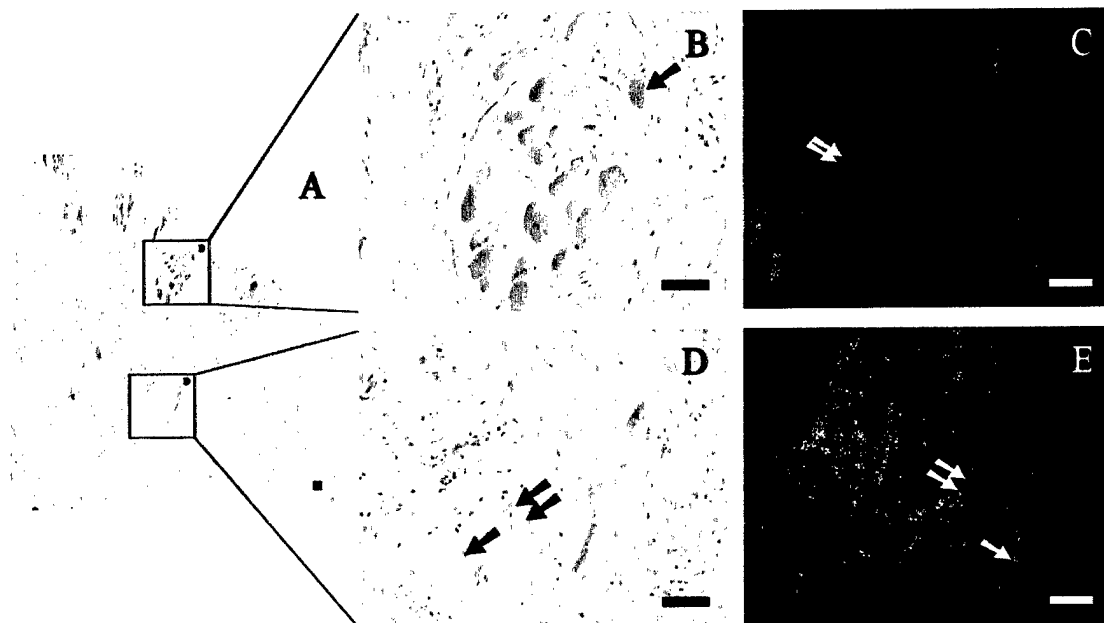


Figure 3.8. Images of a muscle and fibrosis from a moderately differentiated SCC from the lateral surface of the tongue. (A) Low magnification image of an H&E section shows skeletal muscle and extensive fibrosis (2.5X objective). (B) High magnification histologic image of muscle (single arrow) (20X objective). (C) Confocal image of muscle (single arrow) taken 100 microns below the surface. (D) High magnification histologic image of fibrosis (double arrows) with elongated fibroblast nuclei (single arrow) (20X objective). (E) Confocal image of fibrosis (double arrows) taken 50 microns below the surface illustrating reflectance from structural protein fibers and containing elongated fibroblast nuclei (single arrow). Scale bars = 50 microns.

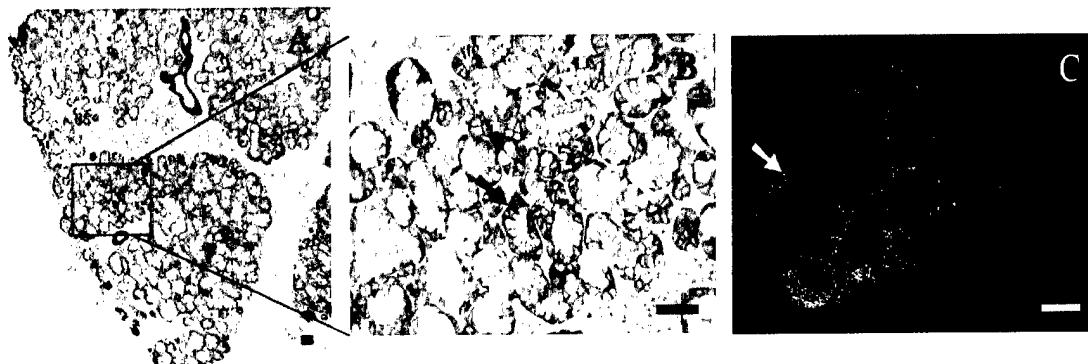


Figure 3.9. Images of salivary glands from the floor of the mouth. (A) Low magnification image of a keratin antibody (MMAC) stained section showing extensive salivary glands (2.5X objective). (B) High magnification histologic image of salivary glands (single arrow) (20X objective). (C) Confocal image of salivary glands (single arrow) taken 50 microns below the surface. Scale bars = 50 microns.

An important performance measure for confocal imaging *in vivo* is the maximum depth at which images can be obtained, or “penetration depth.” We observed a wide variation in penetration depth throughout this study. We analyzed image stacks from 13 normal samples in which confocal images throughout the epithelium were captured, and we were able to image up to the confocal microscope’s working distance (250 microns) 31% of the time. In 46% of the cases, penetration depth was between 150 – 200 microns, while 23% of the time, penetration depth was 100 – 150 microns. We hypothesize that increased levels of keratin, particularly in the superficial epithelium, can limit the ability of illumination light to penetrate to lower depths due to the high refractive index of keratin compared to cytoplasm ($n_{\text{keratin}} = 1.54$ [125] versus $n_{\text{cytoplasm}} = 1.37$ [126]).

3.4 DISCUSSION

The confocal images presented here illustrate the ability of reflectance confocal microscopy to image oral mucosa with resolution comparable to histologic evaluation without tissue preparation and staining. In normal tissue, depth-related changes in cell diameter and nuclear density were observed at multiple anatomic sites within the oral cavity. In SCCs, densely packed, pleomorphic tumor nuclei could be visualized with distinct differences in nuclear density and morphology distinguishable between confocal images of neoplastic and non-neoplastic oral cavity. Other features of non-cancerous and cancerous oral tissue that could be identified in the confocal images included areas of inflammation, fibrosis, muscle fibers and salivary glands. Areas of inflammation appear dark in confocal images of the oral cavity.

The images reported here show similar features in the oral cavity to those reported by White *et al* [44]. In that study, images of the superficial epithelial layers of the lip and anterior tongue were acquired at depths of up to 490 μm and 250 μm , respectively. Cell nuclei and membranes were clearly resolved in the epithelial layers, correlating well with histology. The use of a low power objective (30X) allowed the capture of different structures in the lamina propria including collagen fibers and blood vessels. The study presented here provides a more comprehensive survey of the morphologic features that can be measured using reflectance confocal microscopy from oral sites such as the floor of the mouth, gingiva, buccal mucosa, soft palate and lateral surfaces of the tongue, and how these features change with the development of SCC.

Confocal microscopy can provide images of many important cellular and architectural features of SCC. While the images presented here were obtained from biopsies measured immediately after excision, we have recently described a fiber optic reflectance confocal microscope that has been used to obtain images of the oral cavity *in vivo* [108, 109]. This flexible confocal microendoscope is small enough that it can be used to examine sites throughout the oral cavity. The tip of the endoscope is placed in contact with the tissue to be imaged. A small drop of saline provides index matching between the tip of the endoscope and the tissue. Weak suction is applied at the distal tip of the microendoscope to pull the tissue up through the image plane of the confocal microscope, to easily obtain images at different depths beneath the surface of the epithelium.

The ability to obtain such images *in vivo* and at near real time suggests several potential clinical applications for reflectance confocal microscopy such as noninvasive diagnosis of oral lesions and the ability to determine tumor margins *in vivo* in real time. Visual inspection and palpation remain the standard methods used to assess the extent of mucosal involvement by carcinomas and premalignant lesions. However, molecular and pathologic assessments of “normal appearing” mucosa have revealed molecular and cellular changes in these tissues, illustrating the fallibility of visual detection of dysplasia even by highly trained clinicians [127, 128]. To compensate for the limitation of surgeons to determine exactly the margins of carcinoma or dysplasia, it is accepted practice to resect a large cuff (approximately 1-2 cm.) of normal appearing mucosa around the visibly abnormal tissue. This produces better likelihood of complete excision,

but increased postoperative morbidity due to the greater amount of tissue removed. In tertiary care centers, problems caused by the inability to visually distinguish the margins of carcinoma and dysplasia is ameliorated by the use of frozen section to analyze edges of the resection using light microscopy. However, accurate frozen section analysis is time consuming, costly, dependent on the experience and skill of the histotechnician and pathologist, and not available in unspecialized medical facilities. Thus, technological advancements such as *in vivo* confocal imaging that improve the ability of surgeons to accurately identify tumor margins in real time could have substantial benefit for patients. As our results demonstrate, *in vivo* confocal imaging has the potential to assess features of normal mucosa and SCC, and may yield a very attractive alternative method to assess the status of mucosal margins, through its capability to visualize cellular morphology, and tissue architecture in real time without the need for sectioning and staining. Significant time and cost savings through the use of confocal examination of frozen sections from Mohs micrographic surgery for excision of nonmelanoma skin cancers have already been noted by Rajadhyaksha *et al* [129]. We acknowledge that a limitation of *in vivo* confocal microscopy is penetration depth and therefore its inability to assess the deep margin of a large, invasive tumor. In addition, verrucous lesions with extreme hyperkeratosis may not permit adequate light penetration to visualize the epithelial stromal border.

Achieving the clinical potential of *in vivo* confocal imaging will require further characterization of the cellular and architectural features of oral tissue that are visible with confocal microscopy and assessment of how they match standard histologic

examination. This includes imaging of more dysplastic lesions and the evaluation of the efficiency of confocal imaging in the clinical assessment of margin involvement and response to treatment. Two primary challenges must be addressed in these studies. The first is to obtain images *in vivo* and assess their image characteristics in comparison to our previous results and standard histologic examination; we have just commenced an *in vivo* pilot study of fiber optic reflectance confocal microscopy of oral lesions. The second is to explore methods that can increase the penetration depth at which good quality confocal images can be obtained. We are studying methods to increase penetration depth through the use of additional signal filtering techniques such as coherence gating to better isolate backscattered light from our focal plane [59] and chemical agents such as glucose and glycerol to improve index matching at the surface [44, 130].

3.5 CONCLUSION

In this study, we have shown the power of reflectance confocal microscopy to visualize, at the subcellular level, features of both normal and neoplastic oral mucosa throughout the oral cavity as well as the composition of SCCs with varying differentiation levels. Our results support the potential for this tool to play a significant role in the clinical evaluation of oral lesions, real-time identification of tumor margins, and monitoring of response to therapeutic treatment.

CHAPTER 4

Confocal Microscopy for Diagnosis of Oral Cavity Preneoplasia and Neoplasia

4.1 INTRODUCTION

Oral cancer remains an important health issue throughout the world. In the United States, over 27,000 new cases and approximately 7,000 deaths attributable to oral cancer are expected in 2003. In some areas of the world, this malignancy is much more common; oral cancer is the most common cancer among men and the third most common cancer in women, in India [1]. Prognosis for patients diagnosed with oral cancer remains disappointingly low with five-year survival rates continuing to hover in the fiftieth percentile [2]. These low survival rates are directly linked to the significant number of oral squamous cell carcinomas that are not diagnosed until they are symptomatic, at which point they are typically larger than 2 cm and in 50% of the cases, the condition has already spread regionally to the lymph nodes [131, 132].

A primary cause of the delay in diagnosing precancerous lesions before they progress to carcinoma is the difficulty in clinically differentiating them from the many other benign oral lesions. In [4], Scully lists 32 lesions other than neoplasms that present as lumps or swellings in the mouth. Preneoplastic lesions are often painless and almost always asymptomatic [133] without the classic indicators of advanced oral cancer such as

ulceration, induration, nodularity, bleeding, and cervical adenopathy [134]. Current guidance is to perform a biopsy when a lesion has been present for over three weeks or if the patient is in a high-risk group [5], but even experienced clinicians have difficulty in selecting a representative location on the lesion for biopsy. The ability to examine oral lesions with subcellular resolution *in vivo* could allow a clinician to screen for dysplastic epithelium in order to select lesions requiring biopsy and target a representative area for biopsy.

An exciting new technology, confocal microscopy, has the ability to support clinicians by imaging cellular structures within the epithelial layer without the need for a biopsy. Confocal microscopy is an optical technique that samples small volumes of tissue producing microscopic resolution at depths up to several hundred micrometers into tissue. This resolution combined with changes in refractive index, particularly between a cell's nucleus and cytoplasm, provide details of cell and tissue morphology required for morphologic analysis of the tissue. In addition, recent advances in scanning mechanisms and miniaturized optics have enabled the technology to acquire images *in situ* in near real-time [40, 42, 44, 135-137].

The goal of this study was to assess the ability of reflectance confocal microscopy to detect the presence of precancerous changes in oral epithelium. We report results of a pilot study using reflectance confocal microscopy to image pairs of clinically normal and abnormal biopsies obtained from 22 patients. We find that confocal microscopy can image oral mucosa with the resolution required to detect morphologic changes in oral

mucosa, but variations in hyperkeratotic layer composition and thickness as well as variable epithelial depth complicate detection of precancerous changes.

4.2 METHODS AND MATERIALS

4.2.1 Specimens

Oral cavity biopsies were acquired from 22 patients at the Head and Neck Clinic of the University of Texas M. D. Anderson Cancer Center who were undergoing surgery for squamous cell carcinoma (SCC) within the oral cavity. Informed consent was given by all patients, and the project was reviewed and approved by the University of Texas M. D. Anderson Cancer Center Office of Protocol Research and the Institutional Review Board at the University of Texas at Austin. Biopsies (approximately 3 mm wide by 4 mm long by 2 mm thick) were acquired from at least one clinically normal appearing and clinically suspicious area and immediately placed in growth medium (DMEM, no phenol red). Reflectance confocal images were obtained at multiple image plane depths from biopsies within twelve hours of excision. Following imaging, biopsies were fixed in 10% formalin and submitted for routine histologic examination by an experienced head and neck pathologist. Additional sections from biopsies were stained with Monoclonal Mouse anti-Cytokeratin (Pan) (MMAC) Concentrate Antibody (Zymed Laboratories, Inc.), a broad spectrum monoclonal antibody cocktail of clones A1 and A3 which reacts to cytokeratins 10, 14/15, 16 and 19 in the acidic subfamily and all members of the basic subfamily, to assess correlations between confocal image features and the presence of keratin in the specimen.

4.2.2 *Confocal System*

Images were obtained from each biopsy using the confocal arm of an optical coherence microscope (OCM) with its reference arm blocked (Figure 4.1). Illumination was provided by a broadband superluminescent diode (Superlum Diodes, Ltd., SLD 38) operating at 850 nm with a 25 nm full-width half maximum (FWHM) bandwidth and delivered to the confocal microscope through a 50/50 coupler and a single-mode optical fiber. The illumination light was collimated to a beam diameter of 8 mm upon exciting the optical fiber and delivered to a water immersion microscope objective (40X, 0.8 NA) via a raster-scanning system. This scanning system used a resonant scanner providing an 85 Hz line scan rate and a slow scan galvanometer to move the focused light in the sample, allowing acquisition of images in 3 seconds. The objective focused light to a 1 micron-diameter spot with an average illumination power of 0.4 mW. Light backscattered from the tissue was recoupled into the optical fiber and sent to a low-noise, broadband detector (New Focus, 1801-FC). The detector signal was bandpass filtered to 250 kHz and amplified by 10 dB before being sampled by a data acquisition board (National Instruments, PCI-MIO-16E-4) in a computer.

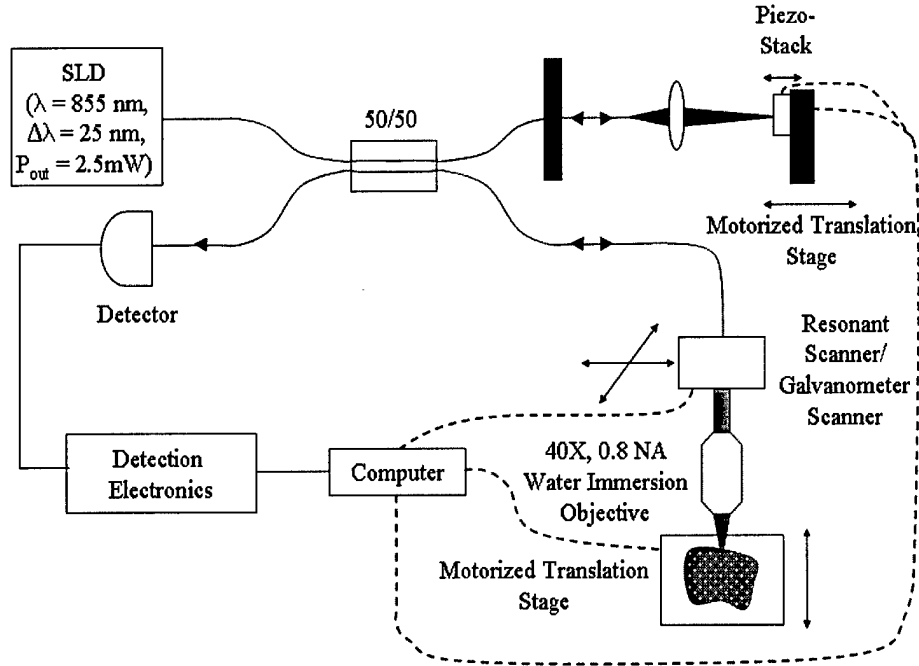


Figure 4.1. Diagram of the OCM system containing the confocal arm used to image oral cavity specimens with its reference arm blocked.

The confocal microscope system operated at a dimensionless fiber spot size, A , [70] of 2.81 to optimize optical sectioning. The measured lateral and axial resolution of the system were 2.3 microns and 5.4 microns, respectively. The field of view was adjustable from 150 – 250 microns by controlling the deflection of the scan mirrors.

4.2.3 Images and Image Processing

Prior to imaging, biopsies were removed from growth media, rinsed with phosphate buffered solution (PBS), and oriented so the image plane of the microscope was parallel to the epithelial surface and would approach the epithelial layer first. A 6% solution of acetic acid was then added to each sample to increase image contrast [123].

Confocal images were acquired at various epithelial depths until tissue details were no longer resolvable. Upon acquisition, image voltage data was saved to a file as floating point numbers and also translated into 8-bit, grayscale format using a full-scale contrast stretch algorithm to produce individual images. Each of the image frames presented here were given additional post-processing to increase image quality. Brightness was enhanced by adding a selected percentage of full gray scale to each pixel and contrast increased by removing another percentage of full gray scale from the image and expanding the remaining midrange gray levels. Descriptive statistics characterizing nuclear morphology were calculated for each image with resolvable nuclei. Binary masks outlining nuclei and the total field of view occupied by nuclei were hand-segmented by one person using a graphics editing program (JASC, Paintshop). These masks were used to extract the area of each nucleus and the area of the overall field of view, allowing calculation of mean nuclear area and nuclear to cytoplasmic ratio for each image.

Images of stained histologic sections were acquired using a color CCD camera coupled to a brightfield microscope. The small field of view of the OCM made it extremely difficult to register exactly where in the biopsy images were acquired so areas were identified in histologic sections that corresponded to features present in our images.

4.2.4 Pathologic Review of Confocal Images

Forty depth of focus stacks from 26 biopsies were selected based on image clarity, with no more than two stacks per biopsy. Depth of focus stacks were reviewed by two different groups to determine whether pathologic diagnoses could be made accurately

from confocal images of oral epithelium. The first group was comprised of 17 pathologists and pathology fellows from the Department of Pathology at the University of Texas M. D. Anderson Cancer Center. The goal of this review was to determine whether confocal images provided an adequate level of detail for a trained pathologist to diagnose dysplasia and SCC. Image stacks were placed in random order and presented to this group with information on which site in the oral cavity the sample was acquired from and the depth below the tissue surface at which each image was taken. Each reviewer was asked to classify samples as normal, dysplastic, or cancerous and, if possible, rate the severity of any detected dysplasia, based on a training set of cervical confocal images of normal epithelium and severe dysplasia from a different study [107]. A second group consisting of 10 engineering graduate students and one faculty member from the Optical Spectroscopy and Imaging Lab at the University of Texas at Austin was asked to review the same samples. This review was performed to see if individuals without formal training in pathology could detect the morphologic changes associated with dysplasia and SCC in the oral cavity. The same image stacks were used for this review, but were organized by patient. The reviewers were not informed whether the images were from a clinically normal or abnormal site, but were told which stacks were from the same patient, which site in the oral cavity the images were from, and at what depth they were acquired. The reviewers were asked to classify each sample as normal or abnormal based on the same training set used with the first group. The sensitivity and specificity for detection of neoplasia by each reviewer was calculated using histopathologic diagnosis as the standard of reference, with hyperkeratotic and hyperplastic biopsies classified as

normal and dysplastic and SCC biopsies classified as abnormal. In order to reduce error from focal variations, we removed all samples from biopsies with focal dysplasia, resulting in a sample size of 32 depth of focus stacks from 21 biopsies for analysis.

4.3 RESULTS

4.3.1 *Imaging Results*

Images were successfully obtained from 41 biopsies acquired from 18 of 22 patients with resolution similar to that provided by bright-field microscopy typically used to examine histologic sections; data could not be obtained from three patient specimens due to instrument errors and in one case, we were unable to acquire an abnormal specimen due to the small size of the lesion. Table 4.1 shows the number of clinically normal and abnormal specimens obtained from each site within the oral cavity. Table 4.2 lists the histopathologic diagnoses for each biopsy from each patient with 28 showing hyperkeratosis, 18 exhibiting hyperplasia, seven with mild dysplasia (three focal), four with moderate dysplasia (two focal), one with focal severe dysplasia, three moderately differentiated SCC, two well differentiated SCC, and four specimens having no diagnosis due to a lack of epithelium in the histologic section

Table 4.1. Number of clinically normal and abnormal biopsies from each site.

Location	Clinical Appearance	
	Normal	Abnormal
Tongue (Lateral and Ventral Surfaces)	6	6
Floor of Mouth	4	4
Gingiva	5	8
Buccal Mucosa	4	2
Soft Palate	1	1

Table 4.2. Histopathologic diagnosis by patient.

Pat.	Site	Histopathologic Diagnosis	
		Clinically Normal Biopsy	Clinically Abnormal Biopsy
1	Buccal mucosa (N1) Floor of mouth (N2) Gingiva (A)	Hyperkeratosis, hyperplasia (N1 and N2)	Moderately differentiated SCC
2	Tongue (ventral surface)	Hyperkeratosis, hyperplasia	Moderate focal dysplasia, hyperkeratosis
3	Tongue (lateral surface) (N) Floor of mouth (A)	Mild focal dysplasia	Well differentiated SCC
4	Tongue (lateral surface)	Hyperkeratosis	Mild dysplasia, hyperkeratosis
5	Gingiva	None ¹	Moderately differentiated SCC
6	Floor of mouth	Mild dysplasia, mild hyperkeratosis	Mild hyperkeratosis, hyperplasia
7	Tongue (lateral surface)	Hyperkeratosis, hyperplasia	Moderate focal dysplasia
8	Gingiva	Hyperkeratosis, hyperplasia	Hyperkeratosis, hyperplasia
9	Gingiva	Mild focal dysplasia	Moderate to severe focal dysplasia, hyperkeratosis
10a	Gingiva	None ¹	Hyperkeratosis, hyperplasia
10b	Soft Palate	Hyperkeratosis, hyperplasia	Well differentiated SCC
11	Floor of mouth (N) Gingiva (A)	Hyperkeratosis, hyperplasia	None ¹
12	Tongue (lateral surface)	Hyperkeratosis, hyperplasia	Mild focal dysplasia, hyperkeratosis
13	Floor of mouth	Mild dysplasia, hyperkeratosis	Mild to moderate dysplasia, severe hyperkeratosis
14	Tongue (lateral surface)	Severe hyperkeratosis, hyperplasia	Mild dysplasia
15	Buccal mucosa (N, A1, A2)	Hyperkeratosis, hyperplasia	Severe hyperkeratosis (A1) Hyperkeratosis, hyperplasia (A2)
16	Buccal mucosa (N) Floor of mouth (A1) Gingiva (A2)	Hyperkeratosis, hyperplasia	Moderate dysplasia, hyperkeratosis (A1) Hyperkeratosis, hyperplasia, (A2)
17	Gingiva	Hyperkeratosis, hyperplasia	Moderately differentiated SCC
18	Buccal mucosa (N) Tongue (lateral surface) (A)	Hyperkeratosis, hyperplasia	None ¹

¹No epithelium in specimen.

The confocal microscope's ability to optically section tissue empowers the acquisition of images at different depths below the epithelial surface with orientation parallel to the surface. Figure 4.2 shows images acquired from a hyperkeratotic and hyperplastic biopsy from the ventral surface of the tongue. The confocal image from the superficial layer (Figure 4.2B) shows larger cells with condensed nuclei, while the confocal image obtained 80 microns beneath the epithelial surface (Figure 4.2C) shows uniform, smaller intermediate epithelial cells. The confocal image from 120 microns below the tissue surface (Figure 4.2D) visualizes both intermediate epithelial cells and more brightly returning, tightly packed basal cells (arrow). The presence of basal cells is explained in the next confocal image from 160 microns below the tissue surface (Figure 4.2E) where the top of a rete is captured in the same region. At 200 microns below the tissue surface (Figure 4.2F), the image plane is in the stroma of this rete process, resulting in a dark region of low return (double arrows) and the top of another rete process has appeared. Confocal image features compare well with the corresponding transverse histologic section (Figure 4.2A). This pattern of confocal images was typical of those recorded from normal biopsies in this study.

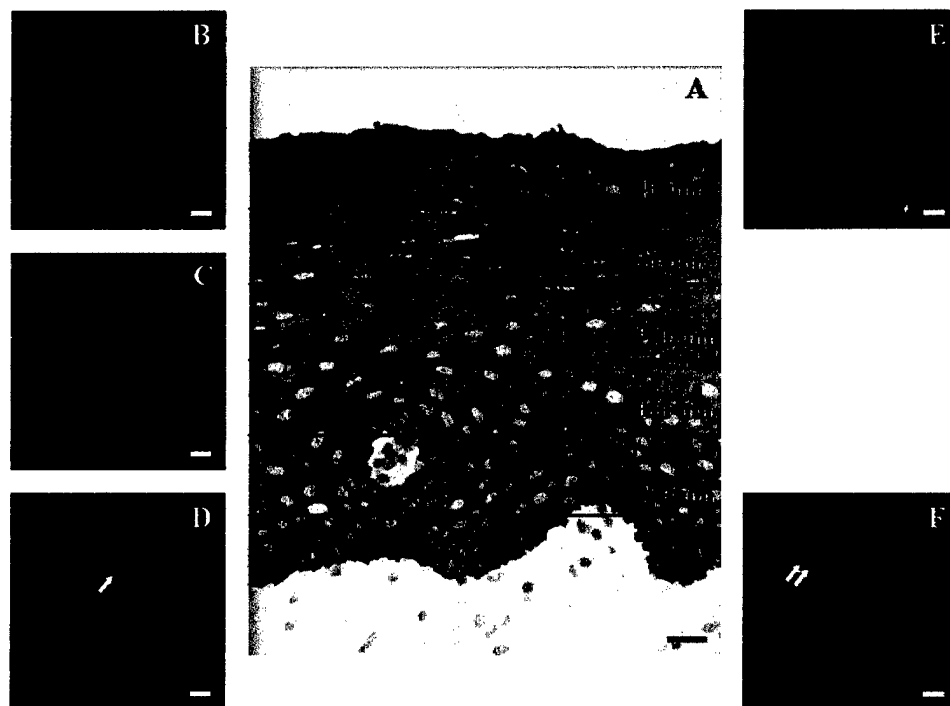


Figure 4.2. Transverse histologic section (A) with en face confocal images (B – F) obtained at different depths below the epithelial surface of a hyperkeratotic and hyperplastic biopsy from the ventral surface of the tongue. Nuclear density, cell size, and cytoplasmic scattering change as the depth of the focal plane increases from (B) 40 microns to (C) 80 microns beneath the epithelial surface, moving from the superficial layer to the intermediate. At 120 microns below the tissue surface, brightly returning basal cells appear in one portion of the image (arrow) and at (E) 160 microns, the image plane has reached the top of a rete process surrounded by these basal cells. At (F) 200 microns, another rete process appears in the bottom center of the image while a dark region of stroma occupies most of the top of the image (double arrows). Scale bars = 20 microns.

High resolution confocal endoscopes that acquire confocal images *in vivo* give this technology a potential role in clinical evaluation of oral lesions. Figure 4.3 shows an example of how a clinical evaluation of a patient's mouth might be visualized using a confocal endoscope. In Figure 4.3A, a clinically abnormal area is present in the top of the patient's soft palate (B) while a clinically normal area is apparent at the bottom of the soft palate (E). Visualization of a biopsy from the abnormal area by both histologic analysis (Figure 4.3B and C) and confocal imaging (Figure 4.3D) reveal tightly packed tumor cells (arrows) and stroma with inflammation (double arrows) consistent with the pathologic diagnosis of invasive, well differentiated cancer. In sharp contrast, examination of a biopsy from the clinically normal area (Figure 4.3E, F, and G) reveals regularly shaped nuclei (arrows) with low nuclear to cytoplasmic ratio, matching the pathologic diagnosis of hyperkeratosis and hyperplasia. In both cases, the confocal images delineate tissue architecture and cell morphology which correlates well with histology.

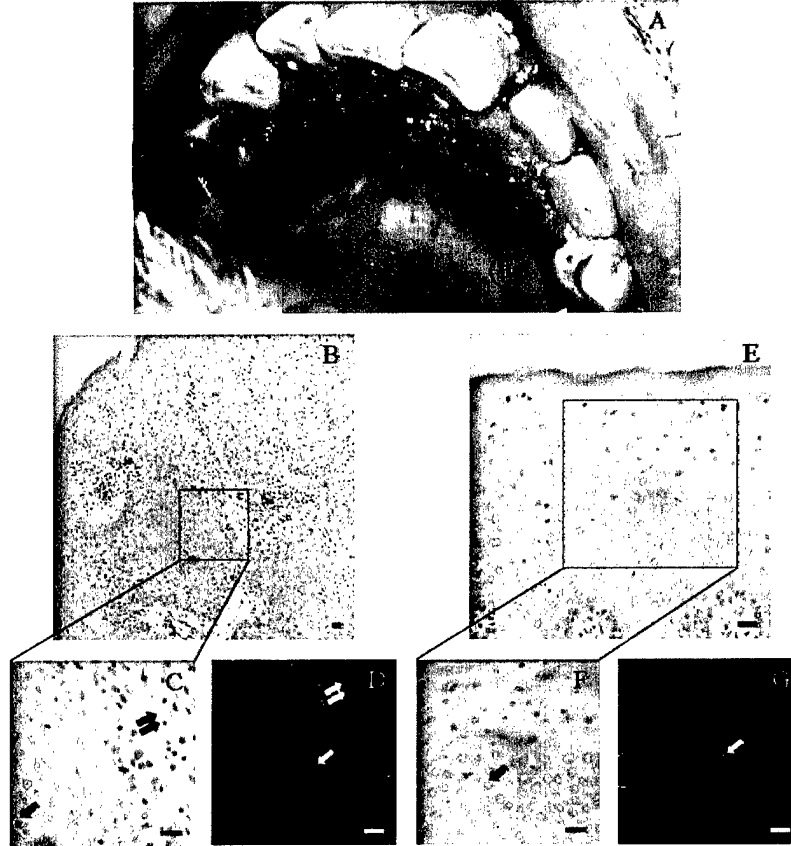


Figure 4.3. Clinical example with a macroscopic digital image of a patient's soft palate and corresponding histologic and confocal images from biopsies acquired from this patient. (A) Digital image identifying the region of the soft palate from which the abnormal (B) and normal (E) biopsies were acquired. (B) Low magnification image of an H&E section from an invasive, well differentiated SCC with tumor cells and stroma with inflammation (4X objective). (C) High magnification image of an H&E section from an invasive, well differentiated SCC with tumor cells (arrow) and stroma with inflammation (double arrows) (20X objective). (D) Confocal image taken 40 microns below the surface of an invasive, well differentiated SCC showing tightly packed tumor cells with irregular nuclei (arrow) and a dark region of stroma with inflammation (double arrows). (E) Low magnification image of an H&E section from a hyperkeratotic and hyperplastic biopsy with regularly shaped nuclei and a much lower nuclear-cytoplasmic ratio than in (B) (10X objective). (F) Low magnification image of an H&E section from a hyperkeratotic and hyperplastic biopsy with regularly shaped nuclei (arrow) and a much lower nuclear-cytoplasmic ratio than in (C) (20X objective). (G) Confocal image taken 100 microns below the surface with regularly shaped nuclei (arrow) and a much lower nuclear-cytoplasmic ratio than in (D). Scale bars = 20 microns.

4.3.2 *Nuclear Morphologic Analysis*

We reviewed the nuclear morphologic statistics extracted from confocal images to determine whether any diagnostic differentiation could be made, concentrating on nuclear to cytoplasmic ratio and average nuclear area since a similar study in the cervix had found these values to be diagnostically significant [107]. Figure 4.4 shows a scatter plot of nuclear to cytoplasmic ratio versus average nuclear area for images obtained at 50 microns below the tissue surface, a depth that provided excellent diagnostic contrast in the cervix. These parameters do not provide good separation of the normal samples, preneoplastic and neoplastic samples. Upon further review of the images, we determined that 50 microns was not deep enough to discriminate normal and dysplastic epithelium because 1) a majority of our dysplasia samples were classified as mild and therefore morphologic variations due to the dysplasia were restricted to the bottom third of the epithelium and 2) many of our samples had hyperkeratotic layers thicker than 50 microns containing irregular, condensed (pyknotic) nuclei that would introduce significant variation into the data set without correlation to dysplasia. Figure 4.5 shows a scatter plot of the nuclear to cytoplasmic ratio versus average nuclear area for a set of images selected for being from the maximum depth below the tissue surface at which nuclei were clearly and fully resolvable for a particular depth of focus stack. This set included images from a wide range of depths, from 30 microns for a highly scattering, well differentiated SCC down to 200 microns from a hyperkeratotic, hyperplastic biopsy. With this criterion, the data set should include a large number of images from close to the epithelial stromal boundary and does in fact allow a slight differentiation between normal

and dysplastic images as a function of increasing nuclear to cytoplasmic ratio and average nuclear area. This pattern continues when morphologic variation due to site is eliminated by limiting the data to just one region such as the tongue (chosen for having the most samples) as shown in Figure 4.6.

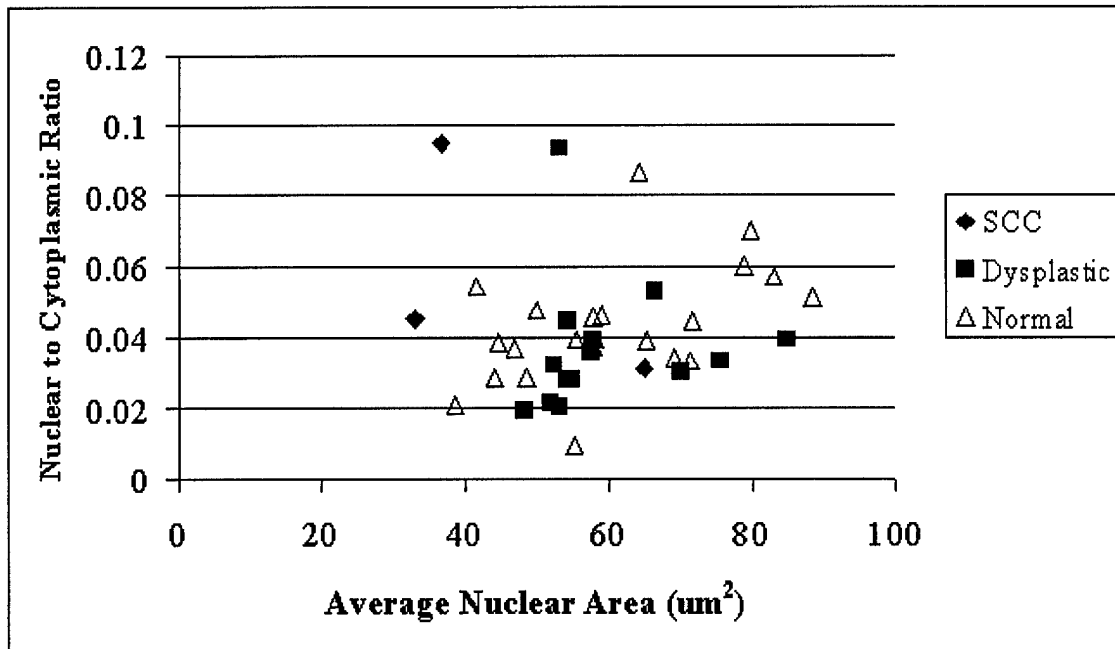


Figure 4.4. Scatter plot of nuclear to cytoplasmic ratio versus average nuclear area for images at 50 microns below the tissue surface. Images are classified as normal, dysplastic, or from SCCs based on histology.

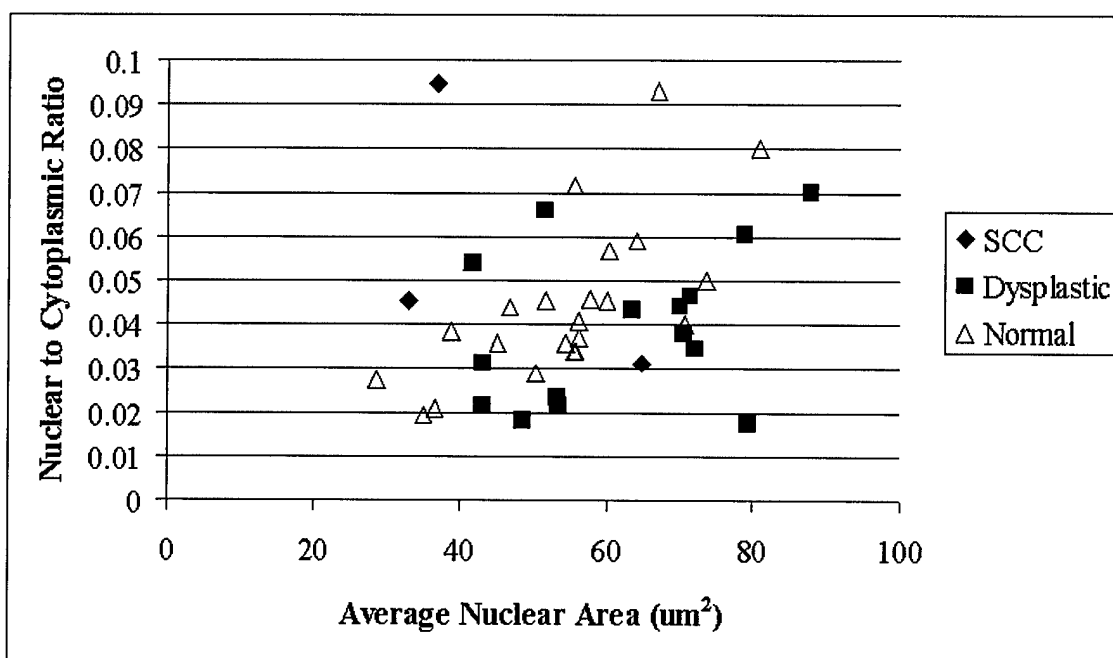


Figure 4.5. Scatter plot of nuclear to cytoplasmic ratio versus average nuclear area for images that are likely from the basal layer (at the maximum depth below the tissue surface at which nuclei are clearly and fully resolvable for a particular depth of focus stack). Images are classified as normal, dysplastic, or from SCCs. At these depths, a slight differentiation between normal and dysplastic images as a function of both nuclear to cytoplasmic ration and average nuclear area can be seen.

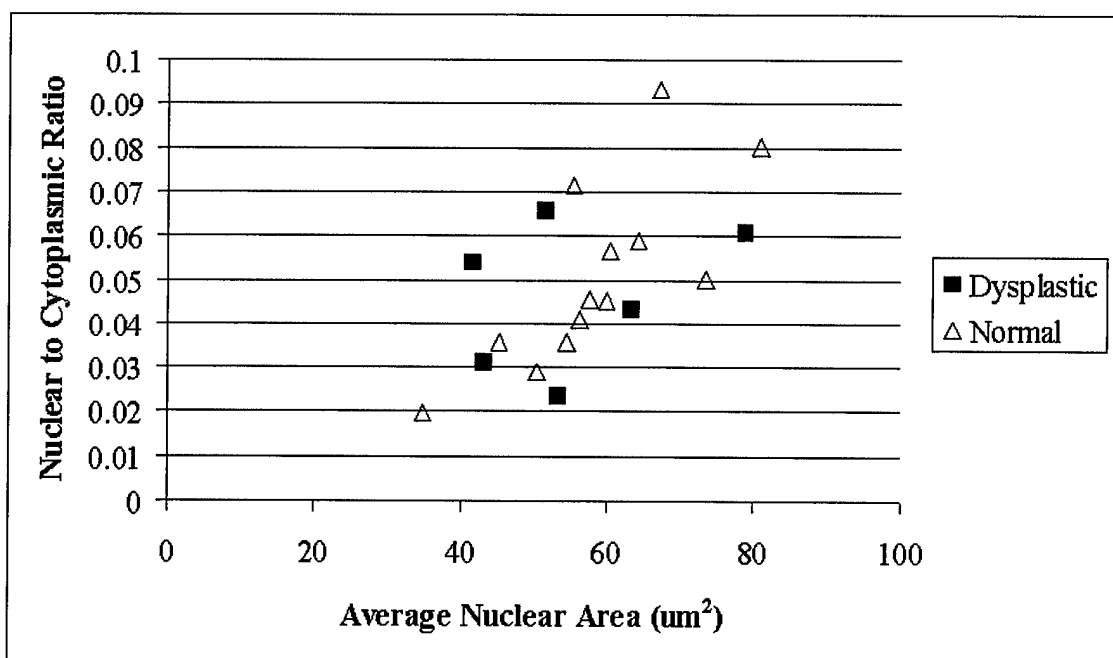


Figure 4.6. Scatter plot of nuclear to cytoplasmic ratio versus average nuclear area for images from the tongue that are likely from the basal layer (at the maximum depth below the tissue surface at which nuclei are clearly and fully resolvable for a particular depth of focus stack). Images are classified as normal, dysplastic, or from SCCs (with no samples in this set). The differentiation between normal and dysplastic samples is still very limited when morphologic variations due to site are removed.

4.3.3 *Image Review*

Figure 4.7 show the results of the image review by 17 pathologists and pathology fellow from the Department of Pathology at the University of Texas M. D. Anderson Cancer Center. This group achieved a mean sensitivity of $73\% \pm 11\%$, with a minimum and maximum value of 56% and 91%, respectively. The group's specificity was much lower with a mean value of $36\% \pm 15\%$ and a minimum and maximum value of 6% and 61%, respectively. Since both values were much lower than achieved with untrained reviewers in the cervix [107], we examined the percentage of reviewers whose diagnosis matched the histopathologic diagnosis for each sample. This analysis showed that more of the trained reviewers correctly diagnosed mild dysplasias and SCCs (78% for both) than for moderate dysplasia (51%). When we examined the diagnostically normal samples (hyperkeratotic and/or hyperplastic), we found that the trained reviewers had difficulty diagnosing severe hyperkeratotic cases, probably due to pleomorphic nuclei often found in hyperkeratotic layers (Figure 4.9A, arrow), and samples from one biopsy with a striated tissue architecture (Figure 4.9C). We also found that the trained reviewers had significant difficulty diagnosing three other biopsies. Examination of the histology for these biopsies found that each biopsy had been cut at an extreme tangential angle that made it difficult for the pathologist to give an accurate diagnosis and also prevented additional sections from being cut from the specimen. When we examined confocal images from these biopsies, we did discover pleomorphic nuclei such as the one in Figure 4.9B (arrow) that led us to believe the tangential cuts for these three cases masked

dysplasia. The mean percentage of reviewers making the correct diagnosis for remaining hyperkeratotic samples remained low though at $45\% \pm 23\%$.

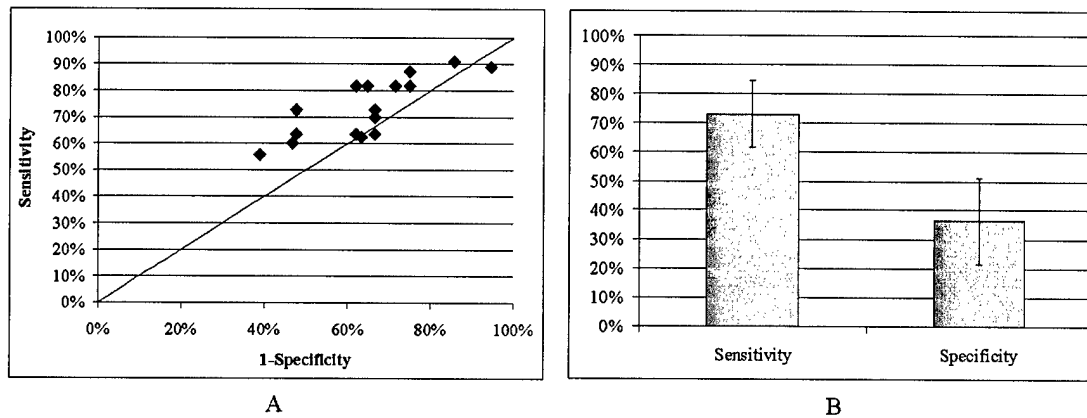


Figure 4.7. (A) Scatter plot of the sensitivity and specificity of the diagnoses made by the trained reviewers. (B) Mean sensitivity and specificity of trained reviewers was $73\% \pm 11\%$ and $36\% \pm 15\%$, respectively.

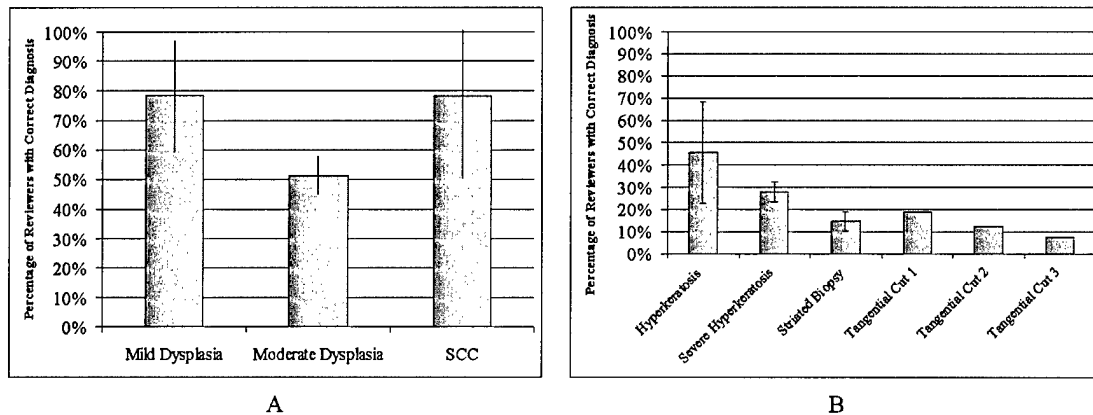


Figure 4.8. (A) A breakdown of the percentage of trained reviewers making the correct diagnosis for abnormal samples identifies that the trained reviewers had difficulty diagnosing moderate dysplasia, but were much better at diagnosing mild dysplasia and SCC. (B) A breakdown of the percentage of trained reviewers making the correct diagnosis for normal samples shows that the trained reviewers made incorrect diagnoses more than 50% of the time but does identify that 1) the trained reviewers had extra difficulty diagnosing severe hyperkeratotic cases and one biopsy with a striated tissue architecture and 2) three histopathologic diagnoses for tangentially cut biopsies may be incorrect.

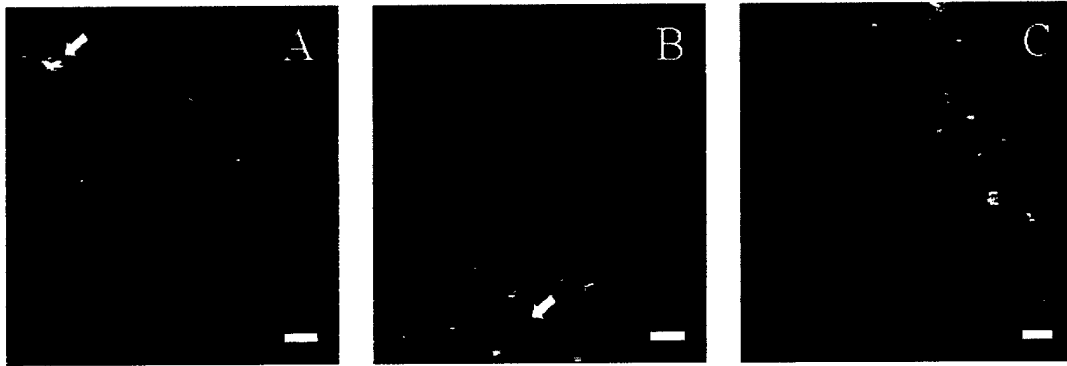


Figure 4.9. Examples of confocal images from diagnostically normal biopsies that trained reviewers consistently classified as abnormal. (A) Confocal image from 90 microns below the surface of a severely hyperkeratotic biopsy from the lateral surface of a tongue with pleomorphic nuclei (arrow). (B) Confocal image from 100 microns below the surface of a tangentially cut buccal mucosa biopsy with pleomorphic nuclei (arrow). (C) Confocal image from 25 microns below the surface of a hyperkeratotic and hyperplastic biopsy from the lateral surface of a tongue with a striated tissue architecture that was repeated at multiple depths.

Figure 4.10 describes the results of the image review by 10 engineering graduate students and one faculty member from the Optical Spectroscopy and Imaging Lab at the University of Texas at Austin. This group achieved a mean sensitivity of $63\% \pm 18\%$, with a minimum and maximum value of 27% and 91%, respectively. The group's specificity was very similar with a mean value of $61\% \pm 15\%$ and a minimum and maximum value of 30% and 81%, respectively. When we examined the percentage of reviewers whose diagnosis matched the histopathologic diagnosis for each sample, we found that the untrained reviewers did not diagnose mild dysplasia and SCC correctly (61% and 70%, respectively) as often as the trained reviewers and also did worse at diagnosing moderate dysplasia (33%). When we examined the samples that were diagnosed as normal (hyperkeratotic and/or hyperplastic), we found that the untrained reviewers diagnosed correctly the severe hyperkeratotic cases as often as mild and moderate hyperkeratosis, but did consistently misdiagnose the biopsy with a striated tissue architecture (27%). Finally, the three tangentially cut biopsies that were consistently misdiagnosed by the trained reviewers were not misdiagnosed by the untrained reviewers as often.

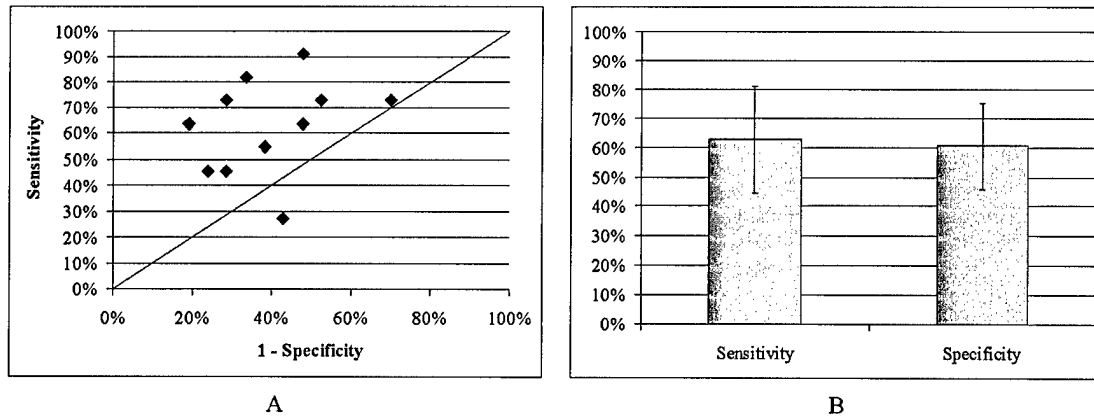


Figure 4.10. (A) Scatter plot of the sensitivity and specificity of the diagnoses made by the untrained reviewers. (B) Mean sensitivity and specificity of untrained reviewers was $63\% \pm 18\%$ and $61\% \pm 15\%$, respectively.

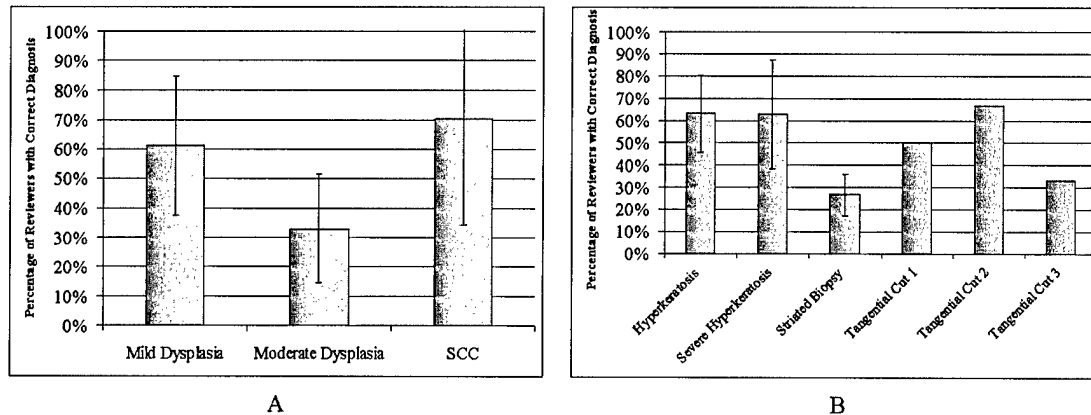


Figure 4.11. (A) A breakdown of the percentage of untrained reviewers making the correct diagnosis for abnormal samples identifies that the untrained reviewers also had difficulty diagnosing moderate dysplasia and that they did not do as well as the trained reviewers in identifying mild dysplasia and SCC. (B) A breakdown of the percentage of untrained reviewers making the correct diagnosis for normal samples shows that they diagnosed severe hyperkeratosis correctly as often as mild to moderate hyperkeratosis, but did misdiagnose the biopsy with striated tissue architecture. More of the diagnoses from the untrained reviewers for the three tangentially cut biopsies matched the histopathologic diagnosis.

4.4 DISCUSSION

The confocal images presented here illustrate the ability of reflectance confocal microscopy to image oral mucosa with resolution comparable to histologic evaluation without tissue preparation and staining. In normal tissue, depth-related changes in cell diameter and nuclear density were observed at multiple anatomic sites within the oral

cavity. We were able to image through the superficial, hyperkeratotic layer into the intermediate and basal layers which most often contain the morphologic changes associated with dysplasia. In SCCs, densely packed, pleomorphic tumor nuclei were visualized with areas of stroma with inflammation once again dark in confocal images of the oral cavity [138].

Our results show that morphologic statistics such as nuclear to cytoplasmic ratio and average nuclear area do allow slight diagnostic differentiation in oral cavity epithelium. Two of the three cases of SCC in the analysis had greater nuclear to cytoplasmic ratios for their average nuclear area than the rest of the sample set while mild and moderate dysplastic epithelium had slightly smaller nuclear to cytoplasmic ratio for their average nuclear area than normal samples. A similar study in the cervix [107] found that the sole use of nuclear to cytoplasmic ratio allowed clear differentiation between normal and low grade dysplasia and high grade dysplasia, but our study shows a more complex relationship between nuclear to cytoplasmic ratio and average nuclear area in the oral cavity. The small number of samples of moderate (four with two having focal moderate dysplasia) and severe (only one focal example) dysplasia in our study also makes the differentiation between dysplasia and normal difficult.

The results of our image reviews emphasize the challenge of detecting dysplasia in the oral cavity. Feedback from our trained reviewers referred to the difficulty in determining where the epithelial stromal layer was in our samples, a key feature required for diagnosing mild dysplasia. We believe that the high number of pathologists who correctly diagnosed mild dysplasia and incorrectly diagnosed hyperkeratotic samples in

our trained image review stemmed from this discomfort, with the pathologists' overdiagnosing to prevent false negative reports. The low number of pathologists correctly diagnosing the cases of severe hyperkeratosis in concert with the indeterminate results of our morphologic analysis at 50 microns below the surface (Figure 4.4) pinpoint the strong possibility of mistaking the irregular, condensed nuclei often found in the hyperkeratotic layer for dysplasia, further emphasizing the need for awareness of where the image plane is in the epithelium. We feel that a more extensive training set must be developed with representative samples of severe hyperkeratosis, mild dysplasia versus basal cells, and squamous cell carcinoma.

The clinical example in Figure 4.3 does illustrate the potential of this technology in the clinical setting. A clinician could use a confocal endoscope to examine the abnormal area and upon seeing the tumor cells (arrow) and stroma with inflammation (double arrows) found in Figure 4.3D, would strongly suspect the presence of SCC and act accordingly. Even more importantly, the clinician could use the confocal endoscope to scan the clinically normal tissue surrounding the abnormal area to help determine the extent of margins needed to extract all of the SCC.

4.5 CONCLUSION

In this study, we have shown the ability of reflectance confocal microscopy to visualize, at the subcellular level, features of both normal and neoplastic oral mucosa throughout the oral cavity. We found that a combination of nuclear to cytoplasmic ratio and average nuclear area allowed slight differentiation between normal and dysplastic

epithelium, but more cases of moderate to severe dysplasia are needed before a definitive answer can be reached. Reviews of confocal images by both trained pathologists and untrained engineers emphasized the need for situational awareness of the region of the epithelium occupied by the image plane and for specific and extensive training in the many variations possible in the oral cavity.

CHAPTER 5

Design, Construction, and Characterization of an Optical Coherence Microscope

5.1 INTRODUCTION

Penetration depth is often a significant limitation in optical imaging, but it is apparent from the last two chapters that the oral cavity has additional features that further retard the ability of a confocal microscope to image deeply into the epithelium. The presence of large amounts of keratin in the superficial part of hyperkeratotic layers increases specular reflection at the tissue surface, reducing the amount of illumination light that actually travels into the tissue. Irregular and condensed nuclei found in the dead cells of this hyperkeratotic layer can mislead attempts at diagnosing dysplasia if imaging does not reach the intermediate and basal layers underneath. In view of these challenges, the OCM with its increased sensitivity and enhanced penetration depth capability seems well suited for imaging in the oral cavity.

This chapter details the design and characterization of an OCM with the subcellular resolution needed to visualize oral mucosa and the morphologic changes associated with dysplasia in this site. System design requirements were derived from the system overall purpose and the target tissue that it would be imaging. A description of the system's design with details of the final configuration of the system is described

before the system's performance is measured in terms of resolution and penetration depth.

5.2 SYSTEM DESIGN REQUIREMENTS

The first step in building any system is gaining an understanding of its requirements. For this instrument, most of its performance requirements were directly related to the anatomy and pathology of the oral cavity while other requirements were derived from these overall performance requirements. The top-level requirements are summarized in Table 5.1 and discussed below.

Resolution and penetration depth requirements came from the structure of both normal and abnormal oral mucosa. In order to detect premalignant lesions, the system had to visualize the morphological changes to tissue, cells, and nuclei that identify neoplasms. The most stringent requirement was that the system be able to resolve individual nuclei, showing their size and shape, which implied a lateral resolution requirement of 2 – 3 microns or better. To prevent blurring, only data from a single layer of cells was desired, implying an axial resolution of at least 6 – 8 microns. In an OCM system, the source and the objective NA were primarily responsible for meeting these parameters. Another requirement determined by cell size was the field of view that had to be covered by each image. With maximum cell diameters of around 25 microns, images needed to be 250 x 250 microns to guarantee capturing 100 cells. In order to see 100 cells, this requirement became 2.5 x 2.5 mm. This requirement helped determine how many pixels were needed for each image to capture the required information.

Description	Requirement
Lateral Resolution:	$\Delta r = 2 - 3$ microns
Axial Resolution:	$\Delta z = 6 - 8$ microns
Field of View:	250 – 2500 microns x 250 – 2500 microns
Penetration Depth:	300 – 500 microns
Safe Irradiance Levels, Fast Image Acquisition Time, Low Cost	

Table 5.1. Top-level system requirements.

Since neoplasms can occur anywhere within the oral mucosa, tissue thickness was the primary driver behind our penetration depth requirement. Meyer recorded average tissue depths of 300 – 500 microns [139], which meant that the system had to be able to penetrate at least 0.5 mm. This requirement was the driving reason behind using an OCM configuration (versus confocal) and levied multiple derived requirements on system components. First of all, if we assumed that noise (instead of background) is the primary limiting factor on penetration depth, the system had to be designed to have enough power and small enough bandwidth to provide a high enough SNR at 0.5 mm for imaging. Also, the objective had to have a suitable working distance (the distance between the objective's front lens and the top of the cover glass (or the sample itself if the objective is not corrected for a cover glass) when the sample is in focus [140]). The objective therefore had to have a working distance long enough to deliver the focus spot to the bottom of the tissue. Finally, the source had to use wavelengths that were not readily absorbed in tissue. This could be done by using a wavelength in the near infrared

(NIR) region of 700 – 1100 nm where losses due to absorption were small compared to those from scattering and could thus be considered negligible [141].

5.3 SYSTEM DESIGN AND FINAL CONFIGURATION

System design and construction of the OCM was split into four areas: 1) the selection of a source and objective to provide high-level satisfaction of resolution and penetration depth requirements; 2) design and construction of the reference arm to allow heterodyne detection and depth scanning; 3) design and construction of the sample arm to fully satisfy resolution requirements; and 4) final integration with control software and data acquisition hardware to direct the system and process images. The following sections will discuss each function in detail, describing design choices made for the OCM shown in Figure 5.1.

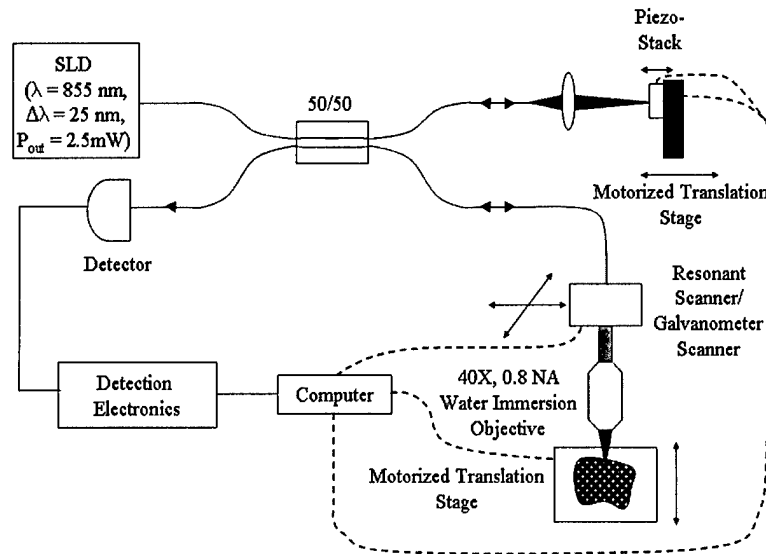


Figure 5.1. OCM block diagram.

5.3.1 *Choosing a source and objective*

The source and objective were the two most important pieces of equipment in the OCM. They were the primary drivers of the resolution and depth penetration achieved by the final instrument and were therefore selected first. A broadband source at an appropriate wavelength and with enough power was chosen to allow penetration of the focus spot into tissue. Based on the source's wavelength, an objective was chosen to provide the desired lateral resolution while minimizing power loss.

The first step was to select a source. An 855 nm SLD with a 25 nm FWHM bandwidth and 2.5 mW of output power (Superlum Diodes, Ltd., SLD 38) was readily available within the laboratory, but a survey of commercially available sources was still performed. Wanting to maximize penetration depth made a source with comparable bandwidth, emission in the NIR region, portable packaging, and more power (to provide increased sensitivity) desirable. The first step in the survey examined technologies other than SLDs for providing broadband NIR light. The top performing OCT systems in terms of resolution and penetration depth use specialized lasers such as a mode-locked Ti:Al₂O₃ laser [92] or a mode-locked Cr⁴⁺:forsterite laser [142], but these systems were too bulky and expensive for clinical applications [91]. Another option was the superfluorescent optical sources developed for telecommunications optical amplification [91], but these sources suffered from non-uniform gain and were also bulky. A more affordable option was to use an edge-emitting LED but these sources could only provide power in the microwatt range [91]. Since none of these technologies met the source requirements for this system, the survey was limited to SLDs.

Alternate SLDs were commercially available, especially if the range of allowable wavelengths was expanded to include the 1300 nm region increasingly used by the telecommunications industry. Moving to this wavelength would increase penetration depth because attenuation due to Rayleigh scattering would decrease [88]. The best candidate at this wavelength was a 1310 nm, 35 – 45 nm bandwidth SLD with 5.5 mW of output power built by B&W Tek, Inc (Model BWC-SLD). This source was not chosen, because, we felt that, at least initially, comparisons with confocal images taken with an 810 nm source were needed to show the improved penetration depth of the OCM and using a source at a similar wavelength would make these comparisons more realistic. An excellent candidate in the 800 nm range was a high power version of the SLD 38 with output power of up to 20 mW. At this point though, a 9 dB increase in sensitivity did not seem worth the investment needed to buy a new source, so the system was built with the available 2.5 mW SLD.

Once the source was selected, an objective was chosen based on the NA needed to provide the specified resolution. The actual lateral resolution was determined by the sample arm's optical design and was therefore very dependent on the chosen scanning system (discussed later in this chapter), but a rough estimate was made at this point. To get a lateral resolution of 2 microns, (2.5) implies that only a NA of 0.18 was required. Since errors within the optics and finite pinholes degrade this resolution and increased lateral resolution was preferred, a high NA objective seemed much better. Other requirements that the objective had to satisfy were having high quality lenses to limit spherical aberrations, a long enough working distance to cover the maximum penetration

depth (> 0.5 mm), high transmission in the NIR region to cut down on power loss in the sample arm, and optimization for water immersion to cut down on the spherical aberrations and specular reflection caused by index mismatch between the objective and sample. With all of these requirements in mind, a 40x, 0.8 NA Olympus water-immersion objective was chosen. The objective was specifically corrected for visible to NIR wavelengths, transmitting 75% at 855 nm, and had a long working distance of 3.3 mm.

5.3.2 *Reference arm design*

Modulation of the reference signal was integral to providing shot noise limited sensitivity. In OCT systems, this modulation is typically produced by moving the reference arm quickly to cause a Doppler shift in the signal. This process can be a significant bottleneck in increasing OCT image acquisition rates, because the arm also has to traverse the entire tissue depth being scanned, requiring a scan range on the order of millimeters [143]. In OCM, this requirement changes because the images are acquired *en face* to the surface of the sample so the reference arm only needs to modulate around the focal plane. In fact, if the amount of movement is kept below the system's axial resolution, image blurring is prevented [144]. The OCM's reference arm therefore needed a method that would provide high frequency, small amplitude path length modulation of its signal.

Many different modulation techniques have been used in OCMs. The original OCM used a PZT stack to provide modulation at 1.64 kHz [59] which was too slow for our purposes. Hoeling used a similar technique in her OCM except her piezoelectric

actuator was driven at a resonant frequency of 122 kHz [144, 145]. Problems with thermal drift of optical path lengths between the reference and sample fibers leading to slow phase drifts in the output were reported with both systems, requiring dual harmonic detection. Another OCM developed in Izatt's lab used a 40 MHz acousto-optic modulator to provide an 80 MHz signal (after double passing), but required very high frequency heterodyne detection and a high power source to achieve desired sensitivities [103]. Another technique wrapped the optical fiber around a piezocylinder, providing modulation by stretching and relaxing the fiber [54]. The primary disadvantages with this technique were the long lengths of fiber needed to get significant changes in path length, polarization changes and stress birefringence problems [145]. Another technique was to coat the fiber with a piezoelectric film that squeezed it, increasing its length [146]. This technique provided modulation from 7 kHz to 6 MHz, but required very high voltages to produce even small movements [145].

Of the techniques described above, the one that provided a relatively fast image acquisition rate without significant investment in money was the 125 kHz piezoelectric actuator used in Hoeling's OCM. Her system formed three-dimensional images of 10^6 volume elements (voxels) in 5 minutes, implying a point scan rate of 3.33 kHz. She used a piezoelectric stack (Thorlabs Inc., AE0203D04), driven at 122 kHz, to vibrate a mirror 400 nm, or nearly one fringe at the OCM's output. This technique did not have problems with the long lengths of cable, high power, and polarization and birefringence effects seen by the others mentioned above. Also with this modulation technique, phase drift in the fibers could be eliminated by setting the modulation amplitude at 0.42λ so that the

sum of powers in the output signal at the first two harmonics of the modulation frequency was insensitive to the drift [145]. We originally planned to use the same modulation frequency and amplitude used by Hoeling, but a factor in the confocal arm design (described in the next section) forced us to move the modulation frequency to a much higher resonant frequency at 376.65 kHz. At this higher frequency, the displacement of the mounted piezo per volt was too low to balance the two harmonics without damage to the piezo because of the decrease in piezo impedance associated with the higher frequency and relaxation characteristics of the piezo itself. We found that driving the piezo at amplitudes greater than 7.5 V_{p-p} provided only minimal increase in displacement so we selected this modulation amplitude to minimize the risk of burning out the piezo during imaging, providing a peak-to-peak displacement of 315nm and 65% reduction in phase variations.

Other than modulation, the only other function that the reference arm had to perform was scan depth matching. The coherence gate provided by the source meant that if path lengths between the sample and reference arm were mismatched by more than 13 microns, an interference signal would not occur. Also, the OCM had to adjust both the sample and reference arms in order to image at different depths because of the use of high NA objectives. To complicate matters, the sample arm's focus would be in tissue while the reference arm's light would be totally in air, making the optical paths to a specific depth different. Therefore, each time the sample arm's focus moved, the reference arm had to be adjusted so that:

$$(n_{air})^2 z_{ref} \cong (n_{tissue})^2 z_{sample} \quad (5.1)$$

(within the coherence gate). This meant that depth translation had to be performed in concert and with high precision and accuracy. While manual micrometers could work in a laboratory situation, the length of time needed to adjust for each new image would be prohibitive for use in the clinic. As a result, both arms included motorized translation stages (Newport, Inc., ILS Series) with on-axis accuracy of 5 μm over 100 mm and an interface to control them through a computer. Also, an algorithm was needed to synchronize the pathlengths. Schmitt solved this problem by assuming that $n_{\text{air}} = 1$ and $n_{\text{tissue}} = 1.4$ and automatically moving the reference arm twice as far as the sample arm [102]. We originally thought that this technique would not be sufficient for imaging tissue because of variability in index of refraction due to tissue differences and depth, but found that this simple algorithm gave a good match in pathlengths until the focal plane reached greater than 250 microns below the tissue surface at which point, minor adjustments to a manual micrometer included in the reference arm corrected misalignments. We therefore included a setting in the control software that allowed user choice of air or tissue as the sample which then caused the reference arm to be moved either an equal distance or twice as far as the sample arm.

5.3.3 *Sample arm design*

The sample arm was designed to perform three functions: 1) provide the needed lateral resolution; 2) scan the focus point in the x-y direction to form an image; and 3) change the scan depth in concert with the reference arm. Changing the scan depth was discussed in the paragraph above, so this section will concentrate on the optical design needed to build individual images. The first step was to choose a scanning system with

the necessary small-scale resolution needed to support our lateral resolution requirement and the ability to scan at the rates needed for our desired image acquisition rate. Then, the optics needed to illuminate the spot on the focal plane and return the reflected signal to the detector had to be designed to fit our lateral resolution requirement for a multiple lens system with a finite-sized, optical fiber based confocal pinhole.

The primary function of the sample arm in an OCM is to scan a focused laser spot through the sample in a defined pattern that provides adequate coverage to satisfy both resolution and field of view requirements. A scanning system was therefore needed to deflect the laser beam through a range of angles in a plane perpendicular to the optical axis. There are two general techniques for performing this deflection. The beam can be moved by diffraction with an acousto-optic cell, but this option is not used often due to the complicated optics required [147]. The other method uses mirrors rotated through a range of angles to deflect the beam. For two-dimensional imaging, two mirrors are needed to implement raster scanning, where one mirror rotates quickly through a complete line scan in the time needed for the slower mirror to move to the next line. The system used to drive these mirrors is directly tied to the image acquisition rate and the speed needed for each scan.

Faster image acquisition rates in imaging systems are always more desirable since they allow the user to view more of the sample quickly without causing blurring in the image. We therefore calculated the fastest imaging speed allowable within the constraints of the modulation technique employed by the reference arm. Using Nyquist's criterion in concert with the width of individual fringes in the interferometric signal, we

estimated that a three second image acquisition rate would allow modulation at 122 kHz and 2 microns lateral resolution over a 256 microns x 256 microns field of view. This image acquisition rate required the slow mirror to scan at 0.33 Hz while the faster arm scanned at 85 Hz. After a survey of the available scanning systems, we choose an integrated raster-scanning system provided by the Electro-Optical Products Corporation that locked a low cost resonant optical scanner with a galvanometer in a master/slave mode and provided the actuators, mirrors, and control box in a single package.

Once the scanning system was chosen, the optics needed to deliver light from the optical fiber to the objective and back had to be designed. For the scanning system to work properly, the optics 1) had to image the sample focus spot onto the fiber; 2) image the objective aperture onto the scan mirrors; 3) control the beamwidth to prevent vignetting (with associated power loss) by lenses and mirrors in the optical path while completely filling the back focal plane of the objective; and 4) meet the lateral resolution requirement while minimizing power losses from specular reflection off optical component surfaces. The easiest way to do this is with two Keplerian telescopes (two lenses separated by the sum of their focal lengths) between each scan mirror, so the mirrors always deflect collimated light. This technique places the image planes at the focal points of each lens and allows simple alignment of the scan mirrors. The scan mirrors and the objective's back aperture must be placed in conjugate "zero-deflection" planes so that the back aperture will always be fully illuminated and a change in mirror angle translates to linear motion of the sample spot [148]. This is easily performed in the arrangement shown in Figure 5.2 by placing the optics such that:

$$s_o + s_i = f_a + f_b \quad (5.2)$$

where f_a and f_b are focal lengths and s_o and s_i are object and image distances to the lenses. An additional mirror was also added to the system to deflect the light down onto the z-axis for easier placement of samples. Individual lenses were selected so that their focal lengths supported the field of view requirement, their diameters could focus the beam during scanning, and their anti-reflection coatings limited power losses within the sample arm.

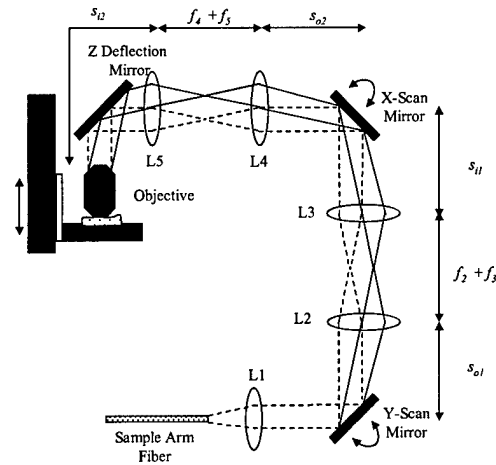


Figure 5.2. Sample arm optics.

After construction of the sample arm, we discovered that we had forgotten to incorporate the image bandwidth into our calculations for determining our image acquisition rate. The deflection angle of the fast scan mirror required to move the focus through 250 microns in the sample combined with an 85 Hz scan rate resulted in an image bandwidth of over 125 kHz. Dual harmonic detection requires that the modulation frequency be greater than twice the image bandwidth to prevent overlapping of the harmonics (since the image bandwidth appears on both sides of the carrier) [101]. At this

point, we moved our modulation frequency from 122 kHz to 376.65 kHz to incorporate this image bandwidth.

The final sample arm configuration acquired images of 230 pixels by 230 pixels and a field of view adjustable from 150 – 250 microns by controlling the deflection of the scan mirrors.

5.3.4 Computer and electrical design

The final step in building the OCM was to design the detection electronics required to demodulate the signal from the detector as well as perform an electrical interfacing design between the computer and the rest of the system. These interfaces are shown in Figure 5.3. A 125MHz, low noise photoreceiver (New Focus, 1801-FC) transduced the interferometric signal from the coupler into a voltage signal and sent the signal to detection electronics. The detection electronics for the OCM included a preamplifier (Hewlett-Packard, 8447D) to give 26 dB of amplification to the signal from the detector, a variable filter (Krohn-Hite, 3202) to bandpass filter the signal down to the two harmonics and reduce noise, and a RMS detector (Analog, AD8361) to demodulate the signal and provide an estimate of the signal intensity, or square of the fringe amplitude. A complementary estimate of signal intensity was provided by blocking the reference and measuring the intensity of the backscattered light returned from the confocal microscope. This confocal signal returned to the computer through a separate electrical path which amplified the signal by 10 dB and highpass filtered it to reduce noise.

The computer had to interface with two instruments while receiving data from the detection electronics. The scanning system had a controller box which drove the mirrors and provided control signals to help synchronize data acquisition. Both of these signals were fairly simple and could be used to configure triggers on a National Instruments (NI) Multifunction DAQ board (PCI-MIO-16E-4) to acquire the data signal with a 250kS/s sampling rate during the linear portion of a line scan. The other interface was to the motorized translation stage controller. This instrument was GPIB-compatible so a NI PCI-GPIB board was used to control it.

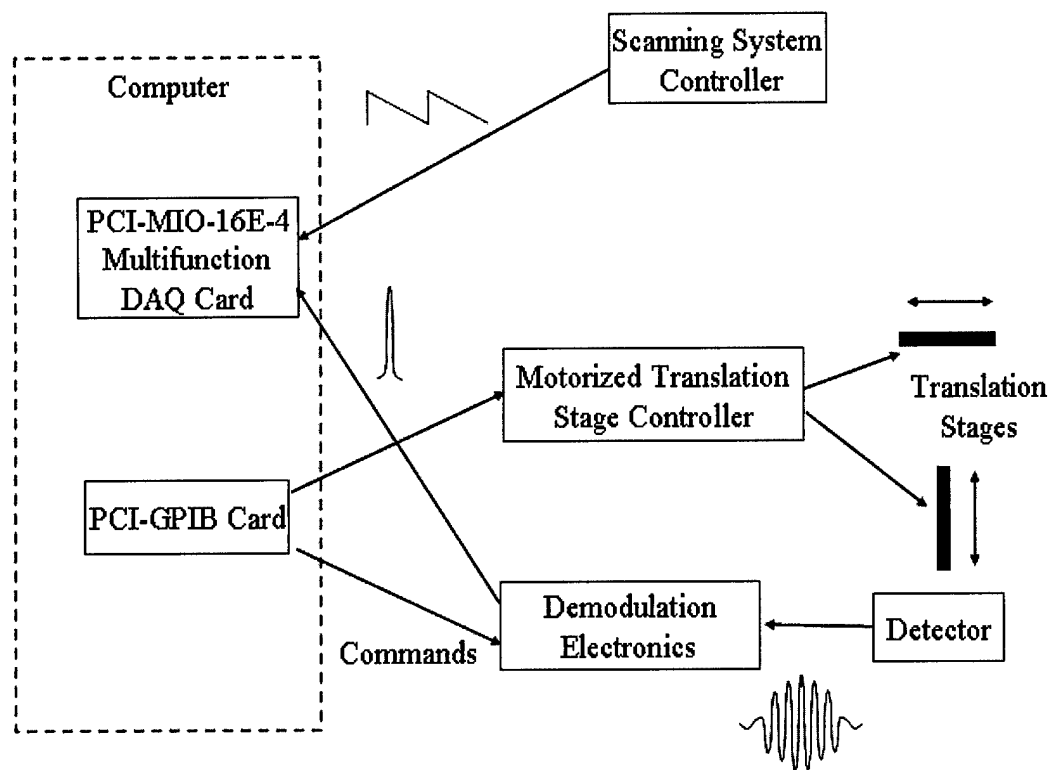


Figure 5.3. Electrical interfacing requirements.

5.4 OCM CHARACTERIZATION

5.4.1 Resolution

The OCM's resolution was estimated by determining the fiber optic's effect on ideal performance through calculation of Gu's dimensionless fiber spot size parameter, A (2.8) [70]. Wave Optics provided single mode fiber for 855 nm with a core radius of 2.5 microns and NA of 0.118, implying a V of 2.166 and r_o of 2 microns. Since the objective's back aperture had a radius of 3.6 mm, the collimating lens had to have a focal length greater than 30.29 mm to overfill it. Using a commercially available focal length of 31.7 mm resulted in a normalized parameter A of 2.81. The computed PSF for this A is shown in Figure 5.4, giving a $u_{1/2}$ of 3.48 optical units (See Section 2.5.1 for details on optical units). This implies that the confocal microscope in the sample arm will give an axial resolution of 1.18 microns.

Calculating the system's lateral resolution is more complicated. A point spread function for lateral intensity using a fiber optic pinhole is not available. As an estimate of its effect, a normalized pinhole radius was determined by finding the radius that gives the same $u_{1/2}$ of 3.48 optical units, using graphs of $u_{1/2}$ as a function of v_p from [68]. The corresponding v_p of 3.8 optical units predicts that the system will have a lateral resolution of 1.6 optical units, or 544 nm. Since the system only uses 230 pixels per line, the lateral resolution of the OCM will be limited by sampling. With a field of view adjustable from 170 – 250 microns, ideal lateral resolution could vary from 1.5 – 2.2 microns.

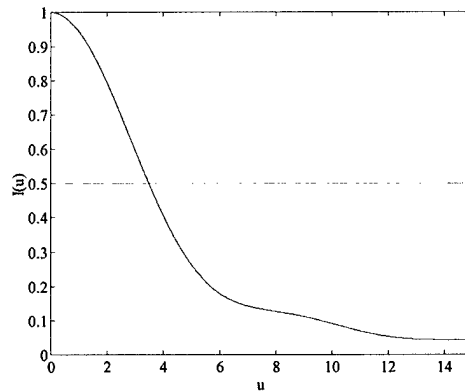


Figure 5.4. Intensity as a function of u and a normalized parameter, $A = 2.81$.

Actual resolutions for the OCM were measured using a Ronchi grating and a first surface mirror. A line profile from a grating image is shown in Figure 5.5A. With a field of view of 170 microns, a lateral resolution of 2.3 microns was determined by measuring the distance between the 10% and 90% intensity lines. The normalized intensity response for both the confocal mode and the OCM to moving a mirror through the focus while keeping the reference arm's pathlength matched with the top of the mirror is shown in Figure 5.5. Axial resolutions of 5.4 microns and 7.8 microns for the confocal mode and the OCM, respectively, were measured through the full-width half-maximum of the average intensity. We attribute the slight widening in the OCM's axial response in comparison to the confocal arm to dispersion effects and the overall broadening of both resolutions in comparison to estimates to spherical aberrations in the optics. The measured resolutions still meet our system requirements of 2 – 3 microns and 6 – 8 microns for lateral and axial resolution, respectively.

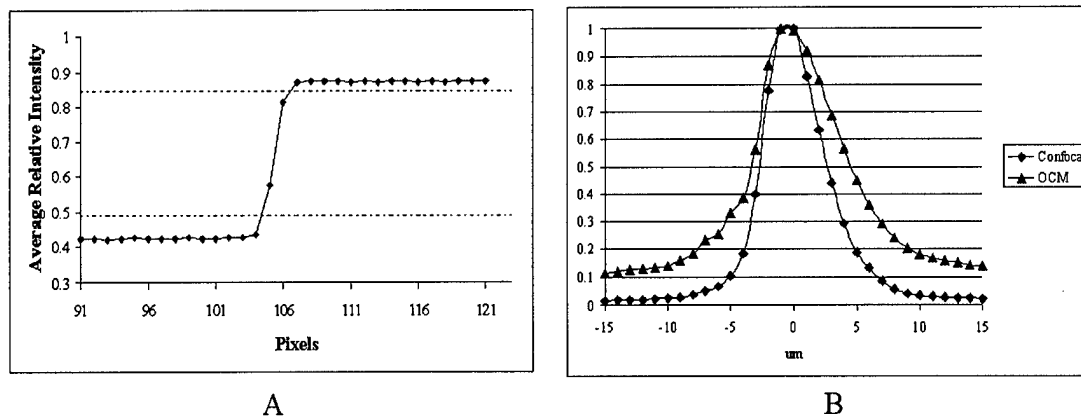


Figure 5.5. Measured resolution for the OCM. (A) A line profile from an image of a Ronchi grating showing the system's edge response. A lateral resolution of 2.3 microns was determined by measuring the distance between the 10% and 90% intensity lines. (B) Normalized intensity response to moving a mirror through the focus while keeping the reference arm's pathlength matched with the top of the mirror. Axial resolutions of 5.4 microns and 7.8 microns for the confocal mode and the OCM, respectively, were measured through the full-width half-maximum of the average intensity. The slight widening of axial resolution for the OCM system is attributed to dispersion effects.

5.4.2 Penetration Depth Estimate

The system's estimated signal-to-noise performance can also be calculated by measuring the amount of power returned to the detector by mirror (assumed to be a perfect reflector) and solving (2.12) for the shot-noise-limited SNR. When a mirror was placed at the focal point of the sample arm's objective, a Newport Model 1830-C optical power meter measured 0.17 mW of power emerging from the fiber after the 50/50 coupler that is coupled to the detector. With a *NEB* equal to 575 kHz (the bandwidth of

the bandpass filter used to isolate the two harmonics) and detector efficiency of 0.64, an estimated SNR of 90 dB should be achieved. The actual noise in the OCM was measured by focusing the sample illumination onto a mirror and acquiring 50 OCM image frames with the coherence gate moved completely out of alignment with the sample arm pathlength and the sample arm blocked. The variance of each pixel was calculated over the 50 frames and the average variance for the image of $4.84 \times 10^{-9} \text{ V}^2$ was used as an estimate of noise. The maximum signal generated divided by this estimate gave a SNR of 88 dB.

Gaining understanding of how noise will limit penetration depth requires a more realistic estimate of epithelial signal as it is attenuated by losses in tissue. An estimate of the signal as it travels deeply into tissue can be calculated using the equation,

$$I(z) = I_o e^{-OD} R(z) e^{-OD} = I_o R(z) e^{-2OD} \quad (5.3)$$

where I_o is the incident intensity, $R(z)$ is the depth dependent reflectivity, and OD is the optical depth, which is the product of the attenuation coefficient times depth. Solving this equation for the depth at which the signal is only twice the noise floor provides a penetration depth estimate of 8.1 OD. Estimates of scattering coefficients in dysplastic cervical epithelium ranges from 66 cm^{-1} to 117 cm^{-1} [77] which implies that noise-limited penetration depths should be within the range of 690 – 1227 microns which exceeds our requirement of 300 – 500 microns. This estimate does not include the effect of multiple scattering and background on our ability to resolve features deeply within the epithelium.

CHAPTER 6

Detection and Diagnosis of Oral Neoplasia with an Optical Coherence Microscope

6.1 INTRODUCTION

Optical coherence microscopy (OCM) is a new optical imaging technology that can provide detailed images of tissue architecture and cellular morphology of living tissue. The technique combines the sub-cellular resolution of high numerical aperture (NA) confocal microscopy with the increased sensitivity and penetration depths of optical coherence tomography (OCT) to acquire detail similar to that available in histologic tissue evaluation, except that images are achieved non-invasively and without stains. In biological structures, resolution of 2 microns [71] has been achieved with a 200 – 500 micron field of view and penetration depth of 600 microns in plant specimens [58, 104] and *in vitro* human colon tissue [59]. Thus, OCM provides the potential to image oral epithelium in a clinical setting with the subcellular resolution needed to assess the pathologic state of tissue.

OCM imaging builds detailed images of cell morphology and tissue architecture by using a high numerical aperture (NA) confocal microscope to collect light backscattered by various tissue components to provide contrast. The high NA objective focuses light to a three-dimensional voxel within the tissue and a pinhole placed at a

conjugate image plane within the confocal microscope is used to localize reflected light from the focal volume. Interferometric techniques are then used on the light returning through the pinhole to further isolate photons returning from a given voxel and reject multiply scattered photons that retard the penetration depth of confocal microscopes in opaque samples [71, 76]. Changes in refractive index provide the contrast necessary to recognize intracellular detail. At this time, OCM imaging has been limited to relatively few biological tissues, but results from confocal microscopy and OCT support the potential of this optical modality for imaging oral lesions.

Both confocal microscopy and OCT have had success in visualizing pre-cancerous and cancerous conditions. High NA confocal microscopy with its subcellular resolution enables imaging of cell morphologic and tissue architectural changes associated with dysplasia and cancer. In skin, where cytoplasmic melanin provides a strong source of backscattering, confocal microscopes have captured morphologic changes in cytologic structure and visualized microvasculature in both basal cell carcinomas and melanomas [119-121, 149]. In amelanotic epithelial tissues, where cell nuclei provide the primary source of reflected light, recent work showed that reflectance confocal imaging of normal and precancerous cervical tissue can characterize nuclear size, nuclear density and nuclear to cytoplasmic ratio without the need for tissue sectioning or staining. Parameters extracted from confocal images could be used to discriminate high grade cervical precancers with a sensitivity of 100% and a specificity of 91% in a study of 25 samples [107]. In a study of the esophagus [122], nuclear to cytoplasmic ratios were extracted from confocal images of normal esophagus and

esophageal cancer; differences were statistically significant and could be used to identify cancer with a diagnostic accuracy of 90%. Confocal imaging of oral mucosa has resolved subcellular detail at depths of 250 microns and 500 microns in the lip and tongue, respectively [44], and captured many features of normal mucosa and oral squamous cell carcinoma from multiple sites within the oral cavity [138].

While high resolution OCT imaging has demonstrated resolution on the order of 1 micron [150], current clinically tested OCT systems do not provide images with the subcellular resolution characteristic of high NA reflectance confocal microscopy. They are able to use their deeper penetration depth capability of up to 1 mm to resolve architectural differences associated with the epithelial and stromal layers as precancers and cancers develop. In a study of the cervix, an OCT system captured irregularities in the epithelial layer and basement membranes of carcinoma in situ as well as lack of definition in the basement membrane associated with invasive carcinoma [151]. OCT endoscopes have also successfully imaged a large number of internal sites. These systems demonstrated a reduction in the distinction between epithelial and stromal layers in OCT images of precancerous and cancerous tissues of the larynx, esophagus, uterine cervix, colon, urinary bladder and esophagus [152-158] when compared to normal tissue.

The goal of this study was to characterize the features of normal and neoplastic oral mucosa using OCM. We report results of a pilot study using an OCM system to image pairs of clinically normal and abnormal biopsies obtained from 12 patients. We find that OCM can image oral mucosa with resolution comparable to histology without the need for tissue fixation, sectioning or staining. Analysis of epithelial scattering

coefficients clearly discerns a difference between the hyperkeratotic layers and the non-keratinized epithelium below and an increase in scattering associated with premalignancy.

6.2 METHODS AND MATERIALS

6.2.1 Specimens

Oral cavity biopsies were acquired from 12 patients at the Head and Neck Clinic of the University of Texas M. D. Anderson Cancer Center who were undergoing surgery for squamous cell carcinoma (SCC) within the oral cavity. Informed consent was given by all patients, and the project was reviewed and approved by the University of Texas M. D. Anderson Cancer Center Office of Protocol Research and the Institutional Review Board at the University of Texas at Austin. Biopsies (approximately 3 mm wide by 4 mm long by 2 mm thick) were acquired from at least one clinically normal appearing and clinically suspicious area and immediately placed in growth medium (DMEM, no phenol red). Both optical coherence and reflectance confocal images were obtained at multiple image plane depths from the biopsies within twelve hours of excision. Following imaging, biopsies were fixed in 10% formalin and submitted for routine histologic examination by an experienced head and neck pathologist. Additional sections from four of the biopsies were stained with Monoclonal Mouse anti-Cytokeratin (Pan) (MMAC) Concentrate Antibody (Zymed Laboratories, Inc.), a broad spectrum monoclonal antibody cocktail of clones A1 and A3 which reacts to cytokeratins 10, 14/15, 16 and 19

in the acidic subfamily and all members of the basic subfamily, to assess correlations between confocal image features and the presence of keratin in the specimen.

6.2.2 *Optical Coherence System*

Images were obtained from each biopsy using an OCM system (Figure 6.1). Illumination was provided by a broadband superluminescent diode (Superlum Diodes, Ltd., SLD 38) operating at 850 nm with a 25 nm full-width half maximum (FWHM) bandwidth and delivered to the confocal microscope through a 50/50 coupler and a single-mode optical fiber. The illumination light was collimated to a beam diameter of 8 mm upon exciting the optical fiber and delivered to a water immersion microscope objective (40X, 0.8 NA) via a raster-scanning system. This scanning system used a resonant scanner providing an 85 Hz line scan rate and a slow scan galvanometer to move the focused light in the sample, allowing acquisition of images in 3 seconds. The objective focused light to a 1 micron-diameter spot with an average illumination power of 0.4 mW. Light backscattered from the tissue was recoupled into the optical fiber, mixed in the 50/50 coupler with light returning from a reference arm and sent to a low-noise, broadband detector (New Focus, 1801-FC).

If the pathlengths of light returning from the sample and reference arm matched to within a coherence length of the SLD, interference fringes were produced at the detector. The pathlength of the reference light was small-amplitude (<1 micron) modulated using a technique described in [144, 145] where light was reflected from a mirror mounted on a sinusoidally driven piezo (NEC, AE0203D04). Demodulation of the first two harmonics of this modulated signal allowed reduction and even elimination of variation in the signal

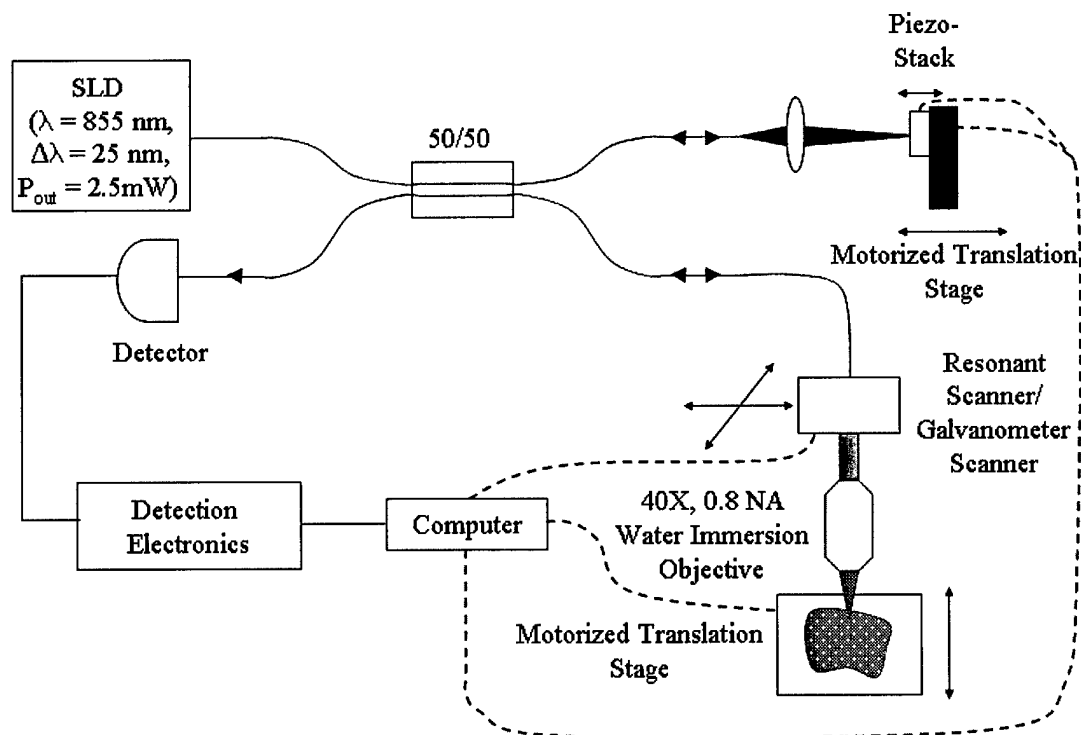


Figure 6.1. Diagram of the OCM system used to image oral cavity specimens.

caused by thermal drifts in the pathlengths of the reference and sample optical fibers [59]. Hoeling demonstrated that the thermal variation could be eliminated if a modulation frequency of 122 kHz was used [144], but in order to raise our image acquisition rate, we increased our modulation frequency to a resonant frequency at 376.65 kHz. At this higher frequency, the displacement of the mounted piezo per volt was too low to balance the two harmonics without damage to the piezo, but a driving signal of 7.5 V_{p-p} was used to provide a peak-to-peak displacement of 315 nm and 65% reduction in phase variations. The resulting signal was amplified by 26 dB and bandpass filtered to isolate the two harmonics and reduce noise. A RMS detector (Analog, AD8361) demodulated the signal

and provided an estimate of signal intensity, or the square of the fringe amplitude. A complementary estimate of signal intensity was acquired by blocking the reference arm illumination and measuring the intensity of the backscattered light returned from the confocal microscope. This confocal signal returned to the computer through a separate electrical path which bandpass filtered the signal to 250 kHz and provided 10 dB of amplification.

The OCM system operated at a dimensionless fiber spot size, A , [70] of 2.81 to optimize optical sectioning. The measured lateral and axial resolution of the system were 2.3 microns and 7.8 microns, respectively. The field of view was adjustable from 150 – 250 microns by controlling the deflection of the scan mirrors.

6.2.3 *Imaging and Image Processing*

Prior to imaging, the biopsies were removed from growth media, rinsed with phosphate buffered solution (PBS), and oriented so the image plane of the microscope was parallel to the epithelial surface and would approach the epithelial layer first. A 6% solution of acetic acid was then added to each sample to increase image contrast [123]. OCM and confocal image pairs were acquired at various epithelial depths until tissue details were no longer resolvable by either of the imaging modalities. Upon acquisition, image voltage data was saved to a file as floating point numbers and also translated into 8-bit, grayscale format using a full-scale contrast stretch algorithm to produce individual images. Each of the image frames presented here were given additional post-processing to increase image quality. Brightness was enhanced by adding a selected percentage of

full gray scale to each pixel and contrast increased by removing another percentage of full gray scale from the image and expanding the remaining midrange gray levels.

Images of stained histologic sections were acquired using a color CCD camera coupled to a brightfield microscope. The OCM's small field of view made it extremely difficult to register exactly where in the biopsy images were acquired so we identified areas in histologic sections that corresponded to features present in our images.

6.2.4 *Scattering Coefficient Analysis*

A selection of image depth of focus stacks were also processed to estimate the epithelial tissue scattering coefficient using a technique described in [77]. An estimate of the aggregate tissue scattering coefficient can be calculated using the equation,

$$I(z) = I_0 e^{-\mu_t z} R(z) e^{-\mu_t z} = I_0 e^{-2\mu_t z} R(z) \quad (6.1)$$

where I_0 is the incident intensity, $R(z)$ is the depth dependent reflectivity, and μ_t is the attenuation coefficient, which is the sum of the absorption and scattering coefficients. This technique assumes that excitation and reflected light travels parallel to the optical axis and that the attenuation coefficient does not vary as a function of depth. In the near infrared, where we made our measurements, the absorption coefficient is significantly lower than the scattering coefficient [159] so the attenuation coefficient was assumed to equal the scattering coefficient. Binary masks outlining nuclei were hand-segmented by one person using a graphics editing program (JASC, Paintshop). A mean reflected intensity for these nuclei was calculated using the nuclear masks to extract specific voltage levels from the detector values saved during imaging and plotted as a function of

depth for each stack. These data were fit to (6.1) by minimizing the mean square error between the data and the fit with the scattering coefficient as the only variable parameter.

6.3 RESULTS

6.3.1 Imaging Results

Both OCM and confocal images were successfully obtained from 28 biopsies acquired from 12 patients with resolution similar to that provided by bright-field microscopy typically used to examine histologic sections. Table 6.1 shows the number of clinically normal and abnormal specimens obtained from each site within the oral cavity. Table 6.2 lists the histopathologic diagnoses for each biopsy from each patient with 20 showing hyperkeratosis, 14 exhibiting hyperplasia, four with mild dysplasia (two focal), three with moderate dysplasia (one focal), one with focal severe dysplasia, one moderately differentiated SCC, one well differentiated SCC, and three specimens having no diagnosis due to a lack of epithelium in the histologic section.

Table 6.1. Number of clinically normal and abnormal biopsies from each site.

Location	Clinical Appearance	
	Normal	Abnormal
Tongue (Lateral and Ventral Surfaces)	3	4
Floor of Mouth	2	2
Gingiva	4	6
Buccal Mucosa	3	2
Soft Palate	1	1

Table 6.2. Histopathologic diagnosis by patient.

#	Site	Histopathologic Diagnosis	
		Clinically Normal Biopsy	Clinically Abnormal Biopsy
1	Tongue (Lat. surface)	Hyperkeratosis, hyperplasia	Moderate focal dysplasia
2	Gingiva	Hyperkeratosis, hyperplasia	Hyperkeratosis, hyperplasia
3	Gingiva	Mild focal dysplasia	Moderate to severe focal dysplasia, hyperkeratosis
4a	Gingiva	None ¹	Hyperkeratosis, hyperplasia
4b	Soft Palate	Hyperkeratosis, hyperplasia	Well differentiated SCC
5	Floor of mouth (N) Gingiva (A)	Hyperkeratosis, hyperplasia	None ¹
6	Tongue (Lat. surface)	Hyperkeratosis, hyperplasia	Mild focal dysplasia, hyperkeratosis
7	Floor of mouth	Mild dysplasia, hyperkeratosis	Mild to moderate dysplasia, severe hyperkeratosis
8	Tongue (Lat. surface)	Severe hyperkeratosis, hyperplasia	Mild dysplasia
9	Buccal mucosa (N, A1, A2)	Hyperkeratosis, hyperplasia	Severe hyperkeratosis (A1) Hyperkeratosis, hyperplasia (A2)
10	Buccal mucosa (N) Floor of mouth (A1) Gingiva (A2)	Hyperkeratosis, hyperplasia	Moderate dysplasia, hyperkeratosis (A1) Hyperkeratosis, hyperplasia, (A2)
11	Gingiva	Hyperkeratosis, hyperplasia	Moderately differentiated SCC
12	Buccal mucosa (N) Tongue (Lat. surface) (A)	Hyperkeratosis, hyperplasia	None ¹

¹No epithelium in specimen.

OCM images were acquired by scanning focused light in a plane parallel to the epithelial surface. Figure 6.2F shows a histology image from a biopsy with hyperkeratosis and hyperplasia from the floor of the mouth, flanked by confocal (Figure 6.2A – E) and OCM (Figure 6.2G – K) images taken from the same biopsy at the different depths indicated by the lines on Figure 6.2F. Images from the superficial epithelium (Figure 6.2A, B, G, and H) taken at 50 and 150 microns beneath the epithelial surface show larger cells with extensive keratin providing bright return from the cell periphery regions while those acquired from 250 microns below the tissue surface (Figure 6.2C and I) capture the more uniform, smaller cells associated with the intermediate layer. The images from the basal epithelium at 300 microns below the tissue surface (Figure 6.2D and J) visualize a distinct increase in cell density and nuclear to cytoplasmic ratio, but contrast in the confocal image (Figure 6.2D) is now significantly reduced. At this depth, the OCM is still able to resolve cell membranes (arrow) (Figure 6.2J) and at 350 microns below the tissue surface (Figure 6.2K), basal cells are still visible in one portion of the image (arrow) while areas of low return represent where part of the image plane has traversed the basement membrane into stroma (double arrows). Confocal and OCM image features compare well with the corresponding transverse histologic section (Figure 6.2F). This pattern of confocal and OCM images was typical of those recorded from normal biopsies in this study.

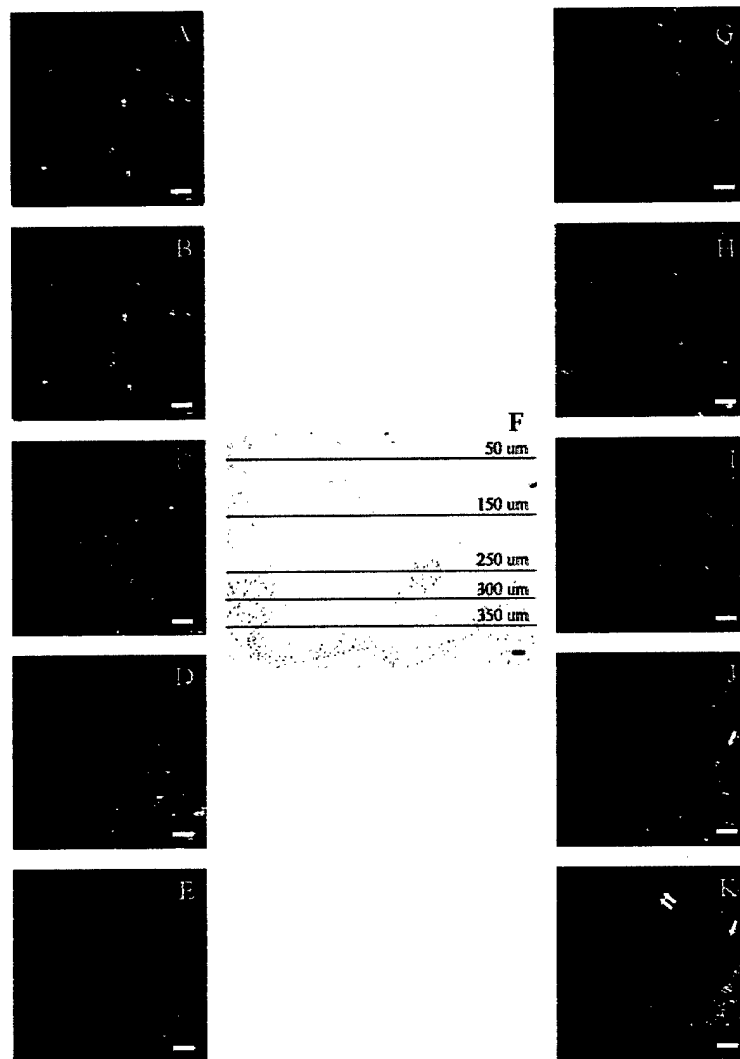


Figure 6.2. Transverse histologic image (F) with en face confocal (A – E) and OCM (G – K) images obtained at different depths beneath the epithelial surface of a hyperkeratotic and hyperplastic floor of the mouth biopsy. Both imaging modalities captured an increase in nuclear density as the depth of the focal plane increased from (A, G) 50 microns to (B, H) 150 microns to (C, I) 250 microns below the tissue surface. At (D) 300 microns below the tissue surface, confocal image quality started to degrade and by (E) 350 microns below the tissue surface, features were barely resolvable. In the corresponding OCM images, cell membranes (arrow) are still resolvable at (J) 300 microns below the tissue surface. At (K) 350 microns below the tissue surface, cells are captured (arrow) and part of the focal plane has traversed through the basement membrane into stroma (double arrows). Scale bars = 20 microns.

Detection of oral dysplasia requires sub-cellular resolution to capture changes in nuclear shape and area characteristic of pathologic changes in tissue during pre-malignant progression. Figure 6.3 shows both histologic and OCM images from a hyperplastic and hyperkeratotic biopsy from gingiva (A, C) and an invasive, well differentiated squamous cell carcinoma from the soft palate (B, D). The nuclei in Figure 6.3A and Figure 6.3C demonstrate the consistent shape, area, and spacing common to healthy tissue. In sharp contrast, the tightly packed tumor cells imaged in Figure 6.3B and Figure 6.3D exhibit extensive variations in nuclear size and nuclear morphology. Epithelial nuclei (single arrows) appear as bright areas on the OCM image, whereas areas of stroma with inflammation (double arrows) appear dark in the OCM image.

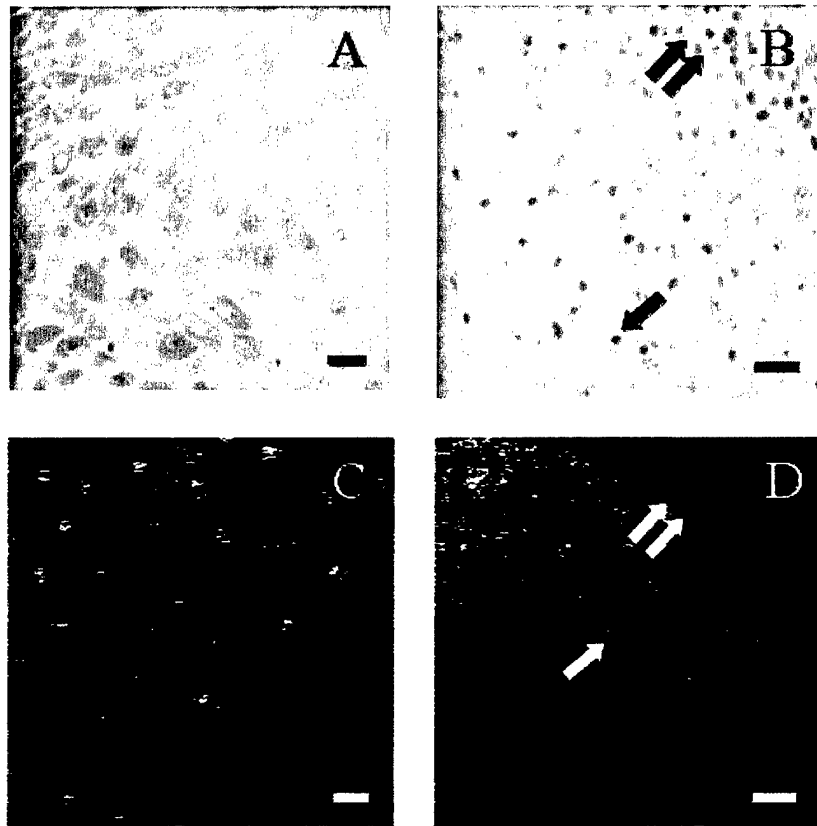


Figure 6.3. Histologic and en face OCM images of normal and cancerous tissue. The consistent nuclear area and spacing in images from a hyperplastic and hyperkeratotic biopsy from gingiva (A, C) contrast sharply with the tightly packed tumor cells (arrow) containing irregular nuclei visualized in a well differentiated SCC from the soft palate (B, D). A portion of stroma with inflammation (double arrows) is also captured in both images of the SCC (B, D). Scale bars = 20 microns.

6.3.2 *Penetration Depth and Scattering Coefficient Analysis*

An important performance measure for optical imaging in tissue is the maximum depth at which images can be obtained, or the penetration depth. Imaging performance for both modalities was analyzed for the 23 biopsies in which consistent features were resolved throughout imaging. For this analysis, penetration depth was defined as the maximum depth at which imaging captured individual nuclei due to the difficulty in differentiating between when the focal plane had entered the stroma with its diffuse, featureless return and when signal return had simply dropped too low to capture information. The results of this analysis are shown in Figure 6.4. The OCM consistently imaged more deeply than the confocal microscope, imaging 100 or more microns deeper in 3 cases, 50 microns or more in 7 cases, and less than 50 microns deeper in 13 cases. Overall, the penetration depth of the OCM exceeded the penetration depth of the confocal by an average 33%. The widely divergent penetration depths for the study (93 – 338 microns for the OCM) illustrate the challenge presented by the diversity of tissue types and pathologic states found in the oral cavity.

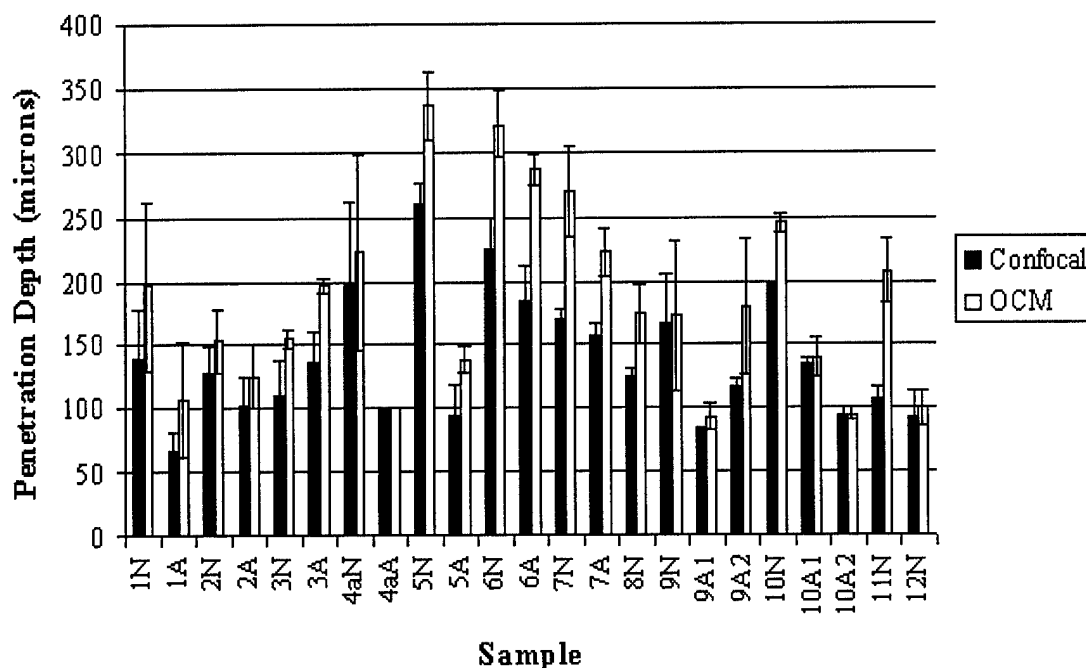


Figure 6.4. Penetration depth of confocal microscope versus OCM system.

An analysis of epithelial scattering coefficients for these samples was also performed. Twenty-nine depth of focus stacks, representing 16 biopsies, were selected. Stacks were chosen based on clarity of nuclei over at least 5 image depths and a maximum of two stacks per biopsy were used. In 23 of 29 stacks, an exponential curve could not be fit to the entire reflected nuclear intensity curve because a region existed at the beginning of the data that did not fit the model. Reflectivities in these regions varied greatly with signal commonly increasing during the first 20 – 50 microns before either remaining relatively constant or dropping off significantly. In 14 of the 23 stacks, the signal started to attenuate exponentially at a specific depth. Upon examination of the pathology diagnosis for these cases, it became apparent that all 23 of these samples came

from hyperkeratotic biopsies while three of the remaining six stacks were SCCs without hyperkeratotic layers and another two came from a biopsy with a very minimal hyperkeratotic layer. Figure 6.5 shows two examples with hyperkeratotic layers clearly distinguishable in both the histology and the normalized nuclear reflectance plots. Figure 6.5A shows a histologic image from a keratin antibody (MMAC) stained section from a hyperkeratotic and hyperplastic gingiva biopsy with a plot of normalized reflected nuclear intensity taken from the same biopsy (Figure 6.5B). The top 10 – 20 microns of the biopsy are heavily keratinized followed by a 40 – 90 micron layer of keratinized cells. This layer is recorded in the plot by a brief period of increasing reflected nuclear intensity before the signal becomes relatively constant until 70 microns below the tissue surface. At this depth, the intensity begins to drop. When the data from 70 – 150 microns is fitted to an exponential curve, the fit constant is 54 (with a mean correlation coefficient of 0.91), implying a scattering coefficient of 27 cm^{-1} . The histologic image in Figure 6.5C from a keratin antibody (MMAC) stained section from a hyperkeratotic, mildly dysplastic gingiva biopsy with focal moderate to severe dysplasia has a thicker 20 – 40 micron, heavily keratinized superficial layer on top of a 30 – 100 micron layer of keratinized cells. This layer is recorded in the plot in Figure 6.5D by a brief period of increasing reflected nuclear intensity before the signal varies significantly until 120 microns below the tissue surface. At this depth, the intensity begins to drop. When the data from 120 – 190 microns is fitted to an exponential curve, the fit constant is 69 (with a mean correlation coefficient of 0.89), implying a scattering coefficient of 34 cm^{-1} .

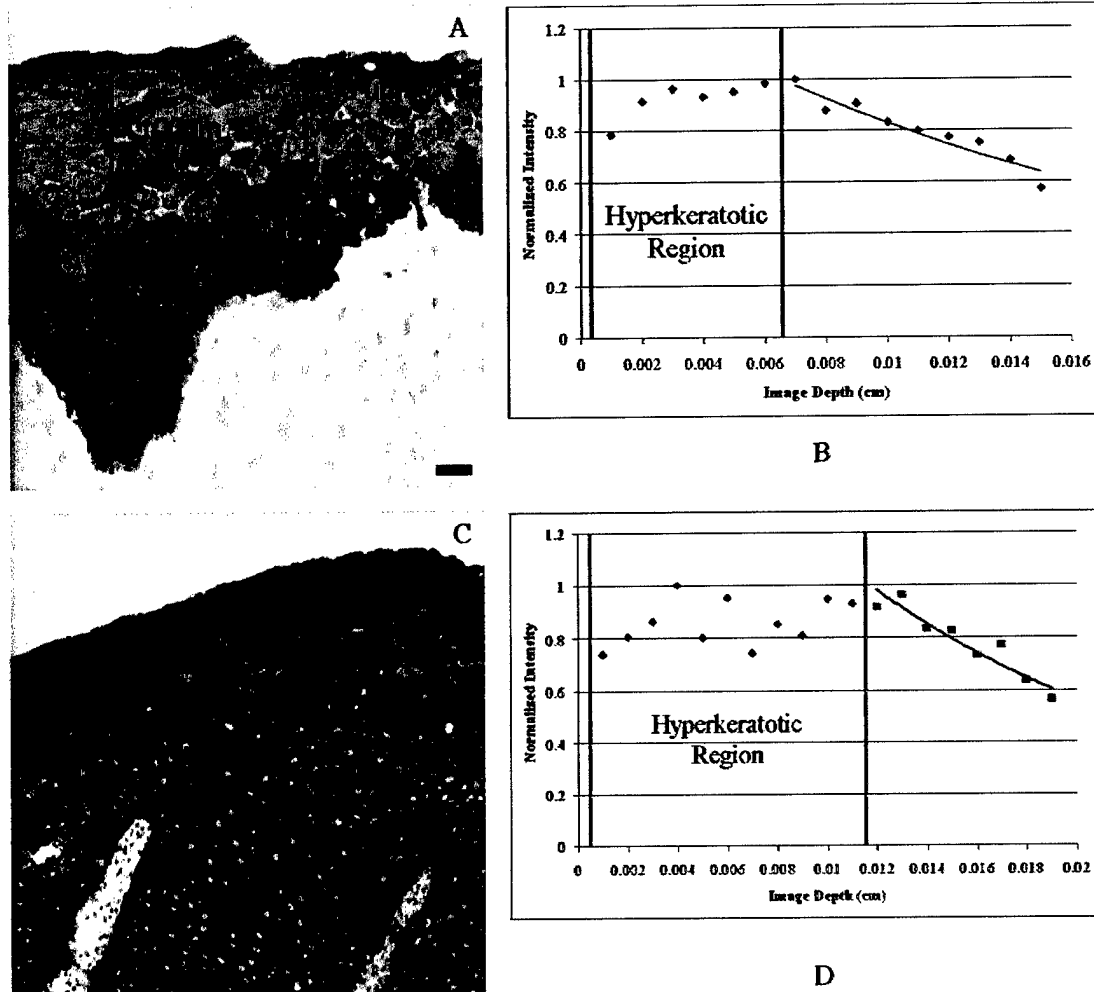


Figure 6.5. Comparison of histology to normalized reflected nuclear intensity as a function of depth. (A) Histologic image from a keratin antibody (MMAC) stained section from a hyperkeratotic and hyperplastic gingiva biopsy. (B) Plot of normalized reflected nuclear intensity taken from the same biopsy in (A) showing characteristic decay within the hyperkeratotic region and exponential attenuation starting at 70 microns with a fit constant of 54 (with a mean correlation coefficient of 0.91), implying a scattering coefficient of 27 cm^{-1} . (C) Histologic image from a keratin antibody (MMAC) stained section from a hyperkeratotic gingiva biopsy with mild dysplasia and focal moderate to severe dysplasia. (D) Plot of normalized reflected nuclear intensity taken from the same biopsy in (C) showing characteristic decay of the hyperkeratotic region and exponential attenuation starting at 120 microns with a fit constant of 69 (with a mean correlation coefficient of 0.88), implying a scattering coefficient of 34 cm^{-1} .

Figure 6.6 shows more examples of normalized nuclear reflectance plots from different sites in the oral cavity representing multiple pathologic states. Figure 6.7A shows a scatter plot of scattering coefficients for the 20 samples that either did not have a hyperkeratotic region or had a second layer that exhibited an exponential attenuation of reflected nuclear intensity, while Figure 6.7B presents the mean scattering coefficients for these stacks by pathologic diagnosis. The mean scattering coefficient for samples from normal biopsies was $27 \pm 11 \text{ cm}^{-1}$, with a minimum and maximum value of 13 and 42 cm^{-1} , respectively, and a mean correlation coefficient of greater than 0.85 for 11 samples and 0.72 for one other. The mean scattering coefficient for samples from dysplastic biopsies rose slightly to $39 \pm 6 \text{ cm}^{-1}$, with a minimum and maximum value of 34 and 48 cm^{-1} , respectively. The mean correlation coefficients for these five samples were greater than 0.89. Finally, the mean scattering coefficient for samples from SCC biopsies was $60 \pm 9 \text{ cm}^{-1}$, with a minimum and maximum value of 54 and 70 cm^{-1} , respectively, with a mean correlation coefficient of great than 0.91 for all 3 samples. While the number of samples from SCC is small, there is definitely an upwards trend in scattering coefficient as the tissue progresses from normal to dysplasia to cancer.

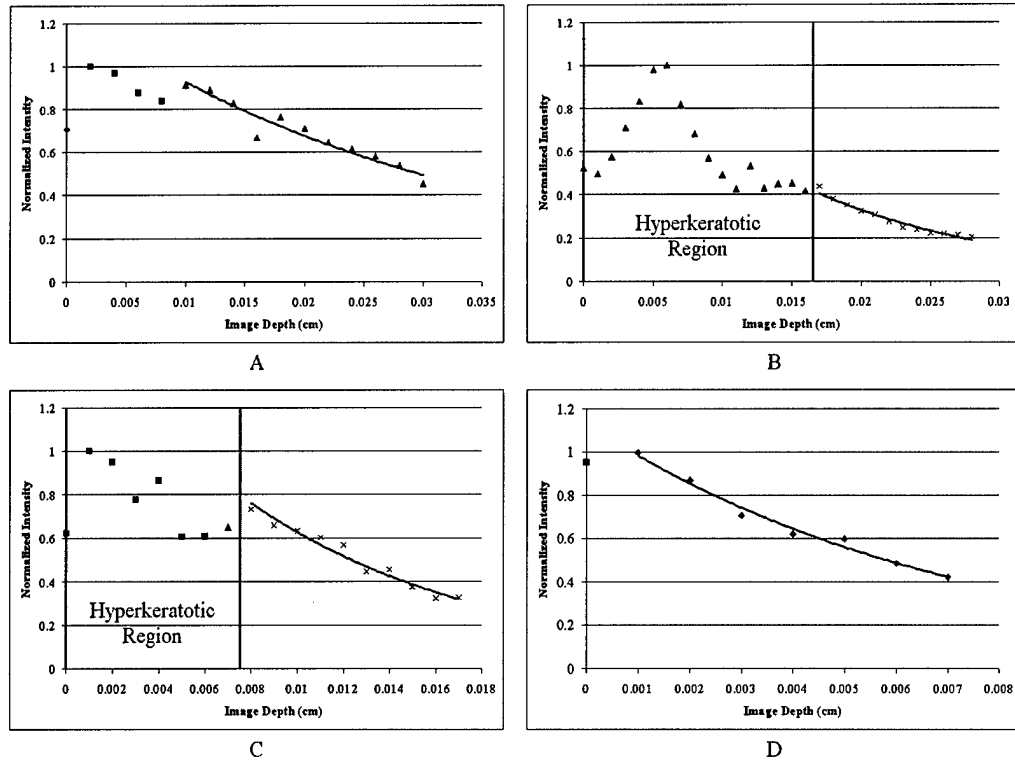


Figure 6.6. Examples of normalized nuclear intensity plots from different sites and pathologic states. (A) Plot from a hyperkeratotic and hyperplastic biopsy from the floor of the mouth with an estimated scattering coefficient of 16 cm^{-1} (mean correlation coefficient of 0.92). (B) Plot from a hyperkeratotic, mildly dysplastic biopsy from the lateral surface of a tongue with an estimated scattering coefficient of 34 cm^{-1} (mean correlation coefficient of 0.96). (C) Plot from a severely hyperkeratotic, moderately dysplastic biopsy from the floor of the mouth with an estimated scattering coefficient of 48 cm^{-1} (mean correlation coefficient of 0.96). (D) Plot from an invasive, well differentiated SCC from the soft palate with an estimated scattering coefficient of 70 cm^{-1} (mean correlation coefficient of 0.98).

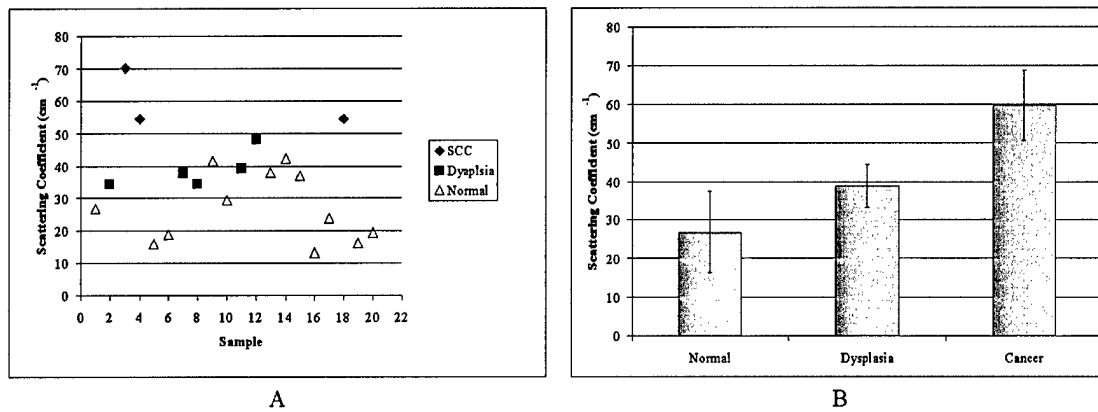


Figure 6.7. (a) Scatter plot of scattering coefficients for non-hyperkeratotic tissue. (b) Bar chart comparing mean scattering coefficients for non-hyperkeratotic tissue by pathologic diagnosis.

6.4 DISCUSSION

The images presented here illustrate the ability of an OCM system to image oral mucosa with resolution comparable to histologic evaluation without tissue preparation and staining. In normal tissue, depth-related changes in cell diameter and nuclear density were observed at multiple anatomic sites within the oral cavity and at deeper depths than achieved with the system's confocal microscope. In SCCs, densely packed, pleomorphic tumor nuclei could be visualized while areas of inflammation appeared. Our images correlate well with histology and are similar to previously reported optical imaging results in the oral cavity [44, 138].

Our study of oral epithelial scattering coefficients emphasizes the role that a hyperkeratotic layer plays in optical imaging of the oral cavity. We believe that the low

levels of reflected intensity at the superficial portion of the hyperkeratotic layer are due to high levels of keratin that lower the index mismatch between nuclei and the surrounding cytoplasm. The reflected intensity increases as the level of keratin in the cytoplasm drops leading to an increase in refractive mismatch. This result supports the conclusion made in a previous study [138] that a larger refractive index exists in the hyperkeratotic layer that would limit the ability of illumination light to reach lower levels in the tissue by increasing specular reflection at the tissue surface. We also believe that the characteristic depth dependent reflectivities observed in the rest of the hyperkeratotic layer are a result of changing levels of keratin in the cytoplasm as well as pyknotic nuclei. Previous studies have shown that chromatin material in the nucleus is responsible for the index mismatch that provides a significant amount of the contrast in optical imaging of amelanotic tissue [43]. Nuclei present in a hyperkeratotic (or parakeratotic) layer are pyknotic due to the death of cells with condensed, irregular chromatin [160]. Varying shapes and DNA levels would cause the reflectivity and scattering function to fluctuate with each individual nucleus.

The scattering coefficients reported here show a definite increasing trend from 27 cm^{-1} in normal tissue to 39 cm^{-1} in dysplastic tissue to 60 cm^{-1} in SCCs. We believe that the increased scattering in abnormal tissue is due to changes in nuclear morphology. Quantitative measures of normal oral epithelium and oral SCC found almost a doubling in DNA content in SCC when compared to normal tissue [161]. Our results are similar to the 22 cm^{-1} and 69 cm^{-1} for normal and dysplastic epithelium, respectively, extracted from cervical tissue confocal images [77] and the 13 cm^{-1} and 142 cm^{-1} for normal and

dysplastic epithelium predicted by our finite difference time domain (FDTD) algorithm which estimated the volume fraction of nuclei and average nuclear size from cervical confocal images [162], with the slightly higher scattering in normal epithelium probably attributable to higher levels of keratin in the cytoplasm.

Recently, a number of studies have suggested that optical spectroscopy and imaging can probe changes in both the epithelium and stroma of both oral and cervical tissue [21, 24, 163-167], but these methods are based on accurate models of the optical properties of the target tissue. Our previous study of cervical epithelial scattering suggested, based on its results for epithelial scattering coefficients, that single layer models that assume tissue is homogeneous are not well suited to describe light propagation in tissue because of the large difference in scattering between epithelium and stroma [77]. Our results further emphasize this point by identifying separate layers within the epithelium with significantly different scattering properties. Therefore, techniques that attempt to accurately model microanatomical and biochemical features of epithelium and their effect on scattering [162, 166-168] will play a vital role in supporting optical spectroscopy as a tool in the oral cavity.

6.5 CONCLUSION

In this study, we have shown the power of optical coherence microscopy to visualize, at the subcellular level, features of both normal and neoplastic oral mucosa throughout the oral cavity. Penetration depths for the OCM were consistently greater than accompanying confocal imaging. Extraction of scattering coefficients from

reflected nuclear intensity was successful in non-hyperkeratotic layers and showed differentiation between scattering properties of normal and dysplastic epithelium and SCCs.

CHAPTER 7

Summary and Conclusions

7.1 SUMMARY OF RESULTS

The work in this dissertation centered on optical imaging in the oral cavity to determine whether confocal microscopy and optical coherence microscopy could detect and diagnose oral neoplasia. The significant number of benign lesions of the oral cavity with similar visual appearance and clinical symptoms and the extensive nature of many oral lesions complicate the task of screening for premalignancies in the mouth. Both of these imaging systems yielded detailed images of cell morphology and tissue architecture for multiple sites and pathologic states of oral mucosa.

An extensive survey of features of normal epithelium and SCCs using an epi-illumination, near real-time reflectance confocal microscope was described in Chapter 3. Nuclear density and morphology differences were resolved between neoplastic and non-neoplastic oral cavity specimens. Other features of non-cancerous and cancerous oral tissue that were identified in the confocal images included areas of inflammation, fibrosis, muscle fibers and salivary glands

A detailed study of the differences between normal, preneoplastic, and neoplastic oral cavity tissue was performed using images from an epi-illumination, reflectance confocal microscope in Chapter 4. Descriptive statistics characterizing nuclear

morphology such as nuclear to cytoplasmic ratio and average nuclear area allowed slight differentiation between normal and dysplastic epithelium. Reviews of confocal images by both trained pathologists and untrained engineers emphasized the need for situational awareness of the region of the epithelium occupied by the image plane.

A description of the design, construction, and characterization of an optical coherence microscope (OCM) is found in Chapter 5. This instrument was built to improve the penetration depth in our studies and allow more imaging of the intermediate and basal layers within oral mucosa. Measured lateral and axial resolutions of 2.3 microns and 7.8 microns satisfied the requirement that the instrument be able to resolve individual nuclei with oral mucosa. An estimated penetration depth (based on SNR) of 690 – 1227 exceeded the measured epithelial thicknesses of 300 – 500 microns.

The increased penetration depths provided by OCM was demonstrated in Chapter 6. Multiple scattering, increased background, and variable tissue architecture prevented the system from achieving the estimated noise-limited penetration depth. In addition, extraction of scattering coefficients from reflected nuclear intensity was successful in non-hyperkeratotic layers and showed differentiation between scattering properties of normal and dysplastic epithelium and SCCs.

Overall, the research in this dissertation gives a thorough basis for optical imaging in the oral cavity. Images were acquired from five separate sites in the oral cavity (tongue, gingiva, floor of the mouth, buccal mucosa, and soft palate) and represented hyperkeratotic, hyperplastic, and dysplastic (primarily mild and moderate dysplasia) mucosa, and mild, moderate, and well differentiated SCC. Two approaches, morphologic

statistical analysis and calculation of scattering coefficients, showed diagnostic contrast with the differentiation from the scattering coefficients being superior

7.2 FUTURE DIRECTIONS

The research presented in this dissertation provides a solid basis for optical imaging in the oral cavity, but there are a number of directions in which further research can progress. Further *in vitro* studies are needed to quantify fully the diagnostic capabilities of optical imaging in the oral cavity. First of all, the diagnostic contrast found in the morphologic statistical and scattering coefficient analyses should be further substantiated by adding more samples to the data set and performing an target analysis of histology to provide a better understanding of key characteristics such as nuclear area and nuclear to cytoplasmic ratio as a function of depth, keratin levels as a function of depth, and hyperkeratotic layer and epithelial thicknesses. Several improvements to the OCM could easily be made to improve penetration depths such as buying a more powerful source and increasing the number of filters used to reduce noise. This increased penetration depth would give the user more confidence in determining when the basal layer of the epithelium has been reached. Finally, the use of other modes of optical imaging such as fluorescence imaging to investigate oral mucosa would provide more information on the content of the tissue, primarily with respect to the presence of keratin.

Optical imaging of the oral cavity will not achieve its full potential until practical *in vivo* imaging is implemented. Advances in flexible reflectance confocal microendoscopes [108 – 116] have shown that this technology can provide the same high

resolution confocal images of tissue as demonstrated in this dissertation but *in vivo* and in a clinical setting. The oral cavity has specific challenges which these endoscopes will need to overcome in order to detect oral neoplasias successfully. The hyperkeratotic superficial layer commonly found in oral mucosa retards penetration of illumination light into deeper epithelial layers while at the same time, levying an increased penetration depth requirement to detect morphologic and scattering changes associated with dysplastic changes. The form factor for the endoscope must enable access to multiple locations in the mouth including the floor of the mouth and gingiva while minimizing discomfort to the patient as sensitive lesions are investigated. Even with these challenges though, optical imaging has the potential to provide a powerful tool for clinical examination of the oral cavity in a wide range of applications such as noninvasive diagnosis of oral lesions, determining tumor margins *in vivo* in real time, and monitoring *in vivo* response of neoplastic cells to therapy.

References

- [1] P. Balaram, H. Sridhar, T. Rajkumar, S. Vaccarella, R. Herrero, A. Nandakumar, K. Ravichandran, K. Ramdas, R. Sankaranarayanan, V. Gajalakshmi, N. Muñoz, and S. Franceschi, "Oral cancer in southern India: the influence of smoking, drinking, paan-chewing and oral hygiene," *International journal of cancer*, vol. 98, pp. 440-5, 2002.
- [2] American Cancer Society, "Cancer facts and figures," Atlanta, 2003.
- [3] L. A. Gloeckler, M. P. Eisner, C. L. Kosary, B. F. Hankey, B. A. Miller, L. X. Clegg, and B. K. Edwards, "SEER cancer statistics review, 1973-1997," National Cancer Institute, Bethesda, MD NIH Pub. No. 00-2789, 2000.
- [4] C. Scully and S. Porter, "ABC of oral health: Swellings and red, white, and pigmented Lesions," *British Medical Journal*, vol. 321, pp. 225-228, 2000.
- [5] C. Scully and S. Porter, "ABC of oral health: Oral cancer," *British Medical Journal*, vol. 321, pp. 97-100, 2000.
- [6] S. Silverman and P. B. Sugerman, "Oral premalignancies and squamous cell carcinoma," *Clinics in Dermatology*, vol. 18, pp. 563-568, 2000.
- [7] F. H. Martini, M. J. Timmons, and M. P. McKinley, *Human anatomy*, 3rd ed. Upper Saddle River, N. J.: Prentice Hall, 2000.
- [8] T. A. Winning and G. C. Townsend, "Oral mucosal embryology and histology," *Clinics in Dermatology*, vol. 18, pp. 499-511, 2000.
- [9] M. H. Ross, L. J. Romrell, and G. I. Kaye, *Histology: A Text and Atlas*, 3rd ed. Baltimore, MD: William & Wilkins, 1995.

- [10] W. G. Shafer, M. K. Hine, and B. M. Levy, *Textbook of Oral Pathology*, 4th ed. Philadelphia: W. B. Saunders, 1983.
- [11] American Cancer Society, "Testing biopsy and cytology specimens for cancer," 2001.
- [12] J. J. Sciubba, "Oral cancer: The importance of early diagnosis and treatment," *American Journal of Clinical Dermatology*, vol. 2, pp. 239-251, 2001.
- [13] D. Eisen, "The oral brush biopsy: A new reason to screen every patient for oral cancer," *General Dentistry*, vol. 48, pp. 96-99, 2000.
- [14] M. A. Kahn, "Oral exfoliative cytology procedures: Conventional, brush biopsy and ThinPrep," *Journal of the Tennessee Dental Association*, vol. 81, pp. 17-20, 2001.
- [15] L. G. Koss, "Cytologic diagnosis of oral, esophageal, and peripheral lung cancer," *Journal of Cellular Biochemistry*, vol. Supplement 17F, pp. 66-81, 1993.
- [16] J. J. Sciubba, "Improving detection of precancerous and cancerous oral lesions: Computer-assisted analysis of the oral brush biopsy," *Journal of the American Dental Association*, vol. 130, pp. 1445-57, 1999.
- [17] A. J. Ligthelm, A. Weber, P. J. van Niekerk, and W. F. van Heerden, "Diagnosis of oral precancer and cancer," *The Journal of the Dental Association of South Africa*, vol. Suppl1, pp. 2-8, 1989.
- [18] E. Dabelsteen, B. Roed-Petersen, C. J. Smith, and J. J. Pindborg, "The limitations of exfoliative cytology for the detection of epithelial atypia in oral leukoplakias," *British journal of cancer*, vol. 25, pp. 21-4, 1971.
- [19] C.-T. Chen, C.-Y. Wang, Y.-S. Kuo, H. H. Chiang, S.-N. Chow, I.-Y. Hsiao, and C.-P. Chiang, "Light-induced fluorescence spectroscopy: A potential diagnostic

- tool for oral neoplasia," *Proceedings of the National Science Council, ROC, Part B: Life Sciences*, vol. 20, pp. 12-130, 1996.
- [20] J. K. Dhingra, X. Zhang, K. McMillan, S. Kabani, R. Manoharan, I. Itzkan, M. S. Feld, and S. M. Shapshay, "Diagnosis of head and neck precancerous lesions in an animal model using fluorescence spectroscopy," *Laryngoscope*, vol. 108, pp. 471-475, 1998.
- [21] A. Gillenwater, R. Jacob, R. Ganeshappa, B. Kemp, A. K. El-Naggar, J. L. Palmer, G. Clayman, M. F. Mitchell, and R. Richards-Kortum, "Noninvasive diagnosis of oral neoplasia based on fluorescence spectroscopy and native tissue autofluorescence," *Archives of Otolaryngology -- Head & Neck Surgery*, vol. 124, pp. 1251-1258, 1998.
- [22] A. Gillenwater, R. Jacob, and R. Richards-Kortum, "Fluorescence spectroscopy: A technique with potential to improve the early detection of aerodigestive tract neoplasia," *Head & Neck*, vol. 20, pp. 556-562, 1998.
- [23] D. L. Heintzelman, U. Utzinger, H. Fuchs, A. Zuluaga, K. Gossage, A. M. Gillenwater, R. Jacob, B. Kemp, and R. R. Richards-Kortum, "Optimal excitation wavelengths for *in vivo* detection of oral neoplasia using fluorescence spectroscopy," *Photochemistry & Photobiology*, vol. 72, pp. 103-113, 2000.
- [24] B. Kulapaditharom and V. Boonkitticharoen, "Laser-induced fluorescence imaging in localization of head and neck cancers," *Annals of Otology, Rhinology & Laryngology*, vol. 107, pp. 241-246, 1998.
- [25] M. W. van den Brekel, R. W. Runne, L. E. Smeele, R. M. Tiwari, G. B. Snow, and J. A. Castelijns, "Assessment of tumour invasion into the mandible: The value

- of different imaging techniques," *European Radiology*, vol. 8, pp. 1552-1557, 1998.
- [26] M. Crecco, A. Vidiri, O. Palma, R. Floris, E. Squillaci, M. Mattioli, F. Marzetti, and S. Squillaci, "T stages of tumors of the tongue and floor of the mouth: Correlation between MR with gadopentetate dimeglumine and pathologic data," *American Journal of Neuroradiology*, vol. 15, pp. 1695-1702, 1994.
- [27] R. Hermans, L. Verwaerde, T. De Schrijver, and A. L. Baert, "CT and MR imaging in tumors of the tongue, tongue base, and floor of the mouth: A comparative study," *Journal Belge de Radiologie*, vol. 77, pp. 78-83, 1994.
- [28] A. Leslie, E. Fyfe, P. Guest, P. Goddard, and J. Kabala, "Staging of squamous cell carcinoma of the oral Cavity and oropharynx: A comparison of MRI and CT in T- and N-staging," *Journal of Computer Assisted Tomography*, vol. 23, pp. 43-49, 1999.
- [29] R. B. Lufkin, "Imaging neoplasms of the head and neck and central nervous system," in *Cancer Medicine*, R. C. Bast, Jr., D. W. Kufe, R. E. Pollock, R. R. Weichselbaum, J. F. Holland, and E. Frei, III, Eds., 5th ed. Hamilton: B. C. Decker, Inc., 2000.
- [30] R. Maroldi, G. Battaglia, D. Farina, P. Maculotti, and A. Chiesa, "Tumours of the oropharynx and oral cavity: Perineural spread and bone invasion," *Organe de la Societe Royale Belge de Radiologie*, vol. 82, pp. 294-300, 1999.
- [31] V. M. Moharir, M. P. Fried, D. M. Vernick, I. P. Janecka, J. Zahajsky, L. Hsu, W. E. Lorensen, M. Anderson, W. M. Wells, P. Morrison, and R. Kikinis, "Computer-assisted three-dimensional reconstruction of head and neck tumors," *Laryngoscope*, vol. 108, pp. 1592-1598, 1998.

- [32] S. K. Mukherji, J. Castelijns, and M. i. Castillo, "Squamous cell carcinoma of the oropharynx and oral cavity: How imaging makes a difference," *Seminars in Ultrasound, CT & MR*, vol. 19, pp. 463-475, 1998.
- [33] R. Murakami, Y. Baba, R. Nishimura, T. Baba, T. Nakaura, T. Ishikawa, and M. Takahashi, "MR imaging of squamous cell carcinoma of the floor of the mouth: Appearance of the sublingual and submandibular glands," *Acta Radiologica*, vol. 40, pp. 276-281, 1999.
- [34] M. Ozturk, I. Yorulmaz, E. Guney, and N. Ozcan, "Masses of the tongue and floor of the mouth: findings on magnetic resonance imaging," *European Radiology*, vol. 10, pp. 1669-1674, 2000.
- [35] R. Sigal, A. M. Zagdanski, G. Schwaab, J. Bosq, A. Auperin, A. Laplanche, J. P. Francke, F. Eschwege, B. Luboinski, and D. Vanel, "CT and MR imaging of squamous cell carcinoma of the tongue and floor of the mouth," *Radiographics*, vol. 16, pp. 787-810, 1996.
- [36] H. Konouchi, J. Asaumi, Y. Yanagi, H. Shigehara, M. Hisatomi, H. Matsuzaki, and K. Kishi, "Evaluation of tumor proliferation using dynamic contrast enhanced-MRI of oral cavity and oropharyngeal squamous cell carcinoma," *Oral oncology*, vol. 39, pp. 290-5, 2003.
- [37] C. Bertrand and P. Corcuff, "In vivo spatio-temporal visualization of the human skin by real-time confocal microscopy," *Scanning*, vol. 16, pp. 150-154, 1993.
- [38] T. Collier, P. Shen, B. de Pradier, and R. Richards-Kortum, "Near real time confocal microscopy of amelanotic tissue: Dynamics of aceto-whitening enable nuclear segmentation," *Optics Express*, vol. 6, pp. 40-48, 2000.

- [39] S. Gonzalez, M. Rajadhyaksha, A. Gonzalez-Serva, W. M. White, and R. R. Anderson, "Confocal reflectance imaging of folliculitis *in vivo*: Correlation with routine histology," *Journal of Cutaneous Pathology*, vol. 26, pp. 201-205, 1999.
- [40] J. V. Jester, P. M. Andrews, W. M. Petroll, M. A. Lemp, and H. D. Cavanaugh, "In vivo, real-time confocal imaging," *Journal of Electron Microscopy Technique*, vol. 18, pp. 50-60, 1991.
- [41] B. R. Masters, D. J. Aziz, A. F. Gmitro, J. H. Kerr, T. C. O'Grady, and L. Goldman, "Rapid observation of unfixed, unstained human skin biopsy specimens with confocal microscopy and visualization," *Journal of Biomedical Optics*, vol. 2, pp. 437-445, 1997.
- [42] M. Rajadhyaksha, R. R. Anderson, and R. H. Webb, "Video-rate confocal scanning laser microscope for imaging human tissues *in vivo*," *Applied Optics*, vol. 38, pp. 2105-2115, 1999.
- [43] C. L. Smithpeter, A. K. Dunn, R. Drezek, T. Collier, and R. Richards-Kortum, "Near real time confocal microscopy of cultured amelanotic cells: Sources of signal, contrast agents, and limits of contrast," *Journal of Biomedical Optics*, vol. 3, pp. 429-436, 1998.
- [44] W. M. White, M. Rajadhyaksha, S. Gonzalez, R. L. Fabian, and R. R. Anderson, "Noninvasive imaging of human oral mucosa *in vivo* by confocal reflectance microscopy," *Laryngoscope*, vol. 109, pp. 1709-1717, 1999.
- [45] M. E. Brezinski, G. J. Tearney, B. E. Bouma, J. A. Izatt, M. R. Hee, E. A. Swanson, J. F. Southern, and J. G. Fujimoto, "Optical coherence tomography for optical biopsy," *Circulation*, pp. 1206-1213, 1996.

- [46] J. Colston B. W., M. J. Everett, U. S. Sathyam, L. B. DaSilva, and L. L. Otis, "Imaging of the oral cavity using optical coherence tomography," *Monographs in Oral Science*, vol. 17, pp. 32-55, 2000.
- [47] F. I. Feldchtein, V. M. Gelikonov, G. V. Gelikonov, R. V. Kuranov, N. D. Gladkova, A. M. Sergeev, N. M. Shakhova, I. A. Kuznetzova, A. M. Denisenko, and O. S. Streltsova, "Design and performance of an endoscopic OCT system for *in vivo* studies of human mucosa," presented at Conference on Lasers and Electro-Optics, San Francisco, CA, 1998.
- [48] D. Huang, E. A. Swanson, C. P. Lin, J. S. Schuman, W. G. Stinson, W. Chang, M. R. Hee, T. Flotte, K. Gregory, C. A. Puliafito, and J. G. Fujimoto, "Optical coherence tomography," *Science*, vol. 254, pp. 1178, 1991.
- [49] Y. Pan and D. L. Farkas, "Noninvasive imaging of living human skin with dual-wavelength optical coherence tomography in two and three dimensions," *Journal of Biomedical Optics*, vol. 3, pp. 446-455, 1998.
- [50] A. M. Rollins, R. Ung-Arunyawee, A. Chak, R. C. K. Wong, K. Kobayashi, M. V. Sivak, and J. A. Izatt, "Real-time *in vivo* imaging of human gastrointestinal ultrastructure by use of endoscopic optical coherence tomography with a novel efficient interferometer design," *Optics Letters*, vol. 24, pp. 1358-1360, 1999.
- [51] J. M. Schmitt, M. J. Yadlowsky, and R. F. Bonner, "Subsurface imaging of living skin with optical coherence microscopy," *Dermatology*, vol. 191, pp. 93-98, 1995.
- [52] H.-W. Wang, "Incoherent and coherent microscopies for analysis of tissue structure and function," in *Department of Biomedical Engineering*. Cleveland: Case Western University, 1999, pp. 1-112.

- [53] F. Xu, H. E. Pudavar, P. N. Prasad, and D. Dickensheets, "Confocal enhanced optical coherence tomography for nondestructive evaluation of paints and coatings," *Optics Letters*, vol. 24, pp. 1808-1810, 1999.
- [54] M. Bashkansky, M. D. Duncan, M. Kahn, D. Lewis, III, and J. Reintjes, "Subsurface defect detection in ceramics by high-speed high-resolution optical coherence tomography," *Optics Letters*, vol. 22, pp. 61-63, 1997.
- [55] E. Beaurepaire, L. Moreaux, F. Amblard, and J. Mertz, "Combined scanning optical coherence and two-photon-excited fluorescence microscopy," *Optics Letters*, vol. 24, pp. 969-971, 1999.
- [56] K. Bizheva, A. Siegel, and D. Boad, "Optical coherence microscopy of Brownian motion as a tool for studying the effect of multiple scattering on depth penetration in turbid media," presented at Conference on Lasers and Electro-Optics, San Francisco, CA, 1998.
- [57] M. D. Duncan, M. Bashkansky, and J. Reintjes, "Subsurface defect detection in materials using optical coherence tomography," *Optics Express*, vol. 2, pp. 540-545, 1998.
- [58] J. W. Hettinger, M. de la Pena Mattozzi, W. R. Myers, M. E. Williams, A. Reeves, R. L. Parsons, R. C. Haskell, R. Wang, and J. I. Medford, "Optical coherence microscopy. A technology for rapid, *in vivo*, non-destructive visualization of plants and plant cells," *Plant Physiology*, vol. 123, pp. 3-15, 2000.
- [59] J. A. Izatt, M. D. Kulkarni, H.-W. Wang, K. Kobayashi, and M. V. Sivak, "Optical coherence tomography and microscopy in gastrointestinal tissues," *IEEE Journal of Selected Topics in Quantum Electronics*, vol. 2, pp. 1017-1028, 1996.

- [60] A. G. Podoleanu, G. M. Dobre, and D. A. Jackson, "En-face coherence imaging using galvanometer scanner modulation," *Optics Letters*, vol. 23, pp. 147-149, 1998.
- [61] J. M. Schmitt, S. L. Lee, and K. M. Yung, "An optical coherence microscope with enhanced resolving power in thick tissue," *Optics Communications*, vol. 142, pp. 203-207, 1997.
- [62] M. Minsky, "Microscopy apparatus." U. S., 1961.
- [63] A. Hall, M. Browne, and V. Howard, "Confocal microscopy - The basics explained," *Royal Microscopical Society Journal of Microscopy*, vol. 26, pp. 63-68, 1991.
- [64] T. Wilson, "Confocal microscopy," in *Confocal Microscopy*, T. Wilson, Ed. London: Academic Press, 1990, pp. 1-64.
- [65] R. H. Webb, "Confocal optical microscopy," *Reports on Progress in Physics*, vol. 59, pp. 427-471, 1996.
- [66] C. L. Smithpeter, "Fiber optics confocal imaging for *in vivo* detection and diagnosis of pre-cancerous lesions," in *Department of Electrical Engineering*. Austin: University of Texas at Austin, 1997, pp. 1-166.
- [67] T. Wilson and A. R. Carlini, "Size of the detector in confocal imaging systems," *Optics Letters*, vol. 12, pp. 227-229, 1987.
- [68] T. Wilson, "The role of the pinhole in confocal imaging systems," in *Handbook of Biological Confocal Microscopy*, J. B. Pawley, Ed., 2nd ed. New York: Plenum Press, 1995.
- [69] S. Kimura and T. Wilson, "Confocal scanning optical microscope using single-mode fiber for signal detection," *Applied Optics*, vol. 30, pp. 2143-2150, 1991.

- [70] M. Gu, C. J. R. Sheppard, and X. Gan, "Image formation in a fiber-optical confocal scanning microscope," *Journal of the Optical Society of America A: Optics, Image Science, and Vision*, vol. 8, pp. 1755-1761, 1991.
- [71] J. A. Izatt, M. R. Hee, and G. M. Owen, "Optical coherence microscopy in scattering media," *Optics Letters*, vol. 19, pp. 590, 1994.
- [72] J. M. Schmitt, A. Knüttel, and M. Yadlowsky, "Confocal microscopy in turbid media," *Journal of the Optical Society of America A: Optics, Image Science, and Vision*, vol. 11, pp. 2226-2235, 1994.
- [73] M. Kempe and W. Rudolph, "Analysis of heterodyne and confocal microscopy for illumination with broad-bandwidth light," *Journal of Modern Optics*, vol. 43, pp. 2189-2204, 1996.
- [74] M. Kempe, W. Rudolph, and E. Welsh, "Comparative study of confocal and heterodyne microscopy for imaging through scattering media," *Journal of the Optical Society of America A: Optics, Image Science, and Vision*, vol. 13, pp. 46-52, 1996.
- [75] A. K. Dunn, C. Smithpeter, A. J. Welch, and R. Richards-Kortum, "Sources of contrast in confocal reflectance imaging," *Applied Optics*, vol. 35, pp. 3441-3446, 1996.
- [76] C. L. Smithpeter, A. K. Dunn, A. J. Welch, and R. Richards-Kortum, "Penetration depth limits of *in vivo* confocal reflectance imaging," *Applied Optics*, vol. 37, pp. 2749-2754, 1998.
- [77] T. Collier, D. Arifler, R. Richards-Kortum, A. Malpica, and M. Follen, "Determination of epithelial tissue scattering coefficient using confocal

- microscopy," *IEEE Journal of Selected Topics in Quantum Electronics*, Accepted for Publication.
- [78] B. R. Masters, G. Gonnord, and P. Corcuff, "Three-dimensional microscopic biopsy of *in vivo* human skin: A new technique based on a flexible confocal microscope," *Journal of Microscopy*, vol. 185, pp. 329-338, 1997.
 - [79] C. Toth, D. Narayan, S. Boppart, M. Hee, J. Fujimoto, R. Birngruber, C. Cain, C. DiCarlo, and W. Roach, "A comparison of retinal morphology viewed by optical coherence tomography and by light microscopy," *Archives of Ophthalmology*, vol. 115, pp. 1425-1428, 1997.
 - [80] C. D. DiCarlo, W. P. Roach, D. A. Gagliano, S. A. Boppart, D. X. Hammer, A. B. Cox, and J. G. Fujimoto, "Comparison of optical coherence tomography imaging of cataracts with histopathology," *Journal of Biomedical Optics*, vol. 4, pp. 450, 1999.
 - [81] M. G. Ducros, J. F. de Boer, H.-E. H. Huang, L. C. Chao, Z. Chen, J. S. Nelson, T. E. Milner, and H. G. Rylander, III, "Polarization sensitive optical coherence tomography of the rabbit eye," *IEEE Journal of Selected Topics in Quantum Electronics*, vol. 5, pp. 1159-1167, 1999.
 - [82] M. R. Hee, J. A. Izatt, E. A. Swanson, D. Huang, J. S. Schuman, C. P. Lin, C. A. Puliafito, and J. G. Fujimoto, "Optical coherence tomograph for ophthalmic imaging," *IEEE Engineering in Medicine and Biology*, pp. 67-76, 1995.
 - [83] V. Kamensky, F. I. Feldchtein, V. M. Gelikonov, L. Snopova, S. Muraviov, A. Malyshev, N. Bityurin, and A. M. Sergeev, "*In situ* monitoring of laser modification process in human cataractous lens and porcine cornea using coherence tomography," *Journal of Biomedical Optics*, vol. 4, pp. 137-143, 1999.

- [84] Y. Pan, E. Lankenau, J. Welzel, R. Birngruber, and R. Engelhardt, "Optical coherence-gated imaging of biological tissues," *IEEE Journal of Selected Topics in Quantum Electronics*, vol. 2, pp. 1029-1034, 1996.
- [85] J. M. Schmitt and S. H. Xiang, "Cross-polarized backscatter in optical coherence tomography of biological tissue," *Optics Letters*, vol. 23, pp. 1060-1062, 1998.
- [86] B. W. Colston, M. J. Everett, and L. B. Da Silva, "Imaging of hard- and soft-tissue structure in the oral cavity by optical coherence tomography," *Applied Optics*, vol. 37, pp. 3582-3585, 1998.
- [87] L. L. Otis, M. J. Everett, U. S. Sathyam, and B. W. Colston, Jr, "Optical coherence tomography: a new imaging technology for dentistry," *Journal of the American Dental Association*, vol. 131, pp. 511-514, 2000.
- [88] M. E. Brezinski and J. G. Fujimoto, "Optical coherence tomography: High-resolution imaging in nontransparent tissue," *IEEE Journal of Selected Topics in Quantum Electronics*, vol. 5, pp. 1185-1192, 1999.
- [89] A. V. D'Amico, M. Weinstein, X. Li, J. P. Richie, and J. G. Fujimoto, "Optical coherence tomography as a method for identifying benign and malignant microscopic structures in the prostate gland," *Urology*, vol. 55, pp. 783-787, 2000.
- [90] C. Pitris, S. A. Boppart, M. E. Brezinski, B. E. Bouma, and J. G. Fujimoto, "Cellular and neoplastic tissue imaging with optical coherence tomography," presented at Conference on Lasers and Electro-Optics Europe, San Francisco, CA, 1998.
- [91] J. M. Schmitt, "Optical coherence tomography (OCT): A review," *IEEE Journal of Selected Topics in Quantum Electronics*, vol. 5, pp. 1205-1215, 1999.

- [92] B. E. Bouma, G. J. Tearney, S. A. Boppart, M. R. Hee, M. E. Brezinski, and J. G. Fujimoto, "High-resolution optical coherence tomographic imaging using a mode locked Ti:Al₂O₃ laser source," *Optics Letters*, vol. 20, pp. 1486-1488, 1995.
- [93] A. M. Rollins, M. D. Kulkarni, S. Yazdanfar, R. Ung-Arunyawee, and J. A. Izatt, "In vivo video rate optical coherence tomography," *Optics Express*, vol. 3, pp. 219-229, 1998.
- [94] J. M. Schmitt and A. Knüttel, "Model of optical coherence tomography of heterogeneous tissue," *Journal of the Optical Society of America A: Optics, Image Science, and Vision*, vol. 14, pp. 1231-1242, 1997.
- [95] M. Bashkansky and J. Reintjes, "Statistics and reduction of speckle in optical coherence tomography," *Optics Letters*, vol. 25, pp. 545-547, 2000.
- [96] E. Beaurepaire, A. C. Boccara, M. Lebec, L. Blanchot, and H. Saint-James, "Full-field optical coherence microscopy," *Optics Letters*, vol. 23, pp. 244-246, 1998.
- [97] A. G. Podoleanu and D. A. Jackson, "Combined optical coherence tomograph and scanning laser ophthalmoscope," *Electronics Letters*, vol. 34, pp. 1088-1090, 1998.
- [98] A. G. Podoleanu and D. A. Jackson, "Simultaneous optical coherence tomography and confocal imaging for retinal investigations," *Proceedings of SPIE - The International Society for Optical Engineering Laser Spectroscopy and Optical Diagnostics: Novel Trends and Applications in laser Chemistry, Biophysics, and Biomedicine*, vol. 3732, pp. 362-366, 1998.
- [99] A. G. Podoleanu, J. A. Rogers, and D. A. Jackson, "OCT en-face images from the retina with adjustable depth resolution in real time," *IEEE Journal of Selected Topics in Quantum Electronics*, vol. 5, pp. 1176-1184, 1999.

- [100] A. G. Podoleanu, J. A. Rogers, and D. A. Jackson, "Three dimensional OCT images from retina and skin," *Optics Express*, vol. 7, pp. 292-298, 2000.
- [101] A. G. Podoleanu, M. Seeger, G. M. Dobre, D. J. Webb, D. A. Jackson, and F. W. Fitzke, "Transversal and longitudinal images from the retina of the living eye using low coherence reflectometry," *Journal of Biomedical Optics*, vol. 3, pp. 12-20, 1998.
- [102] J. M. Schmitt, "Array detection for speckle reduction in optical coherence microscopy," *Physics in Medicine and Biology*, vol. 42, pp. 1427-1439, 1997.
- [103] H.-W. Wang, A. M. Rollins, and J. A. Izatt, "High speed, full field optical coherence microscopy," presented at Conference on Coherence Domain Optical Methods in Biomedical Science and Clinical Applications III, Bellingham, WA, 1999.
- [104] A. Reeves, R. L. Parsons, J. W. Hettinger, and J. I. Medford, "In vivo three-dimensional imaging of plants with optical coherence microscopy," *Journal of microscopy*, vol. 208, pp. 177-89, 2002.
- [105] M. Rajadhyaksha, S. Gonzalez, J. M. Zavislan, R. R. Anderson, and R. H. Webb, "In vivo confocal scanning laser microscopy of human skin II: Advances in instrumentation and comparison with histology," *Journal of Investigative Dermatology*, vol. 113, pp. 293-303, 1999.
- [106] M. Rajadhyaksha, M. Grossman, D. Esterowitz, R. H. Webb, and R. R. Anderson, "In vivo confocal scanning laser microscopy of human skin: Melanin provides strong contrast," *Journal of Investigative Dermatology*, vol. 104, pp. 946-952, 1995.

- [107] T. Collier, A. Lacy, R. Richards-Kortum, A. Malpica, and M. Follen, "Near real-time confocal microscopy of amelanotic tissue: Detection of dysplasia in *ex vivo* cervical tissue," *Academic Radiology*, vol. 9, pp. 504-512, 2002.
- [108] K. B. Sung, C. Liang, M. Descour, T. Collier, M. Follen, A. Malpica, and R. Richards-Kortum, "Near real time *in vivo* fibre optic confocal microscopy: Sub-cellular structure resolved," *Journal of microscopy*, vol. 207(Pt) 2, pp. 137-45, 2002.
- [109] K.-B. Sung, L. Chen, M. Descour, T. Collier, M. Follen, and R. Richards-Kortum, "Fiber-optic confocal reflectance microscope with miniature objective for *in vivo* imaging of human tissues," *IEEE Transactions on Biomedical Engineering*, vol. 49, pp. 1168-1172, 2002.
- [110] P. M. Delaney, M. R. Harris, and R. G. King, "A fibre optic bundle confocal endomicroscope," *Clinical and Experimental Pharmacology and Physiology*, vol. 20, pp. 197-198, 1993.
- [111] G. J. Tearney, R. H. Webb, and B. E. Bouma, "Spectrally encoded confocal microscopy," *Optics Letters*, vol. 23, pp. 1152-1154, 1998.
- [112] A. F. Gmitro and D. J. Aziz, "Confocal microscopy through a fiber-optic imaging bundle," *Optics Letters*, vol. 18, pp. 565-567, 1993.
- [113] P. M. Delaney, M. R. Harris, and R. G. King, "Fiber optic laser scanning confocal microscopy suitable for fluorescence imaging," *Applied Optics*, vol. 33, pp. 573-577, 1994.
- [114] Y. S. Sabharwal, A. R. Rouse, L. Donaldson, M. F. Hopkins, and A. F. Gmitro, "Slit-scanning confocal microendoscope for high-resolution *in vivo* imaging," *Applied Optics*, vol. 38, pp. 7133-7144, 1999.

- [115] J. Knittel, L. Schnieder, G. Guess, B. Messerschmidt, and T. Possner, "Endoscope-compatible confocal microscope using a gradient index-lens system," *Optics Communications*, vol. 188, pp. 267-273, 2001.
- [116] P. Lane, A. Dlugan, and C. MacAulay, "DMD enabled confocal microendoscopy," presented at Coherence Domain Methods in Biomedical Science and Clinical Applications V, San Jose, CA, 2001.
- [117] P. Corcuff, G. Gonnord, G. E. Piérard, and J. L. Lévêque, "*In vivo* confocal microscopy of human skin: A new design for cosmetology and dermatology," *Scanning*, vol. 18, pp. 351-5, 1996.
- [118] S. González, M. Rajadhyaksha, G. Rubinstein, and R. R. Anderson, "Characterization of psoriasis *in vivo* by reflectance confocal microscopy," *Journal of medicine*, vol. 30, pp. 337-56, 1999.
- [119] K. J. Busam, K. Hester, C. Charles, D. L. Sachs, C. R. Antonescu, S. Gonzalez, and A. C. Halpern, "Detection of clinically amelanotic malignant melanoma and assessment of its margins by *in vivo* confocal scanning laser microscopy," *Archives of dermatology*, vol. 137, pp. 923-9, 2001.
- [120] R. G. Langley, M. Rajadhyaksha, P. J. Dwyer, A. J. Sober, T. J. Flotte, and R. R. Anderson, "Confocal scanning laser microscopy of benign and malignant melanocytic skin lesions *in vivo*," *Journal of the American Academy of Dermatology*, vol. 45, pp. 365-76, 2001.
- [121] S. Gonzalez and Z. Tannous, "Real-time, *in vivo* confocal reflectance microscopy of basal cell carcinoma," *Journal of the American Academy of Dermatology*, vol. 47, pp. 869-874, 2002.

- [122] H. Inoue, T. Igari, T. Nishikage, K. Ami, T. Yoshida, and T. Iwai, "A novel method of virtual histopathology using laser-scanning confocal microscopy in-vitro with untreated fresh specimens from the gastrointestinal mucosa," *Endoscopy*, vol. 32, pp. 439-43, 2000.
- [123] R. A. Drezek, T. Collier, C. K. Brookner, A. Malpica, R. Lotan, R. R. Richards-Kortum, and M. Follen, "Laser scanning confocal microscopy of cervical tissue before and after application of acetic acid," *American journal of obstetrics and gynecology*, vol. 182, pp. 1135-9, 2000.
- [124] H. L. Riviere, *Lab Manual of Normal Oral Histology*. Chicago, IL: Quintessence Publishing Co., Inc, 2000.
- [125] R. O. Prum, R. H. Torres, S. Williamson, and J. Dyck, "Coherent light scattering by blue feather barbs," *Nature*, vol. 396, pp. 28-29, 1998.
- [126] A. Brunsting and P. F. Mullaney, "Differential light scattering from spherical mammalian cells," *Biophysical Journal*, vol. 14, pp. 439-453, 1974.
- [127] J. Incze, C. W. Vaughan, Jr., P. Lui, M. S. Strong, and B. Kulapaditharom, "Premalignant changes in normal appearing epithelium in patients with squamous cell carcinoma of the upper aerodigestive tract," *American journal of surgery*, vol. 144, pp. 401-405, 1982.
- [128] J. A. Brennan and D. Sidransky, "Molecular staging of head and neck squamous carcinoma," *Cancer and metastasis reviews*, vol. 15, pp. 3-10, 1996.
- [129] M. Rajadhyaksha, G. Menaker, T. Flotte, P. J. Dwyer, and S. González, "Confocal examination of nonmelanoma cancers in thick skin excisions to potentially guide Mohs micrographic surgery without frozen histopathology," *The Journal of investigative dermatology*, vol. 117, pp. 1137-43, 2001.

- [130] G. Vargas, K. F. Chan, S. L. Thomsen, and A. J. Welch, "Use of osmotically active agents to alter optical properties of tissue: Effects on the detected fluorescence signal measured through skin," *Lasers in surgery and medicine*, vol. 29, pp. 213-20, 2001.
- [131] A. Mashberg and A. M. Samit, "Early detection, diagnosis, and management of oral and oropharyngeal cancer," *CA: a cancer journal for clinicians*, vol. 39, pp. 67-88, 1989.
- [132] J. Guggenheimer, R. S. Verbin, J. T. Johnson, C. A. Horkowitz, and E. N. Myers, "Factors delaying the diagnosis of oral and oropharyngeal carcinomas," *Cancer*, vol. 64, pp. 932-5, 1989.
- [133] M. R. Curtis, "How many oral cancers have you found - or missed - lately?," *Postgraduate Medicine*, vol. 86, pp. 279-280, 1989.
- [134] A. Mashberg and L. J. Feldman, "Clinical criteria for identifying early oral and oropharyngeal carcinoma: erythroplasia revisited," *American journal of surgery*, vol. 156, pp. 273-5, 1988.
- [135] B. R. Masters, G. Gonnord, G. E. Piérard, and Leveque, "*In vivo* confocal microscopy of human skin: A new design for cosmetology and dermatology," *Scanning*, vol. 18, pp. 351-355, 1996.
- [136] T. F. Watson, W. M. Petroll, H. D. Cavanagh, and J. V. Jester, "*In vivo* confocal microscopy in clinical dental research: An initial appraisal," *Journal of dentistry*, vol. 20, pp. 352-8, 1992.
- [137] W. M. Petroll, J. V. Jester, and H. D. Cavanagh, "*In vivo* confocal imaging," *International review of experimental pathology*, vol. 36, pp. 93-129, 1996.

- [138] A. Clark, A. M. Gillenwater, T. Collier, R. Alizadeh-Naderi, A. K. El-Naggar, and R. R. Richards-Kortum, "Confocal microscopy for real time detection of oral cavity neoplasia," *Accepted for publication by Clinical Cancer Research*, 2001.
- [139] J. Meyer and S. Gerson, "A comparison of human palatal and buccal mucosa," *Periodontics*, vol. 2, pp. 184-291, 1964.
- [140] M. W. Davidson, "Microscope objective specifications," vol. 2001: Nikon, Inc.
- [141] W. F. Cheong, S. A. Prahl, and A. J. Welch, "A review of the optical properties of biological tissues," *IEEE Journal of Selected Topics in Quantum Electronics*, vol. 26, pp. 2166-2185, 1990.
- [142] G. J. Tearney, M. E. Brezinski, B. E. Bouma, S. A. Boppart, C. Pitris, J. F. Southern, and J. G. Fujimoto, "In vivo endoscopic optical biopsy with optical coherence tomography," *Science*, vol. 276, pp. 2037-2039, 1997.
- [143] A. M. Rollins, "Real time endoscopic and functional imaging of biological ultrastructure using optical coherence tomography," in *Department of Biomedical Engineering*. Cleveland: Case Western Reserve University, 2000, pp. 217.
- [144] B. M. Hoeling, A. D. Fernandez, R. C. Haskell, E. Huang, W. R. Myers, D. C. Peterson, S. E. Ungersma, R. Wang, and M. E. Williams, "An optical coherence microscope for 3-dimensional imaging in developmental biology," *Optics Express*, vol. 6, pp. 136-146, 2000.
- [145] B. M. Hoeling, A. D. Fernandez, R. C. Haskell, and D. C. Petersen, "Phase modulation at 125 kHz in a Michelson interferometer using an inexpensive piezoelectric stack driven at resonance," *Review of Scientific Instruments*, vol. 72, pp. 1630-1633, 2001.

- [146] M. Imai, T. Yano, K. Motoi, and A. Odajima, "Piezoelectrically induced optical phase modulation of light in single-mode fibers," *IEEE Journal of Selected Topics in Quantum Electronics*, vol. 28, pp. 1901-1908, 1992.
- [147] R. H. Webb, "Optics for laser rasters," *Applied Optics*, vol. 23, pp. 3680-3683, 1984.
- [148] E. H. K. Stelzer, "The intermediate optical system of laser-scanning confocal microscopes," in *Handbook of Confocal Microscopy*, J. B. Pawley, Ed., 2nd ed. New York: Plenum Press, 1995, pp. 139-154.
- [149] Z. S. Tannous, M. C. Mihm, T. J. Flotte, and S. González, "In vivo examination of lentigo maligna and malignant melanoma *in situ*, lentigo maligna type by near-infrared reflectance confocal microscopy: Comparison of *in vivo* confocal images with histologic sections," *Journal of the American Academy of Dermatology*, vol. 46, pp. 260-3, 2002.
- [150] W. Drexler, U. Morgner, F. X. Kartner, C. Pitris, S. A. Boppart, X. D. Li, E. P. Ippen, and J. G. Fujimoto, "In vivo ultrahigh-resolution optical coherence tomography," *Optics Letters*, vol. 24, pp. 1221-1223, 1999.
- [151] C. Pitris, A. Goodman, S. A. Boppart, J. J. Libus, J. G. Fujimoto, and M. E. Brezinski, "High-resolution imaging of gynecologic neoplasms using optical coherence tomography," *Obstetrics and gynecology*, vol. 93, pp. 135-9, 1999.
- [152] G. Zuccaro, N. Gladkova, J. Vargo, F. Feldchtein, E. Zagaynova, D. Conwell, G. Falk, J. Goldblum, J. Dumot, J. Ponsky, G. Gelikonov, B. Davros, E. Donchenko, and J. Richter, "Optical coherence tomography of the esophagus and proximal stomach in health and disease," *The American journal of gastroenterology*, vol. 96, pp. 2633-9, 2001.

- [153] S. Jäckle, N. Gladkova, F. Feldchtein, A. Terentieva, B. Brand, G. Gelikonov, V. Gelikonov, A. Sergeev, A. Fritscher-Ravens, J. Freund, U. Seitz, S. Schröder, and N. Soehendra, "In vivo endoscopic optical coherence tomography of esophagitis, Barrett's esophagus, and adenocarcinoma of the esophagus," *Endoscopy*, vol. 32, pp. 750-5, 2000.
- [154] S. Jäckle, N. Gladkova, F. Feldchtein, A. Terentieva, B. Brand, G. Gelikonov, V. Gelikonov, A. Sergeev, A. Fritscher-Ravens, J. Freund, U. Seitz, S. Soehendra, and N. Schröders, "In vivo endoscopic optical coherence tomography of the human gastrointestinal tract--toward optical biopsy," *Endoscopy*, vol. 32, pp. 743-9, 2000.
- [155] A. M. Sergeev, V. M. Gelikonov, G. V. Gelikonov, F. I. Feldchtein, R. V. Kuranov, and N. D. Gladkova, "In vivo endoscopic OCT imaging of precancer and cancer states of human mucosa," *Optics Express*, vol. 1, pp. 432-440, 1997.
- [156] B. E. Bouma, G. J. Tearney, C. C. Compton, and N. S. Nishioka, "High-resolution imaging of the human esophagus and stomach in vivo using optical coherence tomography," *Gastrointestinal endoscopy*, vol. 51(4) Pt 1, pp. 467-74, 2000.
- [157] X. D. Li, S. A. Boppart, J. Van Dam, H. Mashimo, M. Mutinga, W. Drexler, M. Klein, C. Pitris, M. L. Krinsky, M. E. Brezinski, and J. G. Fujimoto, "Optical coherence tomography: advanced technology for the endoscopic imaging of Barrett's esophagus," *Endoscopy*, vol. 32, pp. 921-30, 2000.
- [158] C. A. Jesser, S. A. Boppart, C. Pitris, D. L. Stamper, G. P. Nielsen, M. E. Brezinski, and J. G. Fujimoto, "High resolution imaging of transitional cell carcinoma with optical coherence tomography: Feasibility for the evaluation of bladder pathology," *The British journal of radiology*, vol. 72, pp. 1170-6, 1999.

- [159] J. Qu, C. MacAuley, S. Lam, and B. Palcic, "Optical Properties of normal and carcinomatous bronchial tissue," *Applied Optics*, vol. 33, pp. 7397-7405, 1994.
- [160] S. L. Robbins, R. S. Cotran, and V. Kumar, *Pathologic Basis of Disease*, 3rd ed. Philadelphia: W. B. Saunders, 1984.
- [161] Y. Kinoshita, S. Inoue, Y. Honma, and K. Shimura, "Diagnostic significance of nuclear DNA content and nuclear area in oral hyperplasia, dysplasia, and carcinoma," *Journal of oral and maxillofacial surgery*, vol. 50, pp. 728-33, 1992.
- [162] D. Arifler, M. Guillaud, A. Carraro, A. Malpica, M. Follen, and R. R. Richards-Kortum, "Light Scattering from normal and dysplastic cervical cells at different epithelial depths: finite-difference time-domain modeling with a perfectly matched layer boundary condition," *Journal of Biomedical Optics*, Paper under review.
- [163] C. Y. Wang, H. K. Chiang, C. T. Chen, C. P. Chiang, Y. S. Kuo, and S. N. Chow, "Diagnosis of oral cancer by light-induced autofluorescence spectroscopy using double excitation wavelengths," *Oral oncology*, vol. 35, pp. 144-50, 1999.
- [164] A. Gillenwater, R. Jacob, R. Ganeshappa, B. Kemp, A. K. El-Naggar, J. L. Palmer, G. Clayman, M. F. Mitchell, and R. Richards-Kortum, "Noninvasive diagnosis of oral neoplasia based on fluorescence spectroscopy and native tissue autofluorescence," *Archives of otolaryngology--head & neck surgery*, vol. 124, pp. 1251-8, 1998.
- [165] D. C. De Veld, M. Skurichina, M. J. Witjes, R. P. Duin, D. J. Sterenborg, W. M. Star, and J. L. Roodenburg, "Autofluorescence characteristics of healthy oral mucosa at different anatomical sites," *Lasers in surgery and medicine*, vol. 32, pp. 367-76, 2003.

- [166] I. Pavlova, K. Sokolov, R. Drezek, A. Malpica, M. Follen, and R. Richards-Kortum, "Microanatomical and biochemical origins of normal and precancerous cervical autofluorescence using laser-scanning fluorescence confocal microscopy," *Photochemistry and photobiology*, vol. 77, pp. 550-5, 2003.
- [167] R. Drezek, C. Brookner, I. Pavlova, I. Boiko, A. Malpica, R. Lotan, M. Follen, and R. Richards-Kortum, "Autofluorescence microscopy of fresh cervical-tissue sections reveals alterations in tissue biochemistry with dysplasia," *Photochemistry and photobiology*, vol. 73, pp. 636-41, 2001.
- [168] R. Drezek, M. Guillaud, T. Collier, I. Boiko, A. Malpica, C. Macaulay, M. Follen, and R. Richards-Kortum, "Light scattering from cervical cells throughout neoplastic progression: influence of nuclear morphology, DNA content, and chromatin texture," *Journal of biomedical optics*, vol. 8, pp. 7-16, 2003.

Vita

Anne L. Clark was born on England AFB in Alexandria, LA, the daughter of Jacqueline and Richard Clark. She grew up moving all over the United States and the world as her father continued his career in the U. S. Air Force. She graduated from Valdosta High School, Valdosta, GA, in 1988, and the U. S. Air Force Academy in 1992 where she received a commission in the U. S. Air Force and a Bachelor of Science degree in Electrical Engineering and Applied Mathematics.

Her first assignment was to attend the Massachusetts Institute of Technology as a C. S. Draper Fellow where she received a Master of Science degree in Electrical Engineering and Computer Science. Upon graduation, she was assigned to the F-22 Systems Program Office, Wright-Patterson AFB, OH, where she served as the Mission Software Lead Engineer and Integrated Product Team Lead, responsible for development of integrated avionics software for the Air Force's next generation fighter, the F-22 Raptor.

Her next assignment was as an Assistant Professor in the Department of Electrical Engineering at the U. S. Air Force Academy, CO, where she taught introductory electrical engineering concepts and advanced microcomputer design. When selected to return to school, she came to the University of Texas at Austin to pursue a Doctorate of Electrical Engineering under the supervision of Dr. Rebecca Richards-Kortum. After receiving her doctorate, she will go to the Threat Reduction Agency in Alexandria, VA, for three years to improve nuclear hardening techniques for microelectronics before returning to the U. S. Air Force Academy to once again teach electrical engineering.

Permanent address: 3813 Sedgefield Dr., Valdosta, GA 31605

This dissertation was typed by the author, Anne L. Clark